Infocommunications Journal

Technically Co-Sponsored by

IEEE
COMMUNICATIONS
SOCIETY

hte

IEEE
HUNGARY SECTION

Special Issue on Advanced Wireless and Mobile Technologies and Services – Guest Editorial

Hassan Charaf and Sándor Imre

We have been witnessing a rapid development of wireless and mobile technologies and services during the past two decades. 4G mobile services are penetrating, mobile access is becoming an increasingly important way for accessing the Internet, and it is expected to become the dominant one. The progress continues as 5G mobile systems are underway. Although many of the new technologies have already been incorporated in practical systems, there is still enough room for research and experimentation, in particular in the areas of cognitive radio, self-organizing networks, M2M communications, or cross-layer optimization, just to name a few.

The 21st European Wireless (EW) Conference was held in Budapest, Hungary, between 20-22 May 2015, and has been organized by the Budapest University of Technology and Economics (BME). The EW 2015 conference was attended by more than **140 participants** from **30 different countries**. From the conference program, 7 papers were selected for the European Wireless Special Issue, which consists of two parts. The following 5 papers form Part I and are published in this issue, while further 2 papers will appear in the 2015/IV issue as Part II.

The first three papers focus on the physical layer of air interfaces of state-of-the-art wireless systems. *Sebastian Baumgartner* and his colleagues developed a method in OFDM-based DAB/DAB+ systems over dispersive fading channels for the joint estimation of the symbol timing offset, the frequency offset and the channel length from the approximated Log-Likelihood function. In addition, they proposed a CP-based synchronization method, based on a modified timing function that targets the estimation of the parameters from the interference-free region within the cyclic prefix. Simulation results show that the proposed algorithms outperform considerably other algorithms and are robust to varying channel conditions.

Filter bank multicarrier (FBMC) modulation is a promising candidate as the primary physical layer waveform in next generation broadband networks. However, FBMC, like other multicarrier schemes, suffer from high peak-to-average power ratio (PAPR). *Bálint Horváth and Péter Horváth* present how to establish lower bounds on the PAPR in Filter Bank Multicarrier Systems by achieving PAPR reduction for short FBMC frames.

Large MIMO systems are recognized as an effective technique for increasing the spectral and energy efficiency of wireless networks. *Qing Wang et al* considered large MIMO systems in indoor WLANs for multi-user MIMO (MU-MIMO) spatial multiplexing in the 2.4 GHz ISM band. The paper focuses on analyzing the behaviors of large MIMO systems with both centralized and distributed antenna system (CAS and DAS) architectures. The numerical results show that the optimum capacity can be closely approached with both CAS and DAS architectures when the number of Access Point (AP) antennas exceeds the users by a few times.

Above the PHY layer Medium Access Control is responsible for the efficient utilization of the common channel. Unfortunately the end-to-end throughput in single flow multi-hop Ad Hoc networks decays rapidly with path length. Along the path, the success rate of delivering packets towards the destination decreases due to higher contention, interference, limited buffer size and limited shared bandwidth constraints. In order to reduce buffer overflow *Jim Marchang, Bogdan Ghita, and David Lancaster* introduced a dynamic queue utilization based MAC protocol which enhances the performance of an end-to-end data flow by up to 30% for a six hop transmission in a chain topology. They demonstrated that this protocol remains competitive for other network topologies and for a variety of packet sizes.

Finally we present a mobile application related paper from *Péter Sarcevic and his coauthors*. Using wireless sensor networks of two wrist mounted 9-degree-of-freedom (9DOF) sensor boards, movement classification can be reliably done. The sensor boards or motes contain a tri-axial magnetometer, a tri-axial gyroscope, and a tri-axial accelerometer. If the classification is assigned to only one mote, which is using the data from both sensor boards, very energy consuming wireless data transfer is required. In this paper, a hierarchical-distributed algorithm is presented, where the motes are calculating their own movement classes, which can be combined on one mote, to determine the movement of the entire body and arms. The proposed method requires less and smaller classifiers, which can be easily implemented on low performance motes.

We hope this careful selection will satisfy our readers' expectations and please, do not forget to follow Part II of this Special Issue in Issue IV, 2015.

HASSAN CHARAF received his PhD in 1998. He is an Associate Professor and fellow at the Department of Automation and Applied Informatics at the Budapest University of Technology and Economics. He is the head of the IT group. As an outstanding figure in teaching, research and development, he holds key positions at several organizations at the university. His research fields are: distributed systems, cloud computing, multiplatform application development methods, software modeling and data technologies.

SÁNDOR IMRE [M'93] is Professor and Head of Dept. of Networked Systems and Sevices at the Budapest University of Technology (BME). He obtained his Dr. Univ. degree in probability theory and statistics in 1996, Ph.D. degree in 1999, and D.Sc. degree from the Hungarian Academy of Sciences in 2007. He is Chairman of the Telecommunication Scientific Committee of the Hungarian Academy of Sciences. He participates on the Editorial Board of two journals: Infocommunications Journal and Hungarian Telecommunications. He was invited to join the Mobile Innovation Centre as R&D director in 2005. His research interests include mobile and wireless systems, quantum computing and communications. He has contributions especially on different wireless access technologies, mobility protocols, security and privacy, reconfigurable systems, quantum computing based algorithms and protocols.

Robust CP-based Synchronization for DAB/DAB+ Systems over Dispersive Fading Channels

Sebastian Baumgartner, Youssef El Hajj Shehadeh, and Gangolf Hirtz

Abstract—In Orthogonal Frequency Division Multiplexing (OFDM) systems, symbol timing errors and frequency offsets may lead to a significant performance degradation. For this reason, it is very important to achieve a high precision time and frequency synchronization. With the absence of pilot symbols, blind synchronization algorithms using different metric functions or statistics of the received signal can be used. This paper investigates blind synchronization over dispersive fading channels by utilizing the redundant information contained in the cyclic prefix (CP). Whereas some proposed methods require channel information, this paper targets the joint estimation of the symbol timing offset, the frequency offset and the channel length.

Starting by a previously proposed Maximum Likelihood method, we show that the approximated Log-Likelihood (LL) function exhibits a plateau and not a global maximum, leading to significant fluctuations in the estimated parameters. Yet, the symbol timing offset and the channel length characterize the position and dimensions of this plateau. Based on this finding, a novel method is developed for the joint estimation of the symbol timing offset, the frequency offset and the channel length from the approximated LL function. In addition, a second CP-based synchronization method is proposed, based on a modified timing function that targets the estimation of the parameters from the interference-free region within the cyclic prefix.

To demonstrate the performance of the proposed methods and provide a fair comparison with the most recent CP-based synchronization algorithms, Monte Carlo simulations are conducted using the OFDM-based Digital Audio Broadcasting (DAB/DAB+) system under different realistic multipath fading channel conditions. The results show that the proposed algorithms outperform considerably other algorithms in related work and are robust to varying channel conditions.

Keywords—OFDM, synchronization, Maximum Likelihood, timing offset, frequency offset, channel length, multipath channels.

I. INTRODUCTION

Orthogonal Frequency Division Multiplexing (OFDM) is a commonly used technology for broadband data transmission over time and frequency selective fading channels. It is a multicarrier modulation method based on modulating each symbol on an orthogonal subcarrier. Due to its high spectral efficiency and simple detection methods, OFDM has been widely adopted in many wireless standards as LTE, WiMAX, IEEE 802.11, DAB/DAB+ , DVB-T and many others.

However, OFDM systems are sensitive to synchronization errors. The symbol timing offset (STO) describes the unknown symbol arrival time and thereby the FFT (Fast Fourier Transform) window positioning in the receiver. Therefore, accurate

Department of Electrical Engineering and Information Technology, Technische Universität Chemnitz, Germany, E-mail: {baumg, eyo, g.hirtz}@etit.tu-chemnitz.de

time synchronization is essential in an OFDM system. The carrier frequency offset (CFO) is caused by a mismatch between the carrier frequencies of the oscillators at the transmitter and the receiver, as well as Doppler-effects due to the relative motion of the transmitter and the receiver in mobile communications. Time synchronization can be performed using a specific transmitted synchronization signal (preamble), virtual subcarriers or pilot symbols within an OFDM symbol [1]–[5]. However, in OFDM systems which do not offer any predefined pilot data like Digital Audio Broadcasting (DAB/DAB+) [6], the determination of the unknown symbol timing, as well as the carrier frequency offset is an important challenging issue and therefore tackled by this paper. Interestingly, this can be achieved by leveraging the redundancy induced by the Cyclic Prefix (CP) and exploiting the correlation characteristics within an OFDM symbol [7]–[10].

Based on this principle, various blind synchronization algorithms have been proposed. In [9], the Maximum Likelihood (ML) principle has been utilized to estimate both the timing offset and the frequency offset under Additive White Gaussian Noise (AWGN) channels. This method has also been shown to perform well under flat-fading channels. However, the performance degrades in case of a frequency-selective fading channel as the algorithm results in significant fluctuations in the estimated timing offset, and tends to get an additional offset which depends on the time spread of the channel. An attempt to derive the Maximum Likelihood method over dispersive fading channels has been taken in [11], where a Likelihood function is derived based on simplified correlation characteristics. However, the method has been found to be non-robust to channel conditions as we will see in this paper. Two symbol timing synchronization algorithms over multipath fading channels were proposed in [12]. These are based on the Maximum Correlation (MC) metric and the Minimum Mean Square Error (MMSE) metric and utilize a correlation length equal to the sum of the channel length and the CP length. Another approach is proposed in [13], based on a Least Square (LS) principle for joint estimation of the symbol timing as well as the frequency offset. The paper in [7] proposes a new timing function to identify the correct STO without any information of the channel profile and channel length. The closest to this work is the idea proposed in [14]. In that paper, a new timing function is proposed and it is shown that the STO and the channel length can be both estimated from the transition characteristics of the proposed timing function.

In this paper, we first analyze the approximated Log-Likelihood (LL) function proposed in [11] showing that it exhibits a plateau over a wide range of STO and channel

length (L) values. This leads to significant fluctuations in the estimated timing offset. Yet, we show that these two parameters can be indirectly estimated from the position and dimensions of this plateau. Consequently, we propose a novel algorithm that estimates jointly the symbol timing offset and the channel length from the transition characteristics of the derived LL function. Moreover, we also propose a modified timing function which is based on seeking the interference-free region and estimating the different parameters from the samples in this region. The two methods are also extended to estimate the frequency offset.

In order to get a fair comparison between the proposed methods and the most recent CP-based synchronization algorithms, all simulations are applied to the same realistic multipath fading channel conditions and evaluated with respect to the Mean Square Error (MSE). The OFDM-based Digital Audio Broadcasting (DAB/DAB+) system [6] is used according to the channel conditions specified in [15], which are realized via a tapped-delay-line model as proposed in [16]. Through Monte Carlo simulations, the proposed algorithms are shown to outperform other methods proposed in related work and the method based on the modified timing function is shown to be robust to different multipath channels.

The rest of the paper is organized as follows: Section II describes the OFDM baseband signal received with a timing and frequency offset over a multipath fading channel. In Section III, the Log-Likelihood function for the joint estimation of the STO and the channel length is derived. After that, the proposed approaches are described in Section IV. Section V provides the simulation results for different multipath propagation channels. Finally, section VI concludes this paper.

Notation: Lower bold letters are used to denote vectors. The complex conjugation of a complex number is denoted by the superscript $(z)^*$, $|z|$ denotes the absolute value whereas $\text{Re}\{z\}$ denotes the real part of a complex number. $E\{\cdot\}$ stands for the statistical expectation. Finally, all estimated parameters are described via $(\hat{\cdot})$.

II. DESCRIPTION OF THE RECEIVED OFDM BASEBAND SIGNAL

At the transmitter side of an OFDM based system, the serial bitstream is first grouped and mapped onto complex constellation points $d_m(k) \in \mathbb{C}$, before being applied to an Inverse Discrete Fourier Transform (IDFT) of size N_u. The resulting m^{th} complex OFDM baseband symbol is given for every subcarrier position $n \in [0, N_u - 1]$ in the time domain as follows

$$x_m(n) = \frac{1}{\sqrt{N_u}} \sum_{k=0}^{N_u - 1} d_m(k) e^{j \frac{2\pi}{N_u} kn}. \quad (1)$$

In order to prevent Inter Symbol Interference (ISI), every OFDM symbol is preceded by a cyclic prefix (guard interval) of N_g samples. One complete OFDM symbol consists therefore of $N_s = N_u + N_g$ samples. As a result, the final m^{th} transmitted time domain signal defined over $[0, N_s - 1]$ will be

$$s_m(n) = \begin{cases} x_m(n + N_u - N_g) & , n \in [0, \ N_g - 1] \\ x_m(n - N_g) & , n \in [N_g, \ N_s - 1] \\ 0 & , \text{otherwise}. \end{cases} \quad (2)$$

Since the CP is a copy of the last N_g samples, the following correlation properties are obtained in the transmitted symbol:

$$E\{s_m(n_1)s_m^*(n_2)\} = \begin{cases} \sigma_s^2 & , n_2 = n_1 \\ \sigma_s^2 & , n_2 = n_1 + N_u \\ 0 & , \text{otherwise} \end{cases} \quad (3)$$

where σ_s^2 is the signal power.

The obtained symbol in (2) is then transmitted over a multipath fading channel that is assumed to be quasi-stationary over M OFDM symbols. The channel impulse response can be modeled as a tapped-delay line with $(L + 1)$ taps of complex attenuation factors $h(l)$. We note that for a finite channel length L, $h(l) = 0$ for $l > L$. The guard interval length is assumed to be greater than or equal to the channel length (i.e., $N_g \geq L$), such that only a small part within the guard interval of the current m^{th} symbol is corrupted by the preceding $(m - 1)^{th}$ symbol. In this case, the mth received OFDM symbol depends, due to ISI, on both the mth and the $(m - 1)^{th}$ transmitted OFDM symbols.

Consider ε as the normalized frequency offset with respect to the subcarrier spacing and θ as the unknown symbol timing offset. The expression of the mth received OFDM symbol can be written as

$$r_m(n) = e^{j \frac{2\pi n \varepsilon}{N_u}} \left(\sum_{l=0}^{L} h(l) \, s_{m-1}(n + N_s - l - \theta) \right. $$
$$\left. + \sum_{l=0}^{L} h(l) \, s_m(n - l - \theta) \right) + \eta(n), \quad (4)$$

where $\eta \sim \mathcal{N}(0, \sigma_\eta^2)$ is a complex additive white Gaussian noise and $n = \{\theta, \theta + 1, \ldots, \theta + N_u + N_g - 1\}$. The index l within the argument of $s_m(n - l - \theta)$, describes the time delay of every propagation path $l \in \{0, 1, \ldots, L\}$ with respect to the sampling time t_s of the system, i.e. $l = \lfloor \tau_l / t_s \rfloor$.

III. LIKELIHOOD FUNCTION

In this paper, the joint estimation of the symbol timing offset, the frequency offset and the channel length is investigated based on the redundancy information in the CP. Since the cyclic prefix is a copy of the last part of an OFDM symbol, the correlation characteristics between a given sample $r_m(n)$ and the corresponding separated-by-N_u sample $r_m(n + N_u)$ needs to be determined. Hereby, the expression $r_m(n + N_u)$ can be written in function of the mth and the $(m + 1)^{th}$ transmitted OFDM symbols as

$$r_m(n + N_u) = e^{j \frac{2\pi (n + N_u) \varepsilon}{N_u}} \left(\sum_{l=0}^{L} h(l) \, s_m(n + N_u - l - \theta) \right. $$
$$\left. + \sum_{l=0}^{L} h(l) \, s_{m+1}(n - N_g - l - \theta) \right) + \eta(n + N_u), \quad (5)$$

Robust CP-based Synchronization for DAB/DAB+
Systems over Dispersive Fading Channels

where $n = \{\theta, \theta+1, \ldots, \theta+N_u+N_g-1\}$.

Due to the fact that the transmitted symbols $s_{m-1}(n)$, $s_m(n)$ and $s_{m+1}(n)$, the channel taps $h(l)$ and the noise $\eta(n)$ are mutually uncorrelated (assuming uncorrelated scattering), the auto-correlation $E\{\psi_m(n)\} = E\{r_m(n) r_m^*(n+N_u)\}$ between samples separated-by-N_u can be found to be

$$
E\{\psi_m(n)\} = \begin{cases} \sigma_s^2\, e^{-j2\pi\varepsilon} \sum_{l=0}^{n-\theta} |h(l)|^2 & , n \in I_1 \\ \sigma_s^2\, e^{-j2\pi\varepsilon} \sum_{l=0}^{L} |h(l)|^2 & , n \in I_2 \\ \sigma_s^2\, e^{-j2\pi\varepsilon} \sum_{l=n-\theta-N_g+1}^{L} |h(l)|^2 & , n \in I_3 \\ 0 & , \text{otherw.} \end{cases}
$$
(6)

with the intervals

$$
\begin{aligned}
I_1 &\equiv \{\theta, \theta+1, \ldots, \theta+L-1\} \\
I_2 &\equiv \{\theta+L, \theta+L+1, \ldots, \theta+N_g-1\} \\
I_3 &\equiv \{\theta+N_g, \theta+N_g+1, \ldots, \theta+N_g+L-1\}.
\end{aligned}
$$
(7)

On the other hand, it can be verified that $E\{|r_m(n)|^2\} = \sigma_s^2 \sum_l |h(l)|^2 + \sigma_\eta^2 \equiv \sigma_r^2$. For a normalized channel (i.e. $\sum_l |h(l)|^2 = 1$), we get $\sigma_r^2 = \sigma_s^2 + \sigma_\eta^2$.

According to the central limit theorem, the received sample $r_m(n)$ can be approximated for large values of N_u as a complex Gaussian random variable of variance σ_r^2; the probability density function (pdf) is given by [11]

$$
f(r_m(n)) = \frac{\exp\left(-\frac{|r_m(n)|^2}{\sigma_r^2}\right)}{\pi\, \sigma_r^2}.
$$
(8)

Consequently, the samples $r_m(n)$ and $r_m(n+N_u)$ follow a bivariate complex Gaussian distribution with a joint pdf [11]:

$$
f(r_m(n), r_m(n+N_u)) =
$$
$$
\frac{\exp\left(-\frac{|r_m(n)|^2+|r_m(n+N_u)|^2-2\rho_n\,\mathrm{Re}\left\{e^{j2\pi\varepsilon} r_m(n) r_m^*(n+N_u)\right\}}{\sigma_r^2(1-\rho_n^2)}\right)}{\pi^2\,(\sigma_r^2)^2\,(1-\rho_n^2)},
$$
(9)

where

$$
\rho_n = \left| \frac{E\{r_m(n) r_m^*(n+N_u)\}}{\sqrt{E\{|r_m(n)|^2\}\, E\{|r_m(n+N_u)|^2\}}} \right|.
$$
(10)

is the correlation coefficient with respect to the complex samples $r_m(n)$ and $r_m(n+N_u)$.

To derive the correlation characteristics, an observation window of length $(2N_u+N_g)$ samples needs to be considered at the receiver and therefore the likelihood function of the received vector $\mathbf{r}_m = [r_m(1), r_m(2), \ldots, r_m(2N_u+N_g)]$ is required. Yet, the multipath effects introduce correlation between the received samples which complicates the derivation of a likelihood function and a closed form expression remains an open problem. In [11], the following approximation has been considered to derive a likelihood function:

$$
E\{r_m(n) r_m^*(n+k)\} = 0, \quad k \neq \{0, N_u\}.
$$
(11)

Consequently, the likelihood function can be expressed as

$$
\begin{aligned}
\Lambda_m(\theta, L) &= f(\mathbf{r}_m | \theta, L) \\
&= \prod_{n \in I} \frac{f(r_m(n), r_m(n+N_u))}{f(r_m(n)) f(r_m(n+N_u))} \prod_n f(r_m(n)).
\end{aligned}
$$
(12)

where $I = I_1 \cup I_2 \cup I_3$.

The product $\prod_n f(r_m(n))$ is thereby independent of θ and L and can be omitted. Subsequently, the likelihood function becomes

$$
\Lambda_m(\theta, L) = \prod_{n \in I} \frac{f(r_m(n), r_m(n+N_u))}{f(r_m(n)) f(r_m(n+N_u))}.
$$
(13)

Due to the fact that the logarithmic function is a strictly increasing function, it does not influence the following maxima search to determine the unknown parameters θ and L. Thus, the so-called Log-Likelihood (LL) function for M received OFDM symbols is finally given by

$$
\Lambda(\theta, L) = \log\left(\prod_{m=1}^{M} \Lambda_m(\theta, L)\right) = \sum_{m=1}^{M} \log(\Lambda_m(\theta, L)).
$$
(14)

Inserting (13) and the pdf specifications given by (8) and (9) into (14), one can easily get [11]

$$
\Lambda(\theta, L) = \sum_{n \in I} \left\{ \frac{2\left(\rho_n \Psi(n) - \rho_n^2 \Phi(n)\right)}{\sigma_r^2\,(1-\rho_n^2)} - M\log\left(1-\rho_n^2\right) \right\},
$$
(15)

where the variables $\Psi(n)$ and $\Phi(n)$ are defined as

$$
\begin{aligned}
\Psi(n) &= \sum_{m=1}^{M} \mathrm{Re}\{e^{j2\pi\varepsilon} r_m(n) r_m^*(n+N_u)\} \\
&= \sum_{m=1}^{M} \mathrm{Re}\{e^{j2\pi\varepsilon} \psi_m(n)\}, \\
\Phi(n) &= \sum_{m=1}^{M} \frac{1}{2}\left(|r_m(n)|^2 + |r_m(n+N_u)|^2\right).
\end{aligned}
$$
(16)

Alternatively, (15) can now be written as a summation $\Lambda(\theta, L) = \sum_{n \in I} \Lambda_n(\theta, L)$ where

$$
\Lambda_n(\theta, L) = \frac{2\left(\rho_n \Psi(n) - \rho_n^2 \Phi(n)\right)}{\sigma_r^2\,(1-\rho_n^2)} - M\log\left(1-\rho_n^2\right).
$$
(17)

Before obtaining the ML estimates of θ and L, it is necessary to estimate the correlation coefficients ρ_n. These can also be estimated in a Maximum Likelihood way. By the partial derivation of the LL function with respect to ρ_n, these coefficients can be found to be the real roots of the following equation of third degree:

$$\sigma_r^2\,\rho_n^3 - \Psi(n)\,\rho_n^2 + (2\,\Phi(n) - \sigma_r^2)\,\rho_n - \Psi(n) = 0 \quad (18)$$

The ML estimates $(\hat{\theta}, \hat{L})$ can then be obtained by searching for the maximum of the LL function:

$$(\hat{\theta}, \hat{L}) = \arg\max_{(\theta, L)} \Lambda(\theta, L) \quad (19)$$

Finally, the frequency offset $\hat{\varepsilon}$ can be estimated from the argument of $\psi(n) = \sum_{m=1}^{M} \psi_m(n)$ averaged over the interval I as follows:

$$\hat{\varepsilon} = -\frac{1}{2\pi} \angle \sum_{n \in I} \psi(n). \quad (20)$$

IV. PROPOSED METHODS

A. Log-Likelihood Transition Characteristics

The approximation in (11) is only valid over AWGN or flat fading channels ($L = 0$). In this case, the LL function has a global maximum at the corresponding STO (see Fig. 1). Over a frequency-selective fading channel, the successive received samples are correlated due to the multipath effects which results in a nonzero channel-dependent correlation in (11). Therefore, the derived likelihood function is not exact and it has been found to have a plateau instead of a peak at the corresponding time offset (see Fig. 2) which results in significant fluctuations in the estimates of θ and L.

Interestingly, the position and the dimensions of the plateau depend directly on θ and L [17]. In Fig. 1 and Fig. 2, the LL function is plotted as a function of θ and L in the case $L = 0$ (flat fading channel) and $L = 9$, respectively. Graphs (a) and (b) correspond to $STO = 10$ and $STO = 20$. Comparing (a) and (b) in both figures[1], it can be observed that the position of the plateau depends directly on the symbol timing offset. On the other hand, the dimension of the plateau is influenced by the delay spread of the channel. This can be clearly seen by comparing Fig. 1 and Fig. 2. Over a flat fading channel (Fig. 1), the plateau is reduced in the plane ($L = 0$) to a single point corresponding to the STO, whereas the size of the plateau increases as the channel length increases. Moreover, we notice that the decreasing edge of the plateau corresponds to the sum: $(\theta + L)$. Thus, tracking this edge allows to get an estimate of the sum of the investigated parameters.

Based on this observation, we propose a novel algorithm for the joint estimation of the STO and the channel length using the derived LL function over dispersive multipath channels. In our algorithm (depicted in Algorithm 1), $(\hat{\tau} = \hat{\theta} + \hat{L})$ is estimated by tracking the decreasing edge of the plateau. First, an interval of $\hat{\tau}$ is defined by finding the maximum of the LL function at $L = 0$. After that, $\hat{\tau}$ is estimated by calculating the variations of the LL function around this maximum and detecting the first significant negative variation (in our implementation, the first variation that is lower than

[1]Note that the two curves (a) and (b) do not correspond to the exact same channel. They were generated over two different simulation runs. This explains the slight difference in the behavior of the LL function.
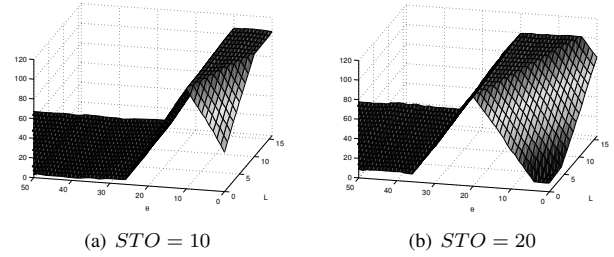
Fig. 1. 3D plot of the LL function for $STO = 10$ (a), $STO = 20$ (b) in the case of a flat fading channel ($L = 0$).
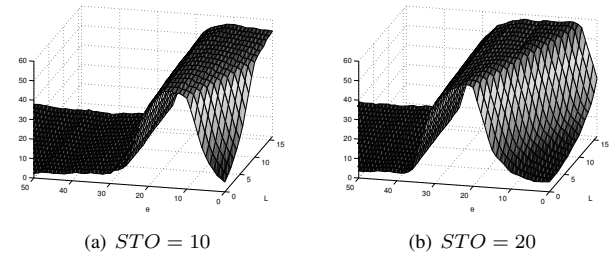
Fig. 2. 3D plot of the LL function for $STO = 10$ (a), $STO = 20$ (b) in the case of a multipath fading channel of length $L = 9$.

-2% is sought). The fact that the LL function behaves similarly in this area for all values of L enables to get a robust estimate $\hat{\tau}$.

Now that $(\theta + L)$ has been estimated, it only remains to estimate one of these two parameters to obtain the other one. From Fig. 1 and Fig. 2, it can be observed that the LL function in the plane ($L = 0$) reaches its plateau at the required STO. Therefore, the estimate $\hat{\theta}$ is obtained by capturing the increasing edge of the LL function. This can simply be obtained by detecting the last significant positive

---

Algorithm 1 Search Algorithm for θ and L

Step 1: Find $\theta_{max} = \arg\max_{\theta} \Lambda(\theta, L = 0)$
Step 2: Find $\hat{\tau}$:
  $\Lambda_L(\theta) = E_L\{\Lambda(\theta, L)\}$
  for $\theta = \theta_{max}$ to $\theta_{max} + N_g - 1$ **do**
    if $\Delta\Lambda_L(\theta)/\Lambda_L(\theta) \leq -0.02$ **then**
      $\hat{\tau} = \theta$;
      $break$;
    end if
  end for
Step 3: Find $\hat{\theta}$:
  for $\theta = \hat{\tau}$ to $\hat{\tau} - N_g$ **do** {decreasing order}
    if $\Delta\Lambda(\theta, 0)/\Lambda(\theta, 0) \geq 0.02$ **then**
      $\hat{\theta} = \theta$;
      $break$;
    end if
  end for
Step 4: Find $\hat{L} = \hat{\tau} - \hat{\theta}$

---

variation reaching the plateau. Moreover, since $0 \leq L \leq N_g$, we first define an interval of the STO $[(\hat{\tau} - N_g), \ \hat{\tau}]$. This has been found to increase the robustness of the estimated $\hat{\theta}$ value. Finally, after obtaining $\hat{\theta}$, the estimate of the channel length can be obtained as: $\hat{L} = \hat{\tau} - \hat{\theta}$.

B. Modified Timing Function

In addition to the method based on the transition characteristics of the Log-Likelihood function, we also propose a new modified timing function that allows a high performance estimation of the timing offset and the channel length. Whereas the LL function involves a summation over the interval I, the modified timing function limits this summation to the interval I_2:

$$\tilde{\Lambda}(\theta, L) = \sum_{n \in I_2} \left\{ \frac{2\left(\rho_n \Psi(n) - \rho_n^2 \Phi(n)\right)}{\sigma_r^2 \left(1 - \rho_n^2\right)} - M \log\left(1 - \rho_n^2\right) \right\}, \quad (21)$$

Indeed, from (6) it can be seen that the intervals I_1 and I_3 involve channel effects whereas the interference-free region I_2 is independent of the channel profile. By limiting the summation to this interval, the timing function exhibits then a peak allowing an easy and accurate estimation of both the timing offset and the channel length as follows:

$$(\hat{\theta}, \hat{L}) = \arg\max_{(\theta, L)} \tilde{\Lambda}(\theta, L) \quad (22)$$

Note that (21) is a function of two variables where the interval I_2 in the summation depends on the unknown parameter L. Consequently, (21) needs to be evaluated for different values of L. The two dimensional function exhibits then a peak at the corresponding values of θ and L.

The frequency offset can also be estimated similar to (20) but by limiting the summation to the interference-free region I_2:

$$\hat{\varepsilon} = -\frac{1}{2\pi} \angle \sum_{n \in I_2} \psi(n). \quad (23)$$

V. SIMULATION RESULTS AND DISCUSSIONS

In order to demonstrate the performance of the proposed methods and compare them with the most recent blind synchronization algorithms, all procedures are applied to the OFDM based Digital Audio Broadcasting (DAB/DAB+) system in transmission mode III according to the specifications in [6]. In this mode every OFDM symbol consists of 192 active subcarriers which are modulated via a $\pi/4$-DQPSK, a FFT size of $N_u = 256$ and a guard interval of $N_g = 63$ samples, respectively. The channel is specified according to the norm given in [15], which is based on the COST-207 channel specification [18]. The Typical Urban (TU) and Bad Urban (BU) channel models are adopted for the simulations. The corresponding channel-tap powers and delays as well as

TABLE I
CHANNEL PARAMETERS FOR THE SIMULATION

(a) Typical Urban channel according to [15], [18]

Parameters	Values
Tap delays [μs]	$[0, 0.2, 0.6, 1.6, 2.4, 5.0]$
Tap powers [dB]	$[-3, 0, -2, -6, -8, -10]$
Doppler profile	[Jakes,Jakes,Gauß1,Gauß1,Gauß2,Gauß2]

(b) Bad Urban channel according to [15], [18]

Parameters	Values
Tap delays [μs]	$[0, 0.4, 1.0, 1.6, 5.0, 6.6]$
Tap powers [dB]	$[-3, 0, -3, -5, -2, -4]$
Doppler profile	[Jakes,Jakes,Gauß1,Gauß1,Gauß2,Gauß2]

Doppler profiles are summarized in Table I. The multipath channels are thereby realized via a tapped-delay-line model according to [16] and are fixed in each OFDM symbol but independent from one run to another within 10^3 Monte Carlo trials. Without loss of generality, in every simulation run the symbol timing is fixed to $\theta = 5$ samples and the frequency offset ε is $1/3$ of the subcarrier spacing, i.e. 2.667 kHz. Unless otherwise stated, $M = 5$ OFDM symbols are considered. The results are evaluated in terms of the probability of lock-in[2] ($P(\hat{\theta} = \theta)$) +, the Normalized (with respect to N_u^2) Mean Square Error (NMSE) between the estimated and real STO, and the NMSE of the frequency offset for different signal-to-noise ratios (SNR).

In the following, the modified ML method in AWGN and flat-fading channels [9], [19] is specified by (MLA) under the assumption of an ideal knowledge of the correlation coefficient according to (10). The Maximum Correlation procedure of [12] is denoted by (MC), and the Minimum Mean Square Error algorithm is denoted by (MMSE). The algorithm based on a new timing function proposed in [14] is denoted by (NTF). The ML algorithm over dispersive channels [11] according to (19) is denoted as (MLD). Recall that this algorithm exhibits significant fluctuations in the estimated STO, resulting in a high error floor. Finally, the proposed method based on the transition characteristics of the LL function is denoted by (LLTC) and the method based on the modified timing function (21) is denoted as (ML-I2).

Fig. 3 shows the simulation results ((a) Probability of Lock-in, (b) NMSE of STO, and (c) NMSE of CFO) in case of a Typical Urban channel whereas Fig. 4 shows the results for a Bad Urban channel model [15], [18]. Observing Fig. 3(a) and Fig. 4(a), it can be clearly noted that the proposed algorithms outperform significantly the other algorithms in terms of the probability of lock-in. In contrary to other algorithms which exhibit an error floor, the performance of the proposed algorithms increase with the SNR. This can also be seen in the NMSE curves of the STO in Fig. 3(b) and Fig 4(b). Moreover, it is interesting to note that the (ML-I2) method is more robust to channel conditions than (LLTC) as it shows high performance over both channel models whereas the performance of (LLTC)

---

[2]Note that this definition is different to some works where the probability of lock-in is evaluated with respect to the interference free region, where the correction of the remaining rotation is left to the equalizer.
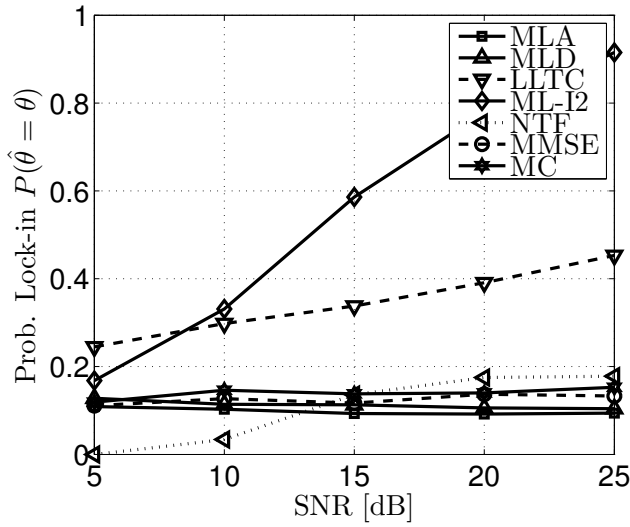
(a) Probability of Lock-in as a function of SNR
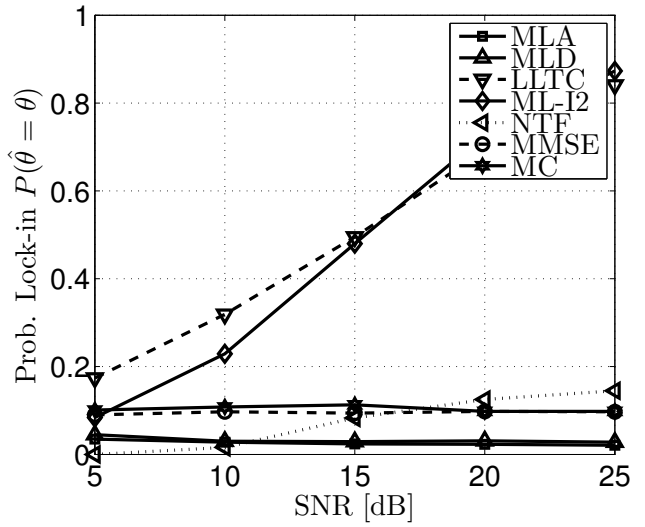
(a) Probability of Lock-in as a function of SNR
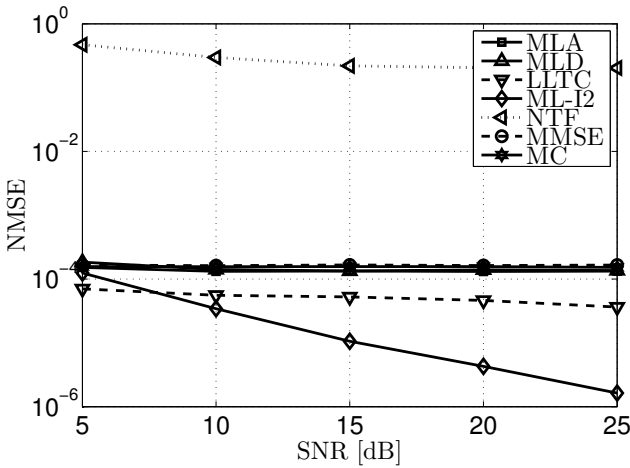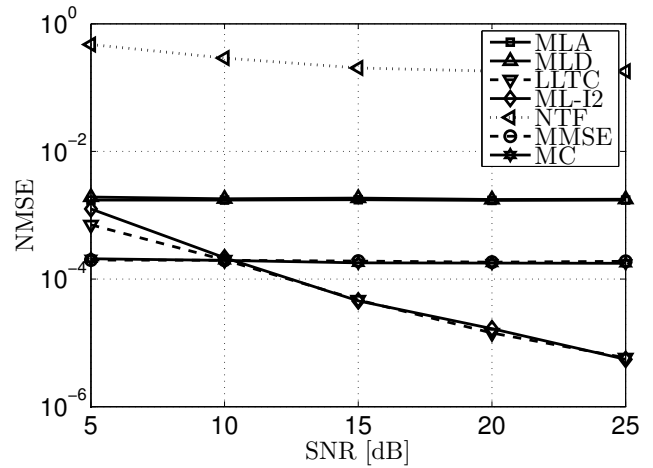
(b) NMSE of the STO as a function of SNR

(b) NMSE of the STO as a function of SNR
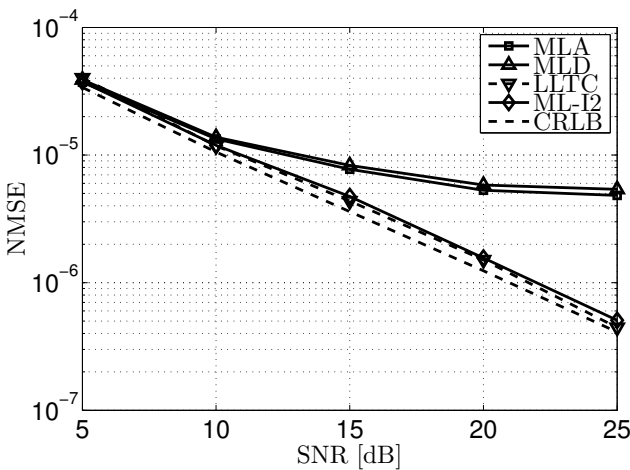
(c) NMSE of the CFO as a function of SNR
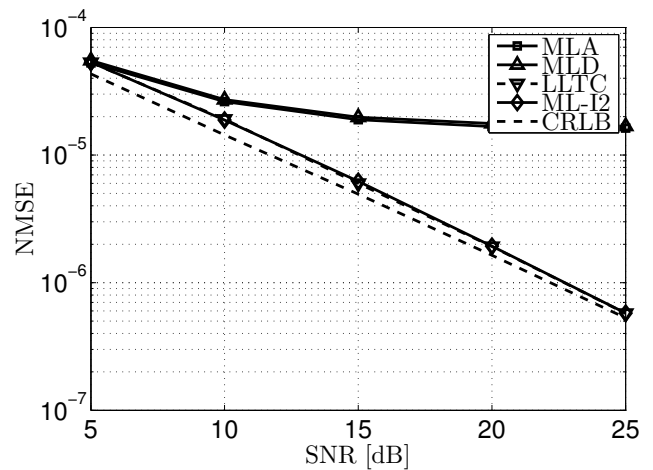
(c) NMSE of the CFO as a function of SNR

Fig. 3. Simulation results in case of a Typical Urban channel [15], [18]

Fig. 4. Simulation results in case of a Bad Urban channel [15], [18]

Robust CP-based Synchronization for DAB/DAB+
Systems over Dispersive Fading Channels
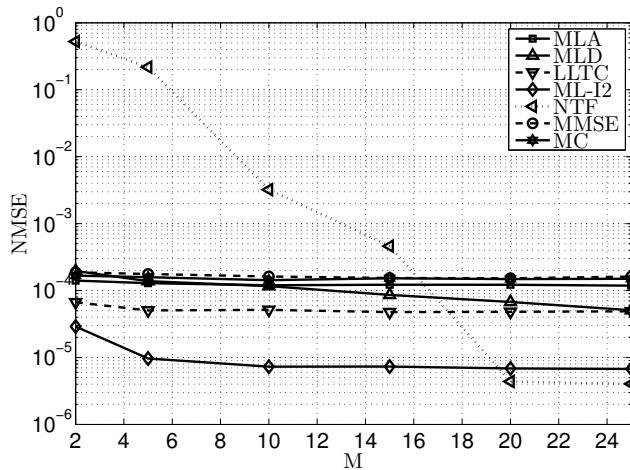
(a) NMSE of the STO as a function of M
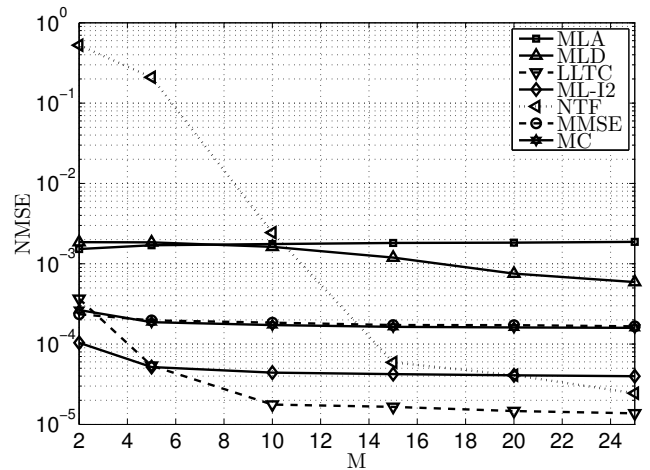
(a) NMSE of the STO as a function of M
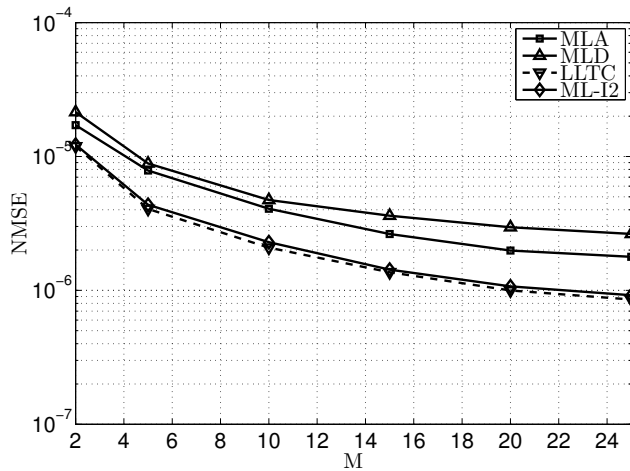
(b) NMSE of the CFO as a function M
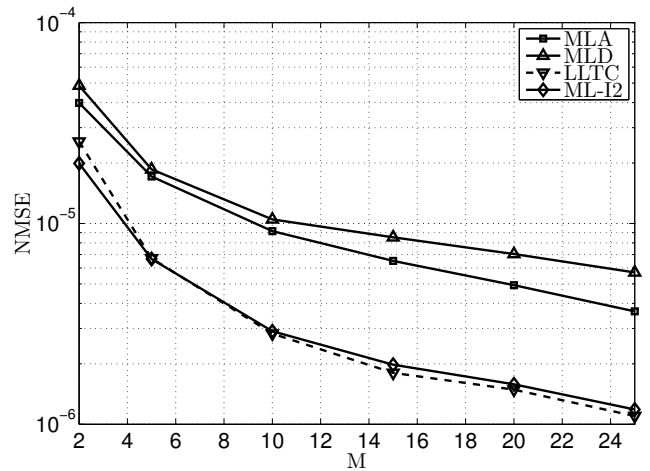
(b) NMSE of the CFO as a function M

Fig. 5. Simulation results in case of a Typical Urban channel [15], [18] for SNR= 15 dB

Fig. 6. Simulation results in case of a Bad Urban channel [15], [18] for SNR= 15 dB

is much less over the Typical Urban channel.

The simulation results for the frequency offset are shown in Fig. 3(c) and Fig. 4(c), for the Typical Urban and Bad Urban channels, respectively. The results of the MLD and MLA methods are similar to each other and do not show much improvement with a higher SNR. On the other hand, the proposed methods show very high performance as the MSE of the frequency offset is close to the Cramér-Rao lower bound (CRLB), which is derived in [11].

Finally, Fig. 5 and Fig. 6 show the results of the STO mean squared error and the CFO mean squared error as a function of the number of OFDM symbols M for an SNR of 15 dB over the Typical Urban and the Bad Urban channels, respectively. In terms of STO estimation (Fig. 5(a) and Fig. 6(a)), the proposed algorithms outperform all other algorithms for most values of M and over both channels. The (LLTC) method shows again that its performance depends on the channel profile. While its performance is worse than (ML-I2) over the Typical Urban channel model, it shows a better performance over the Bad Urban channel. It is interesting to see that the

(NTF) method works well for high values of M (M>20) and outperforms slightly (ML-I2) over the Typical Urban channel. However, a high value of M results in higher computational complexity and requires bigger buffer sizes. Due to the good performance for a small parameter M, the proposed methods can be used in the acquisition as well as the tracking phase. As for CFO estimation (Fig. 5(b) and Fig. 6(b)), the proposed algorithms show a similar performance and outperform the (MLA) and (MLD) methods significantly, especially over the Bad Urban channel.

VI. CONCLUSION

In this paper, blind synchronization based on the cyclic prefix in OFDM systems has been investigated. A previously proposed Maximum Likelihood method for the joint estimation of the symbol timing offset and the channel length over dispersive channels has been revisited. It has been shown that the method yields significant fluctuations in the estimation of the symbol timing offset. This is due to a simplification considered in the derivation of the Log-Likelihood method

which was found to exhibit a plateau instead of a global maximum.

Observing that the dimensions and the position of this plateau depend directly on the values of the STO and the channel length, we have proposed a novel CP-based synchronization method. The method estimates the symbol timing offset and the channel length from the size and position of the plateau of the obtained LL function. Moreover, observing that the interference-free region within the cyclic prefix is characterized by channel-profile independent correlation characteristics, a modified timing function is also proposed. This function has been found to exhibit a global maximum allowing a simple estimation of the STO and channel length. In addition, both methods were extended with frequency offset estimation by seeking the argument of the correlation function during the interference-free region.

Simulation results based on the DAB/DAB+ system specifications over realistic channel models have verified the high performance of the proposed methods. In contrast to other CP-based synchronization algorithms, the proposed method based on the modified timing function has been found to be robust to channel conditions showing a high accuracy in the estimation of the timing and frequency offsets over different channel models.

REFERENCES

[1] L. Nasraoui, L. N. Atallah, and M. Siala, "Performance evaluation of an efficient reduced-complexity time synchronization approach for OFDM systems," *annals of telecommunications-annales des télécommunications*, vol. 69, no. 5-6, pp. 321–330, 2014.

[2] B. Shoba, T. Thamizhilakiya, and K. Jayanthi, "A Robust Training-Symbol Based Timing Synchronization for OFDM Systems," *Digital Signal Processing*, vol. 5, no. 7, pp. 243–251, 2013.

[3] H.-T. Hsieh and W.-R. Wu, "Maximum Likelihood Timing and Carrier Frequency Offset Estimation for OFDM Systems With Periodic Preambles," *IEEE Transactions on Vehicular Technology*, vol. 58, no. 8, pp. 4224–4237, Oct 2009.

[4] J. Zhang and M. Wang, "The Improvement of OFDM Symbol Timing Synchronization Based on Continuous Pilot," *Journal of Computational Information Systems*, vol. 9, no. 24, pp. 10 095–10 102, 2013.

[5] X. Ma, C. Tepedelenlioglu, G. B. Giannakis, and S. Barbarossa, "Non-Data-Aided Carrier Offset Estimators for OFDM With Null Subcarriers: Identifiability, Algorithms, and Performance," *IEEE Journal on selected areas in communications*, vol. 19, pp. 2504–2515, 2001.

[6] European Telecommunications Standards Institute (ETSI), "ETSI EN 300 401 V1.4.1: Radio Broadcasting Systems; Digital Audio Broadcasting (DAB) to mobile, portable and fixed receivers," January 2006.

[7] S. Ma, X. Pan, G. Yang, and T. Ng, "Blind Symbol Synchronization Based on Cyclic Prefix for OFDM Systems," *IEEE Transaction on Vehicular Technology*, vol. 58, pp. 1746–1751, 2009.

[8] B. Ai, Z.-X. Yang, C.-Y. Pan, J. hua Ge, Y. Wang, and Z. Lu, "On the synchronization techniques for wireless OFDM systems," *IEEE Transactions on Broadcasting*, vol. 52, no. 2, pp. 236–244, June 2006.

[9] J. van de Beek, M. Sandell, and P. O. Borjesson, "ML Estimation of Time and Frequency Offset in OFDM Systems," *IEEE Transaction on Signal Processing*, vol. 45, pp. 1800–1805, 1997.

[10] M. J. Canet, V. Almenar, S. J. Flores, and J. Valls, "Low Complexity Time Synchronization Algorithm for OFDM Systems with Repetitive Preambles," *Journal of Signal Processing Systems*, vol. 68, no. 3, 2012.

[11] W. L. Chin, "ML Estimation of Timing and Frequency Offsets Using Distinctive Correlation Characteristics of OFDM Signals Over Dispersive Fading Channels," *IEEE Transaction on Vehicular Technology*, vol. 11, pp. 444–456, 2011.

[12] D. Lee and K. Cheun, "Coarse Symbol Synchronization Algorithms for OFDM Systems in Multipath Channels," *IEEE Communication Letters*, vol. 6, pp. 446–448, 2002.

[13] T. Fusco and M. Tanda, "Blind Synchronization for OFDM Systems in Multipath Channels," *IEEE Transaction on Wireless Communications*, vol. 8, pp. 1340–1348, 2009.

[14] X. Liu, K. Pan, Y. Zuo, and J. Chen, "Blind Symbol Synchronization for OFDM Systems in Multipath Fading Channels," *International Conference on Wireless Communications, Networking and Mobile Computing (WICOM)*, vol. 58, pp. 1746–1751, 2010.

[15] DIN Deutsches Institut für Normung e.V., "Characteristics of DAB Receivers; German Version EN 50248:2001," April 2002.

[16] S. Baumgartner, G. Hirtz, and A. Apitzsch, "Methods for Simulation of the Wireless Propagation Channel for DAB/DAB+/DMB-SDR-Receivers," *IEEE Eurocon 2013*, pp. 138–145, 2013.

[17] Y. E. H. Shehadeh, S. Baumgartner, and G. Hirtz, "A Robust Blind Time Synchronization Method in OFDM Systems over Multipath Fading Channels," in *European Wireless*, May 2015.

[18] M. Failli (Chairman), COST 207 Management Committee of the European Commission, *COST 207: Digital land mobile radio communications*. European Commission, December 1989.

[19] S. Baumgartner, Y. E. H. Shehadeh, and G. Hirtz, "Performance Evaluation of Frequency and Symbol Timing Offset Estimation Methods for DAB/DAB+ Receivers under Multipath Fading Channels," in *The 22nd International Conference on Software, Telecommunications and Computer Networks - SoftCOM*, September 2014.

Sebastian Baumgartner was born in Tirschenreuth, Germany in 1982. He received his Dipl. Math. degree in applied mathematics from the University of applied science in Regensburg, Germany in 2006, In 2011, he received his Dipl.-Ing. degree in electrical engineering from the University of Technology in Chemnitz, Germany, where he is currently working toward the Ph.D. degree in the field of blind synchronization of OFDM based systems. His research interests include stochastical signal processing and blind parameter estimation in multi-carrier communication systems.

Youssef El Hajj Shehadeh is currently a postdoctoral researcher at the Chair of Digital Signal Processing and Circuit Design, Chemnitz University of Technology, Germany. He received the PhD degree in 2013 from the institute of Applied Computer Science/Telematics group at the University of Goettingen, Germany. He holds an engineering diploma degree (2009) in Telecommunications from the Lebanese University of Beirut, Lebanon and a master of research degree (2009) in "Digital Telecommunication Systems" from Telecom Paristech (ENST Paris). His research interests vary between digital communications, resource allocation and medium access techniques, and security in wireless networks mainly on the physical layer level.

Gangolf Hirtz has many years of industrial experience in the areas of consumer and automotive electronics. Since 2008, Prof. Dr.-Ing. Gangolf Hirtz heads the chair of Digital Signal Processing and Circuit Design at Chemnitz University of Technology. His current research interests include Camerabased behavior detection of elderly and wireless communications.

Establishing Lower Bounds on the Peak-to-Average-Power Ratio in Filter Bank Multicarrier Systems

Bálint Horváth[1] and Péter Horváth[1]

Abstract—**Filter bank multicarrier (FBMC) modulation is a promising candidate as the primary physical layer waveform in next generation broadband networks. However, FBMC, like other multicarrier schemes, suffer from high peak-to-average power ratio (PAPR). Due to inherent overlapping of the time domain FBMC symbols, the methods designed for PAPR reduction in orthogonal frequency division multiplexing (OFDM) can not be applied in a straightforward manner for FBMC. In this paper, an optimization method is proposed to obtain significant PAPR reduction for short FBMC frames. The formulation of the optimization problem enables the use of both tone reservation and active constellation extension, which are well-known methods for OFDM PAPR reduction. The results establish a practical lower bound on achievable PAPR with these two approaches.**

Keywords—*filter bank multicarrier, peak-to-average power ratio, optimization, constellation extension, tone reservation*

I. INTRODUCTION

Multicarrier modulation schemes gained considerable attention during the past decades in broadband mobile and fixed wireless systems. Numerous standards adopt orthogonal frequency division multiplexing (OFDM) as their physical layer modulation scheme. Among others, various IEEE 802.11 standards, 3GPP LTE, or in the broadcast world, DVB-T2. Evolving present systems in terms of spectral efficiency and advanced spectrum access techniques motivates the search for advanced multicarrier modulation techniques [1]. A family of a promising prospective waveforms is filterbank multicarrier (FBMC), from which we consider the specific scheme known as OFDM/OQAM.

FBMC shares many advantages with traditional OFDM, e.g., high spectrum efficiency, with simple access to both time and frequency domains in terms of scheduling etc. Specifically it offers very low adjacent channel leakage levels. However, FBMC signalling, like other multicarrier schemes, suffer from dynamic fluctuations in the instantaneous power, which is often described in terms of the peak-to-average-power ratio (PAPR). To mitigate this problem, PAPR reduction methods are being employed. Some of these techniques are directly inspired by OFDM based approaches. Such schemes include selective mapping [2] and clipping based [3] [4] methods. However, as adjacent FBMC symbols overlap in time by design, direct

adoption of PAPR reduction schemes originally conceived for OFDM generally yields suboptimal results. Recent algorithms specifically developed for FBMC are taking the overlapping nature into account, e.g., they employ multi block joint optimization [5], or alternative signal method [6].

In this paper we investigate two PAPR reduction schemes and their joint use for FBMC, namely tone reservation (TR) and active constellation extension (ACE). The basic concept of these methods as well as the formulation of the optimal solution through a quadratic constrained quadratic program (QCQP) are introduced for OFDM systems in [7] and in [8], respectively. A suboptimal program is solved for the joint use of the schemes in [9], whereas the program leading to optimal solution for ACE is shown in [10]. A clipping based implementation of TR and ACE was shown in [4], and ACE smart grid projection of Krongold has been also extended to FBMC in [11]. A sliding window based TR technique for FBMC is also shown in [12].

Although straightforward application of TR and ACE for FBMC apparently show some reduction in PAPR, they remain heuristic approaches and lack the basis of objective comparison. The gains in PAPR reduction with these techniques are significantly lower when compared to what can be achieved for OFDM with the same parameters i.e. same number of subcarriers, modulation alphabet, clipping ratio etc. Since FBMC symbols overlap in time, the problem cannot be solved on a per symbol basis (like in OFDM systems). Thus, an entire frame has to be treated.

Motivated by this apparent performance gap, in this paper we formulate the PAPR minimization problem for FBMC, taking into account the inherent intersymbol interference in the scheme. We apply either TR or ACE or both to achieve the smallest possible PAPR for an entire frame. We show that the problem can be cast as a QCQP and the optimum solution can be found numerically. This result provides the minimum achievable PAPR using TR and/or ACE, thus serving as a lower bound to the PAPR, to which practical, real-time implementation of TR and ACE can be compared to.

In real-world systems (e.g., in 3GPP LTE), the frames consist of a relatively small number of symbols to enable a fine-grained resource allocation. Therefore we can choose realistic frame sizes consisting of 8 and 12 symbols per frame and solve the optimization problem for these values.

Besides serving as a baseline for the amount of achievable PAPR reduction, a further potential use of the presented method is to construct optimized packet headers offline with

minimal PAPR in order to transmit the headers with increased average power (e.g., for timing and frequency offset correction or channel estimation).

The paper is organized as follows. In section II the OFDM and FBMC signal synthesis and the PAPR metric is defined. In section III a the principles of PAPR reduction with TR and ACE schemes are summarized. In section IV the PAPR problem formulation for OFDM and the proposed formulation for FBMC signals are detailed. In section V the results of problem solution is shown and the practical lower bound of the PAPR reduction schemes are presented.

II. SIGNAL MODEL AND PERFORMANCE METRICS

A. Orthogonal frequency division multiplexing signal

The synthesis of the time domain signal is based on inverse discrete Fourier transform (IDFT) of data symbols chosen from a M-QAM modulation alphabet. Generation of a transmitted OFDM symbol is made the following way:

$$x[k] = \sum_{n=0}^{N-1} s_n e^{j\frac{2\pi}{NV}nk}, \qquad (1)$$

where $j = \sqrt{-1}$, N is the number of subcarriers and s_n is the complex data symbol on the nth subcarrier and k is the discrete time and V is the oversamping rate.

B. Filter bank multicarrier signal

A thorough introduction and comparison with OFDM can be found in [13]. Based on [13], a frame of the transmitted FBMC signal can be written as:

$$x[k] = \sum_{m=0}^{M-1}\sum_{n=0}^{N-1} (\theta^n s_{re,n}[m]p_0\left[k - mNV\right] +$$

$$\theta^{n+1} s_{im,n}[m]p_0\left[k - mNV - \frac{NV}{2}\right]) e^{j\frac{2\pi}{NV}n(k-mNV)}, \quad (2)$$

where $\theta^k = e^{j\frac{\pi}{2}n}$ and $s_{re}[m]$ and $s_{im}[m]$ denote the real and imaginary parts of the PSK or QAM modulating symbols on the nth subcarrier in the mth signalling time interval, respectively. The prototype filters $p_0[m]$ are designed with an impulse response length $L = KNV$, where K is the overlapping factor, determining the span of the deliberate intersymbol interference in FBMC symbols. An FBMC frame is assumed to consist of M symbols (thus, the length of a frame is $T = L + (M - 1)NV + \frac{NV}{2}$). Throughout this paper the choice of the prototype filter is identical to the one used in [14], known as the PHYDYAS filter, with $K = 4$. The synthesis of the signal written in (2) can be implemented efficiently using the inverse fast Fourier-transform (IFFT) and polyphase decomposition of the modulated prototype filters, as presented in [15]. A more intuitive representation of the synthesis is depicted in Fig. 1. The main blocks of the signal construction is the IFFT and subsequent filtering which is done separately for the real and imaginary parts of the frequency domain symbols whereas the transformed version of the imaginary part is added with a staggering (i.e., time delay) of $\frac{NV}{2}$ relative to the real part of the signal.
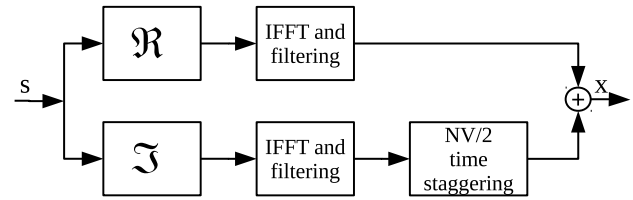
Fig. 1. Synthesis of FBMC signal using IFFT, filtering and time staggering

C. Peak-to-average-power ratio

PAPR is a common metric to characterize the amplitude fluctuations of the signal. Highly dynamic fluctuations increase the required power reserve (back-off) of power amplifiers. Distortions caused by the nonlinear behaviour of the amplifier result in increased out of band radiation (spectrum regrowth), which defeats one of the primary goals of FBMC (i.e., very low adjacent channel leakage) as well as causing intercarrier interference which further degrades the quality of transmission.

The PAPR (in decibel) for OFDM is defined on a per symbol basis as follows:

$$\text{PAPR}_1 = 10\log_{10}\left(\frac{\max\limits_{0 \le k \le NV-1}\left\{|x[k]|^2\right\}}{\frac{1}{NV}\sum\limits_{k=0}^{NV-1}|x[k]|^2}\right), \qquad (3)$$

where $|\cdot|$ is the magnitude of the signal.

On the other hand, the overlap between adjacent symbols in FBMC raises a question about unambiguously defining the PAPR of FBMC. This issue is further complicated by the presence of filter transients at the beginning and end of each frame.

For FBMC only the steady state part is taken into account, thus the first and last L samples (which are transient parts caused by the filters) are discarded. This means that it only makes sense to calculate the PAPR for at least $2K + NV$ samples. After discarding the transients, the rest of the signal is divided into blocks of length NV. This provides a good comparison with OFDM-like signals where the symbols are orthogonal to each other. The PAPR for FBMC is then defined as:

$$\text{PAPR}_2 = 10\log_{10}\left(\frac{\max\limits_{mNV \le k \le (m+1)NV-1}\left\{|x[k]|^2\right\}}{\frac{1}{NV}\sum\limits_{k=mNV}^{(m+1)NV-1}|x[k]|^2}\right), \qquad (4)$$

$$K \le m \le M - K - 1.$$

III. PAPR REDUCTION

An approach to reduce the PAPR is to minimize the numerator of (3) and (4) for OFDM and FBMC, respectively. To address this problem, the "correction term" y is added the original signal x and then E, the instantenous energy of the

complex baseband signal is minimized. The general problem formulation becomes

$$\text{minimize } E \qquad (5)$$
$$|x[k] + y[k]|^2 \leq E, \ 0 \ \leq k \ \leq T - 1.$$

Both the TR and ACE schemes fit into this framework by posing constraints on y. The demodulated (frequency domain) symbols corresponding to y are denoted with t. Then TR and ACE methods can be formulated in the following way.

A. Active constellation extension

The general criterion for ACE restricts the Euclidean distance between the constellation points being not smaller than the original distance. For QPSK modulation the original points and the corresponding extension regions are depicted in Fig. 2 with black dots and grey shading, respectively. For 16QAM alphabet the rule is more sophisticated. For 16QAM the extension regions are shown in Fig. 3. First of all the four closest constellation points to the origin are not involved (since the movement in any direction would decrease the distance to some of the other points), these are marked with white circles in the figure. For the four corner points the same rule applies as for QPSK. The rest of the points have one degree of freedom, thus they can move outwards in the directions depicted with dashed lines. If the minimization in (5) is performed applying the ACE constraints, the original symbols s are modified to $t^{ACE} = s + t$ in order to obtain the PAPR reduced signal.

B. Tone reservation

In the tone reservation scheme a number of tones/subcarriers, are reserved specifically for PAPR reduction purposes and thus these carriers do not take part in data transmission. Let t_R be the set of reserved subcarrier indices and $n_{res} = |t_R|$ the number of reserved tones. The symbols on the reserved carriers are zero initially $s_n = 0$ for $n \in t_R$. Then the criterion for TR becomes

$$t_n^{TR} = \begin{cases} s_n \ , & \text{if } n \notin t_R \\ \text{arbitrary}, & \text{if } n \in t_R \end{cases}. \qquad (6)$$

C. Joint use of TR and ACE

The constraints for TR are more permissive on the reserved tones than those imposed by the ACE, thus the two methods can be used jointly, ideally resulting in even lower PAPR values. In this case the constraints are combined in the following way:

$$t_n^{TRACE} = \begin{cases} t_n^{ACE} \ , & \text{if } n \notin t_R \\ t_n^{TR}, & \text{if } n \in t_R \end{cases}. \qquad (7)$$

Both schemes share the same favourable property that the receiver architecture does not need any modifications, only the indices of the reserved tones must be known in the receiver in order to discard them. However, both schemes increase the average power of the transmitted signal and TR introduces data rate loss since the reserved tones do not carry useful data.

IV. PROBLEM FORMULATION AND OPTIMAL SOLUTION

A. Problem formulation for OFDM

Let F^{-1} be the $NV \times N$ IDFT matrix. Then we can reformulate (1) using matrix operations to $x = F^{-1}s$. Using this notation the QCQP for PAPR reduction to a single OFDM symbol can be formulated based on [7] as:

$$\text{minimize } E$$
$$\text{subject to}$$
$$\begin{bmatrix} x & F^{-1} & -I \end{bmatrix} \begin{bmatrix} 1 \\ t \\ a \end{bmatrix} = 0$$
$$E \geq |a_k|^2, \qquad (8)$$

where a is an auxiliary variable to express the amplitude of the signal. The instantenous magnitude $|a_k|^2$ is upper bounded by E which is minimized. The described for ACE in III-A and TR in (6) are applied on t:

- TR:
  $-\infty \leq t_{t_R} \leq \infty, t_R = \{\text{reserved indices}\}$

Fig. 2.   ACE extension regions for QPSK modulation
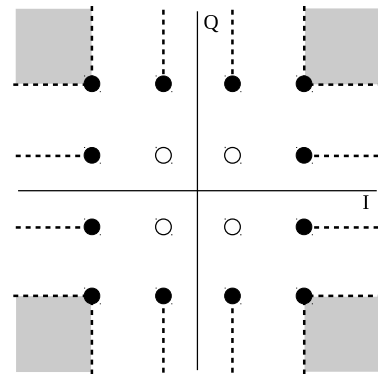
Fig. 3.   ACE extension regions for 16QAM modulation

- ACE (QPSK):
  $\Re\{t_{R_P}\} \geq 0,\quad R_P = \{n \mid \mathrm{sign}(t_{re,n}) = 1\},$
  $\Re\{t_{R_N}\} \leq 0,\quad R_N = \{n \mid \mathrm{sign}(t_{re,n}) = -1\},$
  $\Im\{t_{I_P}\} \geq 0,\quad I_P = \{n \mid \mathrm{sign}(t_{im,n}) = 1\},$
  $\Im\{t_{I_N}\} \leq 0,\quad I_N = \{n \mid \mathrm{sign}(t_{im,n}) = -1\}.$

- ACE (16QAM):
  corner points:
  $\Re\{t_{R_P}\} \geq 0,\quad R_P = \{n \mid t_{re,n} = 3\},$
  $\Re\{t_{R_N}\} \leq 0,\quad R_N = \{n \mid t_{re,n} = -3\},$
  $\Im\{t_{I_P}\} \geq 0,\quad I_P = \{n \mid t_{im,n} = 3\},$
  $\Im\{t_{I_N}\} \leq 0,\quad I_N = \{n \mid t_{im,n} = -3\}.$
  additionally for side points:
  $\Im\{t_{R_{S1}}\} = 0,\quad R_{S1} = \{n \mid t_{re,n} = 1\},$
  $\Im\{t_{R_{S2}}\} = 0,\quad R_{S2} = \{n \mid t_{re,n} = -1\},$
  $\Re\{t_{I_{S1}}\} = 0,\quad I_{S1} = \{n \mid t_{im,n} = 1\},$
  $\Re\{t_{I_{S2}}\} = 0,\quad I_{S2} = \{n \mid t_{im,n} = -1\}.$
  inner points:
  $t_Z = 0,\quad Z = \{n \mid t_{re,n} = 1 \wedge t_{im,n} = 1\}.$

Since the two constraints – ACE and TR – are independent, they can be applied at the same time as well.

B. Problem formulation for FBMC

In order to extend the problem formulation to FBMC signals we propose a way to express FBMC signal synthesis in a linear algebraic form. First, polyphase decomposition allows us to express the filtering procedure with a single matrix. We denote the filter matrix as

$$P = \begin{bmatrix} \mathrm{diag}(\,p[0],\ p[1],\ \ldots,\ p[NV{-}1]) \\ \mathrm{diag}(\,p[NV],\ p[NV{+}1],\ \ldots,\ p[2NV{-}1]) \\ \vdots \\ \mathrm{diag}(p[(K{-}1)NV], p[(K{-}1)NV{+}1], \ldots, p[KNV{-}1]) \end{bmatrix},$$

where $p[i]$ is the ith tap of the prototype filter and $\mathrm{diag}(\cdot)$ denotes the diagonal matrix of the elements. There are K pieces of $NV \times NV$ submatrix resulting in P, a $KNV \times NV$ matrix. As seen in the FBMC signal definition in (2) the symbols are also phase rotated with θ, thus the P filter matrix is multiplied by such a phase rotation matrix accordingly:

$$H_1 = P \cdot F^{-1} \cdot \mathrm{diag}\left(\theta^0, \theta^1, \ldots, \theta^{N-1}\right) \text{ and}$$
$$H_2 = P \cdot F^{-1} \cdot \mathrm{diag}\left(\theta^1, \theta^2, \ldots, \theta^{N}\right),$$

thus we obtain matrices to construct the two staggered portions, respectively. To embed the staggering to the matrix operation we append zeros to the matrices:

$$H_1' = \begin{bmatrix} H_1 \\ 0_{NV/2 \times N} \end{bmatrix}, H_2' = \begin{bmatrix} 0_{NV/2 \times N} \\ H_2 \end{bmatrix}.$$

The zeros at the beginning of H_2' introduce the time shift, whereas the zeros at the end of H_1' are needed to match the dimensions with H_2', so the inphase and the staggered part can be summed to create an FBMC signal. In order to express the final synthesis operator – whereby an arbitrary number of FBMC subsymbols can be summed up – we define the auxiliary matrices

$$H_A^q = \begin{bmatrix} 0_{NV \times qN} \\ H_1' \\ 0_{NV \times (M-q-1)N} \end{bmatrix}, H_B^q = \begin{bmatrix} 0_{NV \times qN} \\ H_2' \\ 0_{NV \times (M-q-1)N} \end{bmatrix}.$$

With these matrices an FBMC subsymbol can be synthesized with a 'tail' of zeros of $M - 1$ subsymbol length. The M-fold augmentation leads to the band matrices

$$H_{F1} = \left[\; H_A^0 \;\middle|\; H_A^1 \;\middle|\; \ldots \;\middle|\; H_A^{M-1} \;\right],$$

$$H_{F2} = \left[\; H_B^0 \;\middle|\; H_B^1 \;\middle|\; \ldots \;\middle|\; H_B^{M-1} \;\right].$$

Thus the synthesis of an entire frame consisting of M subsymbols can be expressed as

$$x = H_{F1}s_{re} + H_{F2}s_{im}, \tag{9}$$

where s_{re} and s_{im} are the real and imaginary parts of the frequency domain symbols s for the whole frame, respectively, i.e., for M subsequent symbols. For a better understanding, the first term of the addition in (9) is illustrated in Fig. 4. The second term of the addition is similar except H_1' and s_{re} are replaced with H_2' and s_{im}, respectively.

Let $t = t_{re} + j \cdot t_{im}$ represent the frequency domain symbols throughout an entire frame belonging to the time domain signal y. To sum up the signal synthesis, the PAPR minimization problem and the constraints for the two methods we get the QCQP in the following form:

$$\text{minimize } E$$
$$\text{subject to}$$
$$\begin{bmatrix} x & H_{F1} & H_{F2} & -I \end{bmatrix} \begin{bmatrix} 1 \\ t_{re} \\ t_{im} \\ a \end{bmatrix} = 0$$
$$E \geq |a_k|^2 \tag{10}$$

For FBMC case the same criterion on ACE and TR can be used as described in (8).

It can be shown that E is a convex function of t_{re} and t_{im}. Since $H_{F1}t_{re} + H_{F2}t_{im}$ and the addition of x and subtraction of a are linear functions, they preserve convexity. Then the absolute value of the complex vector $a = a_{re} + j \cdot a_{im}$ is squared, again preserving convexity. Thus E is a convex function of t_{re} and t_{im} which guarantees that the problem has a unique global optimum.

In the simulations three cases are covered: using only ACE or TR constraints and using both constraints at the same time which is denoted as TR-ACE.

Establishing Lower Bounds on the Peak-to-Average-Power
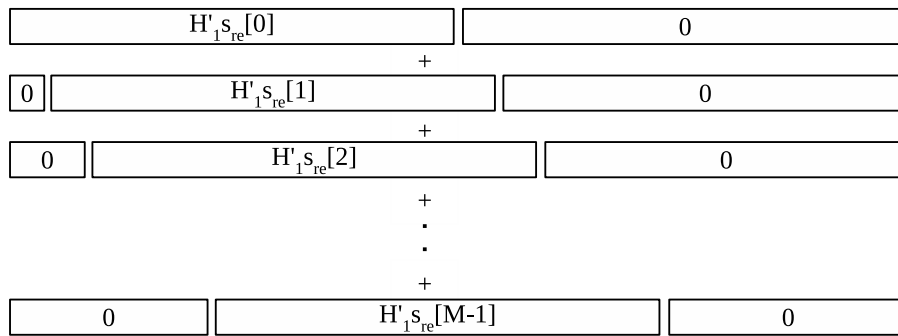Ratio in Filter Bank Multicarrier Systems

$H'_1 s_{re}[0]$	0

$+$

0	$H'_1 s_{re}[1]$	0

$+$

0	$H'_1 s_{re}[2]$	0

$+$
.
.
.
$+$

0	$H'_1 s_{re}[M-1]$	0

Fig. 4. FBMC frame synthesis using the real part of frequency domain symbols

V. SIMULATION RESULTS

For the simulations we use the PHYDYAS prototype filters and the signal parameters described in Table I. In case of FBMC as the number of symbols per frame M increases, the complexity of the optimization problem described in (10) grows rapidly. Also in practical systems (e.g. 3GPP LTE) due to fine grained resource allocation frames consist of small number of symbols (in the order of tens). Thus for evaluation purposes we chose $M = \{8, 12\}$ symbols per frame for FBMC signals. For a given frame size, the M symbols in the frame are jointly optimized which is needed because of the inherent overlapping of the signals. The results were obtained for both QPSK and 16QAM modulation alphabet. For the OFDM case the frame size is not relevant, since the problem can be solved on a per symbol basis. In order to achieve accurate PAPR values an oversampling rate of 4 was applied.

In each case the QCQP program was solved with MOSEK 7 [16] solver using the interior point method. For evaluation purposes we use the complementary cumulative distribution function (CCDF) of the PAPR which is calculated for OFDM and FBMC based on (3) and (4), respectively. The results of PAPR reduction for OFDM with QPSK modulation is shown in Fig. 5. It can be seen that the TR and the ACE scheme alone at 10^{-2} probability results in approximately 4.5 dB and 6 dB reduction, respectively whereas the TR-ACE brings less than 0.3 dB improvement, compared to using ACE only.

In Fig. 7 and Fig. 8 the PAPR reduction results for FBMC with QPSK modulation are shown for $M = \{8, 12\}$ symbols per frame, respectively. The order of performance is the same as in the case of OFDM (in descending order: TR, ACE, TR-ACE), and the amount of improvement is approximately the same for both frame sizes which is 3 dB for TR, 6.2 dB for ACE and TR-ACE performs about by 0.3 dB better than using ACE only.

The results show that for QPSK modulation practically the same amount of PAPR reduction can be achieved in FBMC as in OFDM however, the lower limit for TR is approximately 1 dB higher in FBMC compared to OFDM. Thus the overlapping nature of FBMC is not a limiting factor when using TR or/and ACE schemes, and significant PAPR reduction can be achieved.
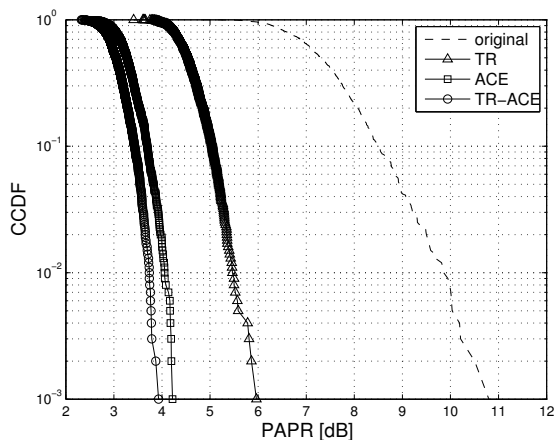
Fig. 5. CCDF of PAPR for original and PAPR reduced QPSK modulated OFDM signal
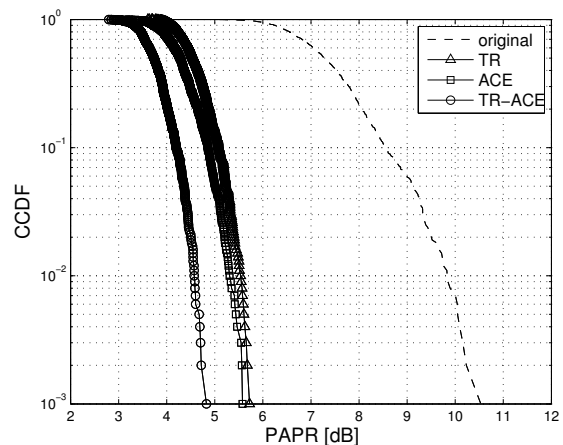
Fig. 6. CCDF of PAPR for original and PAPR reduced 16QAM modulated OFDM signal
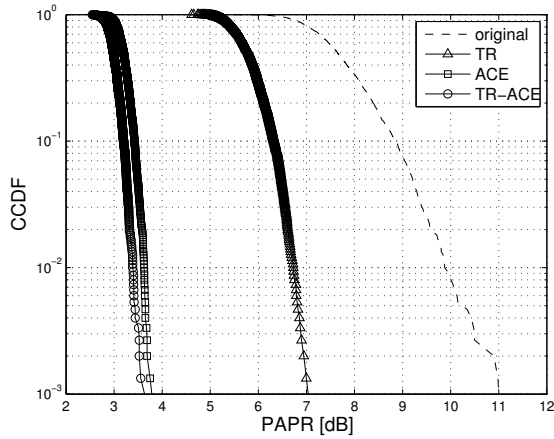
Fig. 7. CCDF of optimized PAPR with $M = 8$ FBMC symbols per frame with QPSK modulation
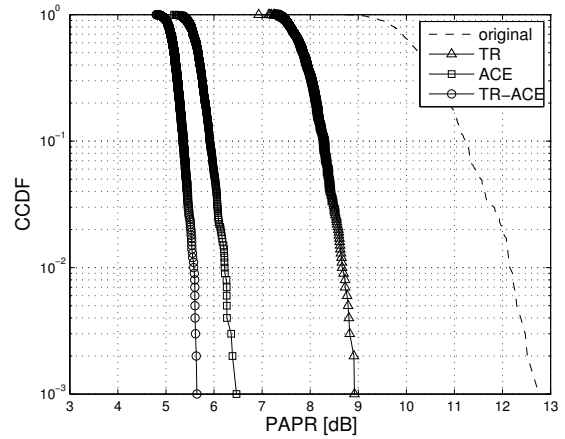
Fig. 9. CCDF of optimized PAPR with $M = 8$ FBMC symbols per frame with 16QAM modulation
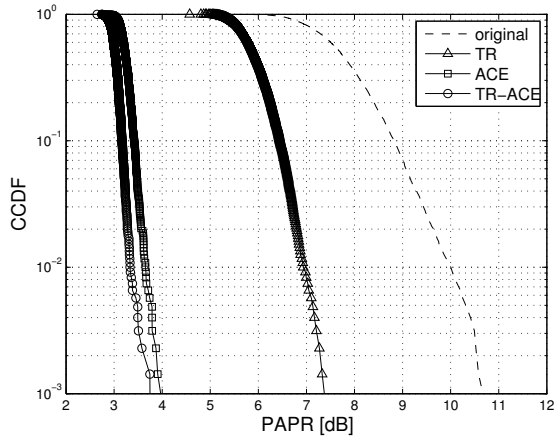
Fig. 8. CCDF of optimized PAPR with $M = 12$ FBMC symbols per frame with QPSK modulation
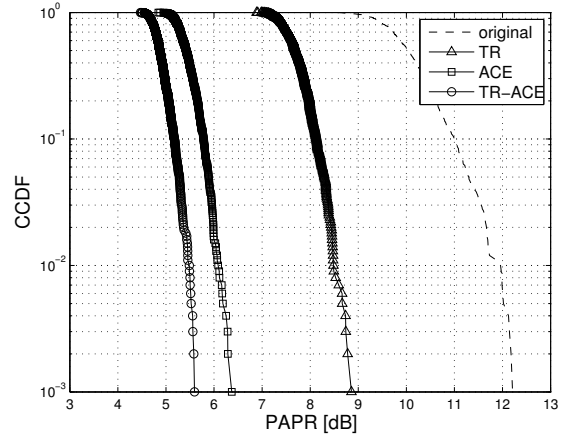
Fig. 10. CCDF of optimized PAPR with $M = 12$ FBMC symbols per frame with 16QAM modulation

In Fig. 6 PAPR reduction results for OFDM with 16QAM modulation is shown. It can be seen that the TR method is more efficient for 16QAM than for QPSK, since there is 1 dB improvement in the reduction. Because the ACE scheme for this modulation alphabet has an effect only on the outer constellation points, thus it is less efficient than for the QPSK case (the difference is about 1.5 dB). The TR-ACE constraints are still the most effective and exhibit as much as 5 dB PAPR reduction (at 10^{-2} probability).

For FBMC the results for 16QAM modulation for $M = \{8, 12\}$ are shown in Figs. 9 and 10, respectively. In this case the results are very similar to the QPSK case, only the PAPR reduction capabilites are less by approximately 1.5-2 dB. This is also due to the ACE scheme has a limited set of constellation points to work on. For this modulation alphabet, there is no significant difference between the $M = 8$ and $M = 12$ cases.

Compared to the 16QAM OFDM the ACE and TR-ACE show impressive PAPR reduction potential, whereas the TR scheme is less efficient for FBMC, still delivering as much as 3 dB reduction.

VI. CONCLUSIONS

In this paper we formulated the PAPR reduction problem for inherently overlapping FBMC signals. Based on this improvement we solved the QCQP for short FBMC frames and showed a lower limit of PAPR in presence of TR or/and ACE constraints. As a comparison we showed the results with the same parameters and constraints for OFDM signals. These results revealed that there is only minor difference in the performance of the PAPR reduction schemes between OFDM and FBMC. In case of QPSK approximately the same amount

Establishing Lower Bounds on the Peak-to-Average-Power
Ratio in Filter Bank Multicarrier Systems

TABLE I.   SIMULATION PARAMETERS

parameter	FBMC	OFDM
no. of subcarriers $[N]$	64	64
frame size $[M]$	8,12	1
overlapping factor $[K]$	4	0
no. of reserved tones $[n_{res}]$	5	5
oversampling rate $[V]$	4	4
no. of realizations	1000	1000
modulation alphabet	QPSK, 16QAM	QPSK, 16QAM

of PAPR reduction can be achieved by using ACE or TR-ACE, however the TR method is at least 1 dB less efficient for FBMC. The lower bounds for 16QAM are higher in for both modulations, but in this case the ACE and TR-ACE schemes result in at least 0.5 dB less reduction compared to OFDM. Also the efficiency of TR for 16QAM is more than 3 dB less for FBMC. As the amount of reduction achieved by optimization is computationally complex, they should be considered as baselines for any real-time applicable algorithm developed using the aforementioned constraints.

REFERENCES

[1] P. Banelli, S. Buzzi, G. Colavolpe, A. Modenini, F. Rusek, and A. Ugolini, "Modulation formats and waveforms for 5G networks: Who will be the heir of OFDM?: An overview of alternative modulation schemes for improved spectral efficiency," *Signal Processing Magazine, IEEE*, vol. 31, pp. 80–93, Nov 2014.

[2] S. Krishna Chaitanya Bulusu, H. Shaiek, D. Roviras, and R. Zayani, "Reduction of PAPR for FBMC-OQAM systems using dispersive SLM technique," in *Wireless Communications Systems (ISWCS), 2014 11th International Symposium on*, pp. 568–572, Aug 2014.

[3] N. van der Neut, B. Maharaj, F. de Lange, G. Gonzlez, F. Gregorio, and J. Cousseau, "PAPR reduction in FBMC using an ACE-based linear programming optimization," *EURASIP Journal on Advances in Signal Processing*, vol. 2014, no. 1, 2014.

[4] Z. Kollar, L. Varga, B. Horvath, P. Bakki, and J. Bito, "Evaluation of clipping based iterative PAPR reduction techniques for FBMC systems," *The Scientific World Journal*, vol. 2014, p. 12, January 2014.

[5] D. Qu, S. Lu, and T. Jiang, "Multi-block joint optimization for the peak-to-average power ratio reduction of FBMC-OQAM signals," *Signal Processing, IEEE Transactions on*, vol. 61, pp. 1605–1613, April 2013.

[6] Y. Zhou, T. Jiang, C. Huang, and S. Cui, "Peak-to-average power ratio reduction for OFDM/OQAM signals via alternative-signal method," *Vehicular Technology, IEEE Transactions on*, vol. 63, pp. 494–499, Jan 2014.

[7] B. Krongold and D. Jones, "PAR reduction in OFDM via active constellation extension," *IEEE Transactions on Broadcasting*, vol. 49, pp. 258–268, Sept. 2003.

[8] J. Y. K. S.-E. Park, Y. Sung-Ryul, D. S. Park, and P. Y. Joo, "Tone reservation method for PAPR reduction scheme," tech. rep., IEEE 802.16e Task Group, IEEE 802.16e-03n60, Oct. 2003.

[9] M. Petermann, D. Wubben, and K. D. Kammeyer, "Joint constellation extension and tone reservation for PAPR reduction in adaptive OFDM systems," in *IEEE 10th Workshop on Signal Processing Advances in Wireless Communications, SPAWC '09*, pp. 439–443, 2009.

[10] B. Horvath, Z. Kollar, and P. Horvath, "Bridging the gap between optimal and suboptimal ACE PAPR reduction scheme for OFDM," in *Radioelektronika (RADIOELEKTRONIKA), 2014 24th International Conference*, pp. 1–4, April 2014.

[11] N. van der Neut, B. Maharaj, F. de Lange, G. Gonzalez, F. Gregorio, and J. Cousseau, "PAPR reduction in FBMC systems using a smart gradient-project active constellation extension method," in *Telecommunications (ICT), 2014 21st International Conference on*, pp. 134–139, May 2014.

[12] S. Lu, D. Qu, and Y. He, "Sliding window tone reservation technique for the peak-to-average power ratio reduction of FBMC-OQAM signals," *Wireless Communications Letters, IEEE*, vol. 1, pp. 268–271, August 2012.

[13] B. Farhang-Boroujeny, "OFDM versus filter bank multicarrier," *IEEE Signal Processing Magazine*, vol. 28, no. 3, pp. 92–112, 2011.

[14] M. Bellanger, M. Renfors, T. Ihalainen, and C. A. F. da Rocha, "OFDM and FBMC transmission techniques: a compatible high performance proposal for broadband power line communications," in *Proc. IEEE Int Power Line Communications and Its Applications (ISPLC) Symp*, pp. 154–159, 2010.

[15] Y. Dandach and P. Siohan, "FBMC/OQAM modulators with half complexity," in *2011 IEEE, Global Telecommunications Conference (GLOBECOM 2011)*, pp. 1–5, dec. 2011.

[16] MOSEK ApS, *The MOSEK optimization toolbox for MATLAB*, 2015.

Bálint HORVÁTH received his BSc and MSc from electrical engineering from the Budapest University of Technology and Economics in 2010 and 2013, respectively. He is currently working towards his PhD at the Department of Broadband Infocommunications and Electromagnetic Theory. His research interests include signal processing, wireless communications and software defined radio.

Péter HORVÁTH received his PhD degree from the Budapest University of Technology and Economics where he is currently an associate professor at the Department of Broadband Infocommunications and Electromagnetic Theory. His research interests include wireless channel modeling, multi-antenna techniques, physical layer aspects of cognitive radio and wireless cyber-physical systems.

Sum-rate Performance of Large Centralized and Distributed MU-MIMO Systems in Indoor WLAN

Qing Wang, *Student Member, IEEE*, Diptanil Debbarma, Anthony Lo, Ignas Niemegeers, Sonia Heemstra de Groot

Abstract - Large MIMO systems are recognized as an effective technique for increasing the spectral and energy efficiency of wireless networks. The attractiveness of this technique for WLAN is that it can be an alternative approach to cell densification for providing high data rate wireless access. Here we consider large MIMO systems in indoor WLANs for multi-user MIMO (MU-MIMO) spatial multiplexing in the 2.4 GHz ISM band. The focus is on analyzing the behaviors of large MIMO systems with both centralized and distributed antenna system (CAS and DAS) architectures. The analysis is based on extensive ray-tracing channel simulations, as well as an i.i.d. Rayleigh model. The numerical results show that the optimum capacity can be closely approached with both CAS and DAS architectures when the number of Access Point (AP) antennas exceeds the users by a few times. DAS is found to be superior to CAS in that the required number of antennas is significantly smaller, and especially performs better in non-rich scattering channels which is the case of practical channels reflected by ray-tracing simulations.

Index Terms – **MU-MIMO, large MIMO, centralized antenna system, distributed antenna system, WLAN**

I. INTRODUCTION

Large MIMO has been advocated recently as a promising technique for next generation wireless networks due to its manifold benefits, especially the potential of a tremendous boost of spectral efficiency and energy efficiency [1] [2]. This technique brings at least two fundamental changes to the traditional MIMO scheme [1]. First, a large number of antennas are employed at the base station (BS) or access point (AP), say tens to hundreds or even more. Traditional MIMO systems typically have only a small number, e.g., maximally 8 in the latest WiFi standard IEEE 802.11ac (for frequency bands below 6 GHz). Potentially, the capacity can be increased multiple times with higher order spatial multiplexing in large MIMO. Second, the number of BS or AP antennas is much larger than the number of co-scheduled mobile stations (STAs), say 10 times more. Traditional MIMO systems usually assume a similar or equal numbers of transmit and receive antennas. The additional antennas make it possible to use linear precoding to achieve high data rate, which reduces the signal processing complexity in high-dimensional MIMO. Large MIMO has now been recognized as

a promising technique for next-generation cellular networks or 5G, however, its use in WLAN is rarely discussed in the literature at this time.

The attractiveness of large MIMO for WLAN is that it can be an alternative approach for cell densification to provide high data rate access, especially for high user density scenarios like airport gates, train stations, crowded office buildings, etc. A basic problem of cell densification is that the network may have degraded performance by intra- and inter-cell interference due to poorly-coordinated transmissions. On the contrary, in large MIMO, the cooperation of a large number of antennas can sharply focus signals onto the intended users and cancel the undesired signals in almost all other directions. As a result, not only a larger number of parallel spatial streams can be supported but also the data rate of each stream can be significantly improved to guarantee the quality-of-service (QoS) for simultaneously served users.

The objective of this paper is to analyze the behavior of large MIMO systems in WLAN, and verify the viability of achieving the optimum capacity with a reasonable number of antennas for multi-user MIMO (MU-MIMO) spatial multiplexing. Unlike cellular networks which consider outdoor environments, licensed frequency bands, and relatively large cells, WLAN mainly aims at indoor environments and applications, and use license-free bands. Therefore, the discussions in this paper differ from the prior work for cellular networks reported in [3] [4] [5]. Moreover, [3] and [4] only consider centralized antenna system (CAS) architecture, and [5] only uses theoretical channel models. Our work differs in another two aspects. First, we consider both CAS and DAS architectures. Second, we use both practical and theoretical MIMO channels, to highlight the performance differences in practical and ideal channel conditions. The practical indoor wireless channels are simulated by ray-tracing software, which can characterize large MIMO channels with good accuracy as verified in [6]. The theoretical MIMO channel model combines the i.i.d. Rayleigh small-scale fading model, and the path loss results obtained from ray-tracing simulations, to obtain the ideal channel condition. Above that, the deployment of the antennas is optimized based on the received signal strength over the coverage area to better fit antennas into the indoor environment. We find that, a large number of STAs can be supported simultaneously and achieve the optimum capacity with a limited number of antennas for both CAS and DAS architectures. The results, however, show a significant advantage of DAS architecture over CAS, especially in practical channels.

The remainder of this paper is organized as follows. Section

II provides the system model and the sum-rate capacity metrics for the subsequent analysis. Section III presents the channel simulation methods with a ray-tracing tool, and the modeling of the ideal MIMO channel. Section IV examines the numerical results we obtained. Section V concludes the paper and highlights remaining important issues that need to be investigated.

II. SYSTEM MODEL

We consider a single cell or single AP WLAN with CAS and DAS architectures, illustrated in Fig. 1. For DAS systems, the remote antenna units (RAUs) or antenna clusters are typically connected by wirelines to the AP. In particular, optical fiber is a promising wireline connection that has been advocated in recent years [7]. We denote the number of RAUs, the number of antennas per RAU, and the number of co-scheduled single-antenna STAs by M, N and K, respectively. So the total number of AP antennas is MN. CAS is taken as a special case that $M = 1$, then N equals the total number of antennas.

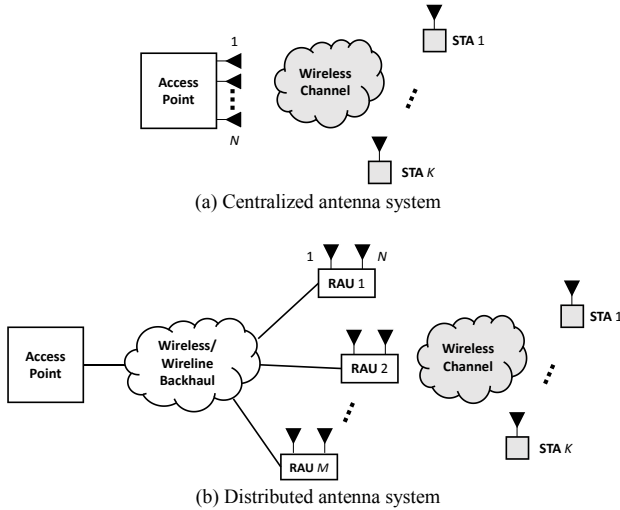(a) Centralized antenna system

(b) Distributed antenna system

Fig. 1 Architecture of CAS and DAS for WLAN.

In a CAS, the antennas of an AP are co-located, typically with half-wavelength spacing between individual antennas. As a result, the antennas of the AP usually share the same large scale fading for the same user, and small scale fading variations are correlated across the antennas. The channel correlation renders the MIMO channel of low rank which limits the spatial multiplexing gain. So in traditional MIMO systems, user scheduling is used to select the users that are well separated spatially, so as to obtain more "favorable" MIMO channels. This requirement is however much relaxed in large MIMO [1].

In a DAS, the antennas are clustered in the RAUs, and the RAUs are scattered over the coverage area. The antenna separation in a RAU is small, typically with half-wavelength, but the RAUs are separated by distances of at least several meters. The MIMO system can then benefit from two facts. First, the macro-diversity due to the large separation of RAUs which reduces the average path loss to the users thus improves the average received signal strength. Second, the micro-diversity improves the independence of small scale fading across the antennas at different RAUs, which lowers MIMO channel correlation. Therefore, the DAS architecture is superior to the CAS architecture for traditional MIMO systems, which has been confirmed in the studies like [8]. Evidently, the cost is the higher complexity of the infrastructure.

The following assumptions are made for our modeling and analysis:

- The K co-scheduled STAs are selected by random scheduling, i.e., without optimization based on the spatial separability of the STAs, since large MIMO potentially can achieve the optimum performance without sophisticated user scheduling as in traditional MIMO systems. In addition, the STAs are uniformly distributed over the entire area. We leave the discussions on non-uniform distributions for our future research.

- We assume global sum power constraint over all the antennas. This assumption leads to a much lower complexity in computing the precoding matrix [9]. In addition to that, we also argue that the transmission power of the antennas is extremely low in large MIMO systems due to the high beamforming gain with the numerous antennas and the reduced path loss in DAS systems especially for indoor WLAN setups, which makes the assumption also reasonable in practice.

- To simplify the analysis, we assume the backhaul connection in the DAS architecture is ideal. For example, delays across the RAUs are assumed equal and the bandwidth is sufficiently large; optical fiber distortions are already compensated [10]. In addition, the constraints like channel estimation accuracy and power regulations on EIRP, are not considered in order to keep a clear focus in the analysis.

A. Signal Model

The signal model is given in the following for block-fading narrow-band channels. The block-fading channel model is suitable for indoor channels due to the slow user mobility and physical environment changes. The extension of the narrow band model to OFDM systems is straightforward. In the numerical analysis, we will consider OFDM modulation, and use equal power allocation to the subcarriers. In addition, the models are given assuming perfect channel knowledge is known.

Denote the full channel matrix by $\mathbf{G} = [\mathbf{g}_1, \cdots, \mathbf{g}_K]$, where $\mathbf{g}_k, k = 1, \cdots, K$ is the channel vector of the k th STA. The channel coefficients consist of both large scale fading and small scale fading. Specifically,

$$\mathbf{g}_k = \left[\beta_{1k} \mathbf{h}_{1k}^T, \cdots, \beta_{Mk} \mathbf{h}_{Mk}^T \right]^T \qquad (1)$$

where β_{mk} is the large scale fading and $\mathbf{h}_{mk}$ is the small scale fading vector between the m th RAU and the k th STA, respectively. The received signal at the STAs is

$$\mathbf{y} = \mathbf{G}^H \mathbf{x} + \mathbf{n} \qquad (2)$$

where $\mathbf{x}$ is the precoded signal vector, $\mathbf{n}$ is the Gaussian noise vector with i.i.d. elements following $\mathcal{CN}(0, \sigma^2)$ and σ^2 is the noise power.

B. Sum-rate Capacity

Sum-rate capacity is the total achievable data rate of all the co-scheduled STAs (measured in bps/Hz). In this paper, it is evaluated under different conditions to give a comprehensive view. Specifically, we take into account of the interference-free (IF) case, and different precoding techniques including DPC (Dirty Paper Coding), ZF (Zero-forcing) and MBF (matched beamforming), which are elaborated in the following.

1) IF

IF capacity is the best performance that can be achieved if all the channel energy to STA k is delivered to STA k but without any multi-user interference (MUI), which is usually used as a benchmark [1]. With such assumption, the data rate for the k th STA is given by

$$R_{\mathrm{IF},k} = \log_2\left(1 + \frac{p_k \|\mathbf{g}_k\|^2}{\sigma^2}\right) \quad (3)$$

where p_k is the transmission power allocated for the k th STA, which is assumed to be equal for all STAs, so $p_k = P_t / K$, for $k = 1,\cdots,K$ and P_t is the total transmission power. The sum-rate is then given by

$$C_{\mathrm{sum,IF}} = \sum_{k=1}^{K} R_{\mathrm{IF},k} \quad (4)$$

2) DPC

DPC is the optimum non-linear precoding technique which gives the upper bound capacity for a given channel. The sum-rate is usually given in the following form

$$C_{\mathrm{sum,DPC}} = \max_{\mathbf{P}} \log_2 \det\left(\mathbf{I} + \frac{1}{\sigma^2}\mathbf{G}\mathbf{P}\mathbf{G}^H\right) \quad (5)$$

where $\mathbf{P}$ is a diagonal matrix representing the power allocation to the STAs, i.e., $\mathbf{P} = \mathrm{diag}\{p_1,\cdots,p_K\}$, constrained by $\sum_{k=1}^{K} p_k = P_t$. The optimum power allocation can be found by the water-filling algorithm [4]. In the high SNR regime, it can be approximated by [11]

$$C_{\mathrm{sum,DPC}} = \log_2 \det\left(\mathbf{I} + \frac{P_{\mathrm{total}}}{K\sigma^2}\mathbf{G}\mathbf{G}^H\right) \quad (6)$$

i.e., with equal power allocations to the STAs.

3) Linear Precoding

Linear precoding techniques are more favorable in practice due to their low complexity. In this paper, we consider ZF and MBF, which precode the signal with different objectives. Specifically, ZF only cancels MUI but neglecting the final SINRs of the STAs, and MBF only considers SNR maximization for individual STAs but without taking into account MUI. Although suboptimal, they are potentially able to achieve the optimum capacity performance in large MIMO regime, i.e., when $MN \gg K$ (see [1] for more information).

For linear precoding, we can write the received signal model as

$$\mathbf{y} = \mathbf{G}^H \mathbf{W} \mathbf{P}^{1/2}\mathbf{s} + \mathbf{n} \quad (7)$$

where $\mathbf{s}$ is the information symbol, and $\mathbf{W}$ is the beamforming matrix. Therefore, the SINR of the k th STA is given by

$$\mathrm{SINR}_k = \frac{|\mathbf{g}_k^H \mathbf{w}_k|^2 \, p_k}{\sum_{j\neq k}|\mathbf{h}_k^H \mathbf{w}_j|^2 \, p_j + \sigma^2} \quad (8)$$

The beamforming matrix $\mathbf{W}$ is obtained through the following procedure. First, the precoding matrices of MBF and ZF are calculated by

$$\tilde{\mathbf{W}}_{\mathrm{MBF}} = \mathbf{G} \quad (9)$$

$$\tilde{\mathbf{W}}_{\mathrm{ZF}} = \mathbf{G}(\mathbf{G}^H\mathbf{G})^{-1} \quad (10)$$

Then, the columns are normalized to achieve unit power of beamforming vectors. Specifically, in the final beamforming matrices, $\mathbf{W}_{\mathrm{ZF}}$ and $\mathbf{W}_{\mathrm{MBF}}$, the columns are obtained by $\mathbf{w}_k = \tilde{\mathbf{w}}_k / \|\tilde{\mathbf{w}}_k\|$. Since for ZF, $\mathbf{h}_i^H \mathbf{w}_j = 0$ for $i \neq j$, the first term of the denominator of the Eq. (8) will be zero.

Finally, the sum-rate is calculated by

$$C_{\mathrm{sum,ZF/MBF}} = \sum_{k=1}^{K} \log_2(1 + \mathrm{SINR}_{k,\mathrm{ZF/MBF}}) \quad (11)$$

In addition, equal power allocation is assumed for the linear precoders as well in the analysis.

III. CHANNEL MODELS

Channel modeling is important for investigating the performance of MIMO systems. As already pointed out in [4] [12], the channel conditions of the STAs, e.g., line-of-sight (LOS) and none-line-of-sight (NLOS), have noticeable effect on the achievable data rates. In this paper, both ray-tracing channel simulation and an ideal channel model are used. Ray-tracing simulation based channel modeling stands for the characterization of more practical channels, in contrast to the ideal channel condition.

A. Ray-tracing Simulation

The ray-tracing simulations are conducted in a 3D ray-tracing tool named Radiowave Propagation Simulator (RPS) [13]. To make the simulations more scalable, the channel transfer functions are derived with the following steps. First, the locations of the M RAUs are optimized according to received signal strength. Specifically, we locate the RAUs on 5m grids on the ceiling plane of the indoor scenario (see Fig. 2), assuming each RAU has a single isotropic antenna and the same transmission power. Then, the group of RAU positions that provides the highest 5-percentile receive signal power over the entire coverage area is selected. The searching algorithm used here is "greedy search", which iteratively adds one RAU to maximize the objective function (see [14] for more details). A reason why we choose this algorithm is that it is deterministic, which yields reproducible optimization results. Second, the band-limited time-domain channel impulse responses (CIR) between each RAU and each STA position are derived from RPS, along with angular (departure and arrival angles) and temporary information of all the rays. Third, the channels of each sub-antenna array, i.e., the antennas on each RAU (organized as a uniform planar array), are obtained by adding the array response to the CIRs derived from the last step. See [6] for more explanations which also verifies the effectiveness of this approach. Finally, the
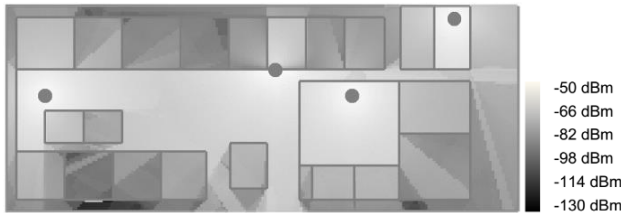
Fig. 2 Simulation scenario with an example of four RAUs deployed at optimized positions, the dots in the figure. The color map shows the received signal strength when assuming 0 dBm transmission power at each RAU.

channel transfer functions on the subcarrier are derived by applying Fast Fourier Transform (FFT) on the CIRs of all antennas.

The selected scenario is a floor of the Electrical Engineering (Flux) building of Eindhoven University of Technology where most of the rooms are for lectures and laboratories, of dimension 100 m × 40 m × 4 m, which is illustrated in Fig. 2. The main objects considered in the ray-tracing simulations are the walls, floor and ceiling. The walls are plastered, and ceilings and floors are concrete, typical materials of large surfaces of office buildings.

B. Ideal Channel Model

The wireless channel model is, as usual, divided into large scale fading and small scale fading. Here the small scale fading across the antennas at an RAU for an STA is described by the i.i.d. Rayleigh fading model. I.i.d. Rayleigh fading model represents the physical environments that are rich in scatters, which somehow results in the ideal channel condition for multi-user spatial multiplexing [3], which results in a capacity upper bound. To be consistent with ray-tracing channel simulation, we have to force the receive signal power between any pair of STA and RAU at the subcarriers to be the same. Therefore, we derive the the the ideal channel through the following procedure.

First, we denote the average channel gain between the mth RAU and the kth STA from ray-tracing channel simulation by β_{mk}, which is obtained by the following normalization

$$\beta_{mk}^{\mathrm{RT}} = \frac{\sum_{l=1}^{L} \| \mathbf{g}_{mk}^{\mathrm{RT}}[l] \|_{\mathrm{F}}^{2}}{NL} \tag{12}$$

where $\| \cdot \|_{\mathrm{F}}$ is Frobenius norm. $\mathbf{g}_{mk}^{\mathrm{RT}}[l]$ is the channel vector on the lth subcarrier, and $l=1,\cdots,L$ (RT is short for ray-tracing). As a result, the small scale fading $\mathbf{h}_{mk}^{\mathrm{RT}}[l] = \mathbf{g}_{mk}^{\mathrm{RT}}[l] / \beta_{mk}^{\mathrm{RT}}$ will have unit average power over all the N antennas and L subcarriers. Note that this channel gain is obtained from an instantaneous channel, which is different from the common large scale fading factor derived by long-term average.

Then, we denote the small scale fading of i.i.d. Rayleigh channel as $\mathbf{h}_{mk}^{\mathrm{IID}}[l]$, where the elements follow i.i.d. $\mathcal{CN}(0,1)$. It is then normalized by

$$\overline{\mathbf{h}}_{mk}^{\mathrm{IID}}[l] = \sqrt{\frac{NL}{\sum_{l=1}^{L} \| h_{mk}^{\mathrm{IID}}[l] \|_{\mathrm{F}}^{2}}} \mathbf{h}_{mk}^{\mathrm{IID}}[l] \tag{13}$$

to obtain unit average power over all the antennas and subcarriers.

Finally, the i.i.d. Rayleigh MIMO channel used for analysis is derived by

$$\mathbf{g}_{mk}^{\mathrm{IID}}[l] = \beta_{mk}^{\mathrm{RT}} \overline{\mathbf{h}}_{mk}^{\mathrm{IID}}[l] \tag{14}$$

As a result, the ray-tracing channel $\mathbf{g}_{mk}^{\mathrm{RT}}[l]$ and i.i.d. Rayleigh channel $\mathbf{g}_{mk}^{\mathrm{IID}}[l]$ will give the same receive power over all subcarriers provided the same total transmission power. The reader can refer to [4] for more details about channel normalization techniques.

IV. NUMERICAL RESULTS

This section presents the numerical results based on the above models to analyze the influences of different parameters on the sum-rate. We consider the antenna system architectures, the precoding techniques and the physical channels. We try to seek insights for the following questions: (1) how many antennas are needed to support a certain number of STAs (2) how differently does large MIMO behave under practical and ideal channel conditions (3) what is the performance difference between CAS and DAS architectures (4) how do the precoding techniques perform. These questions are interesting for practical implementations.

The common simulation parameters are given in Table I.

TABLE I SIMULATION PARAMETERS

Frequency	2.4 GHz
Bandwidth	20 MHz
Number of subcarriers	64
Background noise	-174 dBm/Hz
Noise figure	10 dB
Transmission power	P_0=20 dBm (equal allocation to subcarriers)
Scenario	100 m×40 m× 4 m (STAs at 1 m height)

A. Capacity Versus Number of AP Antennas

We first analyze the influence of the antenna array sizes on the system performance. We consider the CAS architecture (i.e., M=1), and a DAS with M=4, and K=16. For the CAS, the average SNR is around 25dB, thus ensure most STAs are in high-SNR regime. The results are given in Fig. 3. (In all the figures, RT is short for ray-tracing, and IID for i.i.d. Rayleigh channel). The observations are summarized in the following.

The average IF capacity is stable due to the power assumption given in Section II. On the contrary, DPC, ZF and MBF all experience dramatic improvements when MN increases. The average capacity of the DAS is higher due to stronger received signal strength.

DPC, ZF, and MBF, provide data rates below IF case but tend to approach it as MN becomes larger. For example, for CAS in i.i.d. Rayleigh channel, DPC and ZF tightly approximate IF when $MN \geq 128$, i.e., around 8 times of K. The gaps are actually larger in ray-tracing channels. So, in order to achieve a similar data rate as in i.i.d. channels, many more antennas are needed.

The performance differences among the precoders also gradually vanish as MN increases. The interesting finding is that ZF
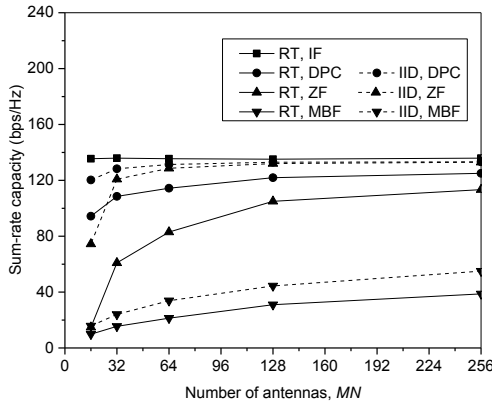
(a) CAS
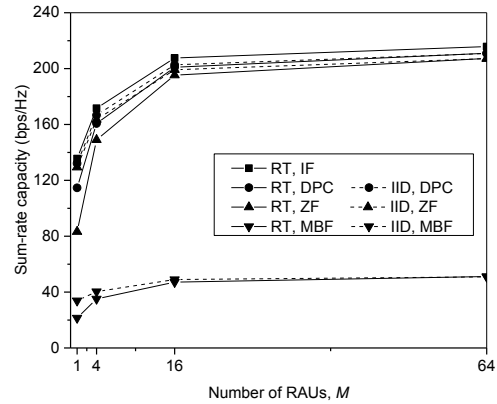
(a) $MN = 64$
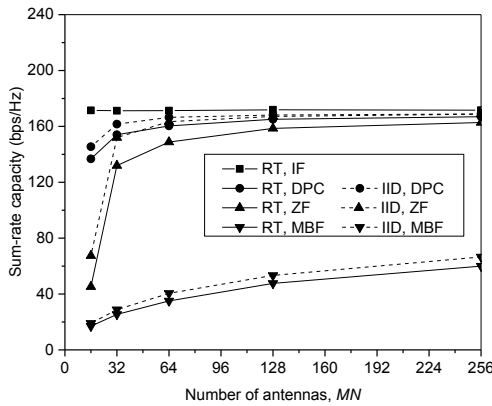
(b) DAS ($M = 4$)
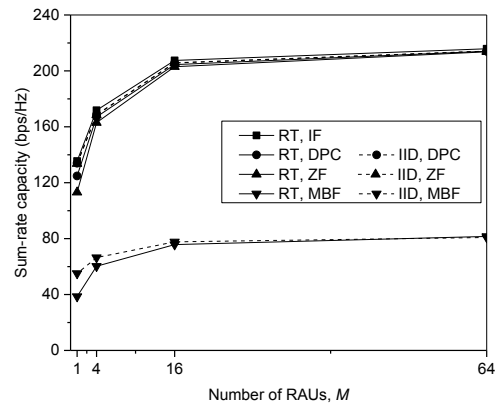
(b) $MN = 256$

Fig. 3 Sum-rates versus total number of antennas with different configurations.

Fig. 4 Sum-rates versus the number of RAUs with the same total number of antennas.

can approximate the performance of DPC for a large MN, which confirms that simple linear precoders can provide close-to-optimum performance. MBF performs much poorer even when MN is very large, although theoretically it is also optimal under condition $MN \rightarrow \infty$. This suggests that precoders considering MUI mitigation should be more effective in practice, especially for the low frequencies, since the required antenna array size is much smaller.

Moreover, the outcome in ray-tracing channel is poorer than in i.i.d. Rayleigh channel. However, the gaps look smaller in DAS when we compare Fig. 3a and Fig. 3b. We further discuss this in the next subsection about the effect of antenna distributions.

B. Capacity Versus Antenna Distribution

Now we consider using the same number of antennas in total (i.e., MN is constant), to investigate the performance changes with different levels of antenna distribution. Specifically, different numbers of RAUs, M, are considered with optimized placement as we mentioned earlier. The other parameters are held the same. The number of STAs is $K = 16$. Fig. 4 shows the results

for MN=64 and 256, respectively.

It can be seen from the figures that a higher distribution level benefits the network from several perspectives. First, the overall sum-rates are increased. Second, the differences of linear precoders in comparison with DPC and IF are decreased. Third, the sum-rate gaps between ray-tracing channel and the ideal i.i.d. channel are smaller. The overall benefit is a compound effect of the macro- and the micro-diversity offered by DAS, which suggests great advantages of DAS over CAS.

Another point is that, the improvements saturate as M increases. From the results, we see that M=16 is already a satisfactory level. This is interesting for practice since it is not necessary to make all antennas distributed over the coverage area to get the best performance, while a small M can offer significant gains.

C. Capacity Versus Number of Co-scheduled STAs

Traditionally, the number of STAs K that can be supported simultaneously depends on the number of antennas at the AP. So, for large MIMO systems, the potential number of co-scheduled STAs is also large. However, as it is known that, to obtain

low-level MUI, user scheduling and complex precoding are needed. The desirable strategy in large MIMO is to employ a much larger number of antennas than parallel spatial streams, in another word, let $MN \gg K$ [1]. As a result, low-complexity precoding can be used to get good performance. It is then interesting to know how large the ratio of MN/K should be. It has been reported in, e.g., [1], that the number of base station antennas should be at least 10 times the number of single-antenna STAs in CAS. The above analysis in this paper also supports this conclusion. However, for a DAS architecture, the statement does not hold. What we show later is that the total number of antennas needed in DAS is actually significantly less.

For the analysis in this subsection, we assume $MN=256$, and, $M=1$ (CAS) and $M=16$ (DAS). We vary K, to see how the sum-rate capacity changes. The other parameters are kept the same. The results are given in Fig. 5.

We can see that rather different results are obtained for CAS and DAS. Many more STAs can be supported in DAS than in CAS to approximately achieve the optimum IF capacity. The superiority is especially significant in the practical ray-tracing channels. For example, even when $K=64$, the STAs can still achieve close-to-optimum performance in DAS, which is not the case in CAS.

One major reason for the poor performance of CAS for large K is due to the compact antenna array which results in correlated channels when STAs are in line-of-sight condition and a poor-scattering channel is experienced. We can see that in i.i.d. Rayleigh channel, CAS still performs well but it is poor in ray-tracing channels. On the contrary, for DAS, the performance tends to be similar as in i.i.d. channels.

Some additional points are necessary to mention. We note that, the targeted K in a practical system may depend on other factors. For example, channel training overheads and the number of pilot sequences may limit K to a smaller number. For that reason, the CAS architecture may be sufficient to get the target performance as well. In addition, other considerations like the antenna array structure (e.g., cylinder array) and user scheduling, should be helpful for improving the performance. This is however out of the scope of this paper. So, the two architectures are equivalent for certain cases. The difference is that, to achieve the same performance, a CAS requires a sufficiently large antenna array, which turns into a large physical size which could lead to practical problems, e.g., form factor and installation issues. A DAS, on the other hand, needs fewer antennas, but requires a more sophisticated infrastructure to support antenna distributions, leading to higher installation cost. Indeed, the DAS architecture in particular with a higher distribution level, surpasses CAS significantly in terms of MU-MIMO capacity.

V. Conclusions and Future Work

This paper analyzes the behavior of MU-MIMO with large antenna arrays in indoor WLAN, operating in the 2.4 GHz ISM band. We have considered the important factors related to the sum-rate performance, including precoding techniques, channel characteristics, and especially antenna configuration and deployment.
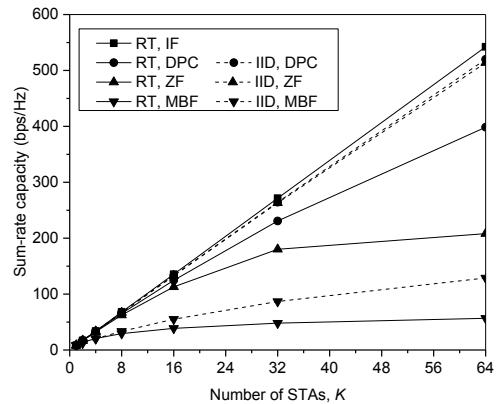
(a) CAS
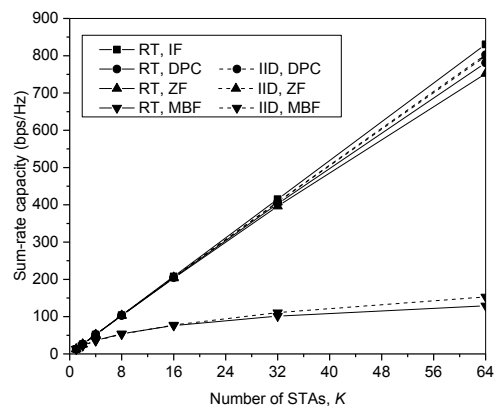
(b) DAS ($M = 16$)

Fig. 5 Sum-rates versus the number of co-scheduled STAs in CAS and DAS.

Although theoretically the upper bound capacity can be achieved by simple linear precoders as the number of antennas $MN \to \infty$, their performance differences are significant when MN is not infinite but assumes practical values, e.g., in the order of hundreds. Regarding precoding, ZF offers much better performance than MBF. This suggests MUI suppression is necessary in the precoding process, which should be considered for designing precoding techniques.

We also found that the DAS architecture significantly surpasses CAS in terms of capacity provisioning to a larger number of co-scheduled STAs. We can interpret that from several aspects. First, less antennas are needed with a DAS architecture, which is preferable in practice in terms of cost and complexity. Second, a higher antenna distribution level leads to better performance, but in fact a moderate level is satisfactory. For example, a balancing point in our analysis is $M = 16$, which results in an inter-RAU distance of around 16 m. Third, DAS is especially superior to CAS in practical channels due to the limited scattering and LOS conditions. This also means that in outdoor channels where the scattering is usually poorer than in indoor, DAS should provide a higher performance gain.

There are several important points we did not address and require further investigation. First, the effect of non-uniform user distributions, e.g., users are clustered at some locations. Second, one needs to consider multiple-AP cases, especially when inter-cell interference may exist due to the higher frequency reuse factor. This requires more sophisticated simulation of the wireless channels, and media access mechanisms. Third, one should take into account per antenna peak or average power constraints, or constant envelop transmission. Especially constant envelop transmission is currently a hot research topic for large MIMO systems [15]. Fourth, the backhaul-related issues for DAS may play a role, e.g., the optical fiber distortion needs to be considered.

REFERENCES

[1] F. Rusek, D. Persson, B. K. Lau, E. G. Larsson, T. L. Marzetta, O. Edfors, and F. Tufvesson, "Scaling up MIMO : Opportunities and challenges with very large arrays," *IEEE Signal Processing Magazine*, vol. 30, no. 1, pp. 40–60, Jan. 2013.

[2] E. G. Larsson, O. Edfors, F. Tufvesson, and T. L. Marzetta, "Massive MIMO for next generation wireless systems," *IEEE Communications Magazine*, vol. 52, no. 2, pp. 186–195, Apr. 2014.

[3] J. Hoydis, C. Hoek, T. Wild, and S. ten Brink, "Channel measurements for large antenna arrays," in *2012 International Symposium on Wireless Communication Systems (ISWCS)*, 2012, pp. 811–815.

[4] X. Gao, O. Edfors, F. Rusek, and F. Tufvesson, "Massive MIMO in real propagation environments," *arXiv preprint arXiv:1403.3376*, pp. 1–10, 2014.

[5] K. T. Truong and R. W. Heath, "The viability of distributed antennas for massive MIMO systems," in *Asilomar Conference on Signals, Systems and Computers*, 2013, pp. 1318–1323.

[6] J. Weng, X. Tu, Z. Lai, S. Salous, and J. Zhang, "Indoor massive MIMO channel modelling using ray-launching simulation," *International Journal of Antennas and Propagation*, vol. 2014, pp. 1–13, 2014.

[7] T. Koonen, "Fibre to the home/fibre to the premises: what, where, and when?," *Proceedings of the IEEE*, vol. 94, pp. 911–934, 2006.

[8] R. W. Heath, T. Wu, Y. H. Kwon, and A. C. K. Soong, "Multiuser MIMO in distributed antenna systems with out-of-cell interference," *IEEE Transactions on Signal Processing*, vol. 59, no. 10, pp. 4885–4899, 2011.

[9] K. Hosseini, W. Yu, and R. Adve, "Large-scale MIMO versus network MIMO for multicell interference mitigation," *IEEE Journal of Selected Topics in Signal Processing*, vol. 8, no. 5, pp. 930 – 941, 2014.

[10] A. Hekkala, M. Hiivala, M. Lasanen, J. Perttu, L. C. Vieira, N. J. Gomes, and A. Nkansah, "Predistortion of radio over fiber links: Algorithms, implementation, and measurements," *IEEE Transactions on Circuits and Systems*, vol. 59, no. 3, pp. 664–672, 2012.

[11] J. Lee and N. Jindal, "High SNR Analysis for MIMO Broadcast Channels: Dirty Paper Coding vs. Linear Precoding," *IEEE Transactions on Information Theory*, no. 2, p. 33, 2006.

[12] Q. Wang, Z. Cao, D. DebBarma, I. Niemegeers, S. Heemstra de Groot, and A. Lo, "Measurements and performance of large MIMO systems at 2.4 GHz for indoor WLAN," in *2014 IEEE 21st Symposium on Communications and Vehicular Technology in the Benelux (SCVT)*, 2014, pp. 35–40.

[13] J. Deissner, J. Hubner, D. Hunold, and J. Voigt, *RPS Radiowave Propagation Simulator*. Actix GmbH, 2008.

[14] E. Amaldi, A. Capone, M. Cesana, F. Malucelli, and F. Palazzo, "WLAN coverage planning: optimization models and algorithms," *2004 IEEE 59th Vehicular Technology Conference*, vol. 4, pp. 2219 – 2223, 2004.

[15] S. K. Mohammed and E. G. Larsson, "Per-antenna constant envelope precoding for large multi-user MIMO systems," *IEEE Transactions on Communications*, vol. 61, no. 3, pp. 1059–1071, 2013.

Qing Wang received his B.Eng. degree in Telecommunication Engineering from Xidian University, China, in 2009. In 2011, he obtained his M.E. degree in Information and Communication Engineering from National University of Defense Technology, China. He is currently working towards his Ph.D. degree in COBRA Research Institute at Eindhoven University of Technology, The Netherlands. His research interests include wireless and mobile communications, wireless indoor networks, WLAN and radio-over-fiber technologies.

Diptanil DebBarma was born in Agartala, India in 1986. He received his B.E from Sathyabama University, India in Electronics and Telecommunication in 2004 and graduated as one of the University Topper. He obtained his Masters (M.E) from the prestigious Indian Institute of Science (IISc), India in Telecommunication, 2010, and was the recipient of the Ministry of Human Resource and Development (MHRD) scholarship. Currently he is pursuing his PhD at Eindhoven University of Technology (ECO group) working for the Dutch IOP-GenCom project MEANS. His research interest includes Wireless Communication, Wireless Network, Stochastic Network Control, Network Coding implementation in wireless MAC, Information Theory, MU-MIMO, Cooperative and Distributed MIMO.
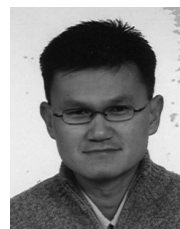
Anthony Lo received combined B.S. and B.E., and Ph.D. degrees in 1992 and 1996 from La Trobe University, Australia. He is currently a Principal Scientist at Huawei Technologies R & D Sweden. He was an assistant professor at Delft University of Technology and, prior to the academic appointment, he was a research engineer at Ericsson EuroLab working on UMTS/HSPA and LTE. His research interests include M2M Massive MIMO, communications, intelligent transportation systems, smart grids, and the wireless network cloud.

Ignas Niemegeers got an MSc degree in Electrical Engineering from the University of Gent, Belgium in 1970, an MSc in 1972 and a PhD degree in 1978 in Computer Engineering from Purdue University, USA. From 1978 to 1981 he was a system designer at Bell Telephone Mfg. Cy, Antwerp, Belgium. From 1981 to 2002 he was professor at the University of Twente, The Netherlands. From 1995 to 2002 he was Scientific Director of the Centre for Telematics and Information Technology (CTIT) of the University of Twente. From 2002 until 2012 he was chairman of the Telecommunications Department and professor in Wireless and 8 Mobile Communications at Delft University of Technology. Since August 2012 he is emeritus professor at Delft University of Technology

and advisor to the Centre for Wireless Technology at Eindhoven University of Technology, The Netherlands. He was involved in many European research projects and reviewer for many projects. His present research interests are 5G, Radio-over-fiber networks, 60 GHz networking, energy-harvesting networks.

Sonia Heemstra de Groot holds M.Sc. degrees in Electrical Engineering from Universidad Nacional de Mar del Plata, Argentina and Philips International Insti-tute/NUFFIC, The Netherlands. She obtained the Ph.D. degree in Electrical Engineering at the University of Twente, The Netherlands, in 1990. Since 2012 she is a full professor at Eindhoven University of Technology where she holds the part-time chair in Heterogeneous Network Architectures. Before she has had assistant and associate professor positions at the University of Twente and a full-professor position at the Delft University of Technology in Personal and Ambient Networking. After having worked some years as a senior researcher at Ericsson EuroLab, The Netherlands, she co-founded the Twente Institute for Wireless and Mobile where she has been Chief Scientist from 2003 to 2014. Her expertise and interests are in the areas of wireless and mobile communications, wireless networks, Internet of Things, wireless security, personal and ambient networks (co-inventor of the concept of personal networks and federations concept), vehicular networks, wireless indoor communications, and radio-based positioning techniques. She has coordinated and participated in many national and international research projects and has authored or co-authored more than 150 papers published in international journals or presented at international conferences.

CALL FOR PAPERS
Special Issue on Applied Cryptography and Security

This special issue will focus on the area of applied cryptography and security, in particular on the following topics:
- **Applied Cryptography,**
- **Practical Cryptanalysis,**
- **Cryptographic Protocols,**
- **Security Mechanisms Deploying Cryptography.**

The Special Issue will accommodate journal versions of selected papers from SantaCrypt 2015, a Czech and Slovak workshop to be held in Prague, Czech Republic, on December 3-4, 2015. In addition, papers from open call are welcome.

Deadlines:

Submission of manuscripts: November 15, 2015.

Notification of authors about the evaluation: December 15, 2015.

Submission of camera ready versions of accepted papers: January 10, 2016.

Guest Editors:

VÁCLAV (VASHEK) MATYÁŠ is a Professor at the Masaryk University, Brno, CZ, and Vice-Dean for Foreign Affairs and External Relations, Faculty of Informatics. His research interests relate to applied cryptography and security, where he published over 150 peer-reviewed papers and articles, and co-authored several books. He was a Fulbright-Masaryk Visiting Scholar with Harvard University, Center for Research on Computation and Society in 2011-12, and previously he worked also with Microsoft Research Cambridge, University College Dublin, Ubilab at UBS AG, and was a Royal Society Postdoctoral Fellow with the Cambridge University Computer Lab. Vashek edited the Computer and Communications Security Reviews, and worked on the development of Common Criteria and with ISO/IEC JTC1 SC27. He received his PhD degree from Masaryk University, Brno and can be contacted at matyas AT fi.muni.cz.

ZDENĚK ŘÍHA is an Assistant Professor at the Masaryk University, Faculty of Informatics, in Brno, Czech Republic. He received his PhD degree from the Faculty of Informatics, Masaryk University. In 1999 he spent 6 months on an internship at Ubilab, the research lab of the bank UBS, focusing on security and usability aspects of biometric authentication systems. Between 2005 and 2008 he was seconded as a Detached National Expert to the European Commission's Joint Research Centre in Italy, where he worked on various projects related to privacy protection and electronic passports. He was involved in the ePassport interoperability group known as the Brussels Interoperability Group. Zdeněk has been working with the WG 5 (Identity management and privacy technologies) of ISO/IEC JTC 1/SC 27. Zdeněk's research interests include Android security, smartcard security, PKI, security of biometric systems and machine readable travel documents. Zdeněk can be contacted at zriha AT fi.muni.cz.

PAVOL ZAJAC is an Assistant Professor at the Slovak University of Technology in Bratislava, Faculty of Electrical Engineering and Information Technology, Slovakia (FEI STU). He received his PhD degree in Applied Mathematics from FEI STU. His main research focus is in the area of mathematical cryptology, including mathematical principles of cipher design, and algebraic cryptanalysis. He also works on various application projects, including efficient implementation of post-quantum cryptosystems, and improving privacy of user data on mobile devices. Pavol can be contacted at pavol.zajac AT stuba.sk.

Dynamic Queue Utilization Based MAC
for Multi-Hop Ad Hoc Networks

Jims Marchang[1], Bogdan Ghita[1], and David Lancaster[1]

Abstract – **The end-to-end throughput in single flow multi-hop Ad Hoc networks decays rapidly with path length. Along the path, the success rate of delivering packets towards the destination decreases due to higher contention, interference, limited buffer size and limited shared bandwidth constraints. In such environments the queues fill up faster in nodes closer to the source than in the nodes nearer the destination. In order to reduce buffer overflow and improve throughput for a saturated network, this paper introduces a new MAC protocol named Dynamic Queue Utilization Based Medium Access Control (DQUB-MAC). The protocol aims to prioritise access to the channel for queues with higher utilization and helps in achieving higher throughput by rapidly draining packets towards the destination. The proposed MAC enhances the performance of an end-to-end data flow by up to 30% for a six hop transmission in a chain topology and is demonstrated to remain competitive for other network topologies and for a variety of packet sizes.**

Index Terms – **Ad-Hoc, MAC, Queue, QoS, Network Saturation.**

I. INTRODUCTION

Quality of Service (QoS) provisioning in Ad Hoc networks remains a challenging issue despite substantial research undertaken over the past decade [1]-[5]. Seminal papers have considered the capacity of a wireless network subject to multiple flows [6] but in this paper attention is restricted to a single multi-hop flow in the saturated region (a point where increasing the input data rates in the network does not enhance the performance further). Even in this case, due to high interference and limited bandwidth, network environments self-generate bottlenecks along multi-hop paths. The network saturates rapidly and end-to-end throughput decays rapidly with path length [7]-[8].

For a single multi-hop flow in an Ad Hoc wireless network, a node is considered to be active if it is a source node, a relay node, or a receiving node. In standard IEEE 802.11DCF, all active nodes have equal probability of accessing the medium, and a node with i active nodes in its interference range may gain access to the medium with a probability of $1/i$. In a linear chain topology, per node

access probability decreases as the hop count rises and the interfering nodes increases. For a long chain topology, the highest degree of interference occurs around the centre of the chain and is lower towards either the source or the destination ends of the chain. So, for a single flow along a chain, the queue utilization pattern will vary with the hop count. This motivates the design of a medium access mechanism that dynamically depends on the queue utilization of the participating nodes.
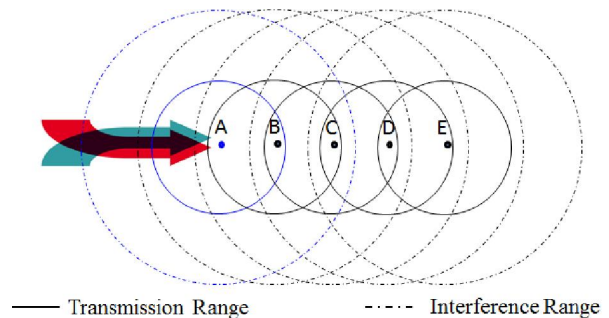
Figure 1. A chain topology with four hop network

In the given figure 1, if node A wants to send data to node E, as the number of hop increases, the degree of interference and the number of contenders also increases, so it gets harder to push the packets forward towards the destination. When node A uses the channel, node B and C has to differ, because node B is with the transmission range of node A and node C is within an interference range of node A. In such a distributed network with a shared channel mechanism, if a real time traffic with a high data rate of constant bit rate is generated at node A or node A acts as a gateway of the inflow traffics, the chances of buffer overflow is high since the access of the shared channel by node B or C would force node A to differ accessing the channel. Thus a ripple effect of differing upto two hop neighbours is formed when a node becomes active as a sender or as a relay node in a shared channel of multi hop network. So, achieving high end to end throughput is limited by the nature of the network.

In the condition of network saturation, losses of data in the network are mainly due to the queue being full, no route availability or retry count exceeded. Other kinds of drops are due to collision and packet error, but such packets are retransmitted if the TTL (Time To Live) and retry count are still valid. Problems induced by physical limitations like

bandwidth, transmission range and interference range cannot be resolved easily, but the MAC algorithm can be adjusted to control the access mechanism in such a way that overall packet drop is reduced and the network performance is elevated, which is the aim of this paper.

II. PERFORMANCE OPTIMIZATION IN AD HOC NETWORKS

In order to improve the performance of resource constrained Ad Hoc networks, a number of protocols have been proposed by different authors: challenges and prospects of bandwidth allocation are discussed in [9] and a method of predicting the available bandwidth for optimizing per node performance is proposed in [10].

Significant efforts have focused on optimizing the performance in multi-hop wireless Ad Hoc networks by controlling congestion and by designing efficient MAC protocols. The IEEE 802.11DCF specification provides fairness across the active contending nodes within its transmission range [11], but in order to differentiate services both in terms of throughput and delay and provide QoS, IEEE 802.11e was introduced with some variations in [12]-[14]. In order to enhance the performance of IEEE 802.11e, [15] discusses a technique to avoid unnecessary polling of a silent station which generates voice traffic. In order to elevate the end-to-end throughput, hop-by-hop congestion control is discussed in [16] and an end-to-end congestion control is also proposed in [17]. The authors of [18] describe a throughput-oriented MAC by controlling the transmitting power of the nodes based on game theory, to achieve concurrent transmission, [19] describes a method to optimize the sensing thresholds of the CSMA receiver and the transmitter by minimizing the outage probability by using SINR (Signal to Noise Ratio). A distributed contention window adaptation technique to adjust the incoming and the outgoing traffic is proposed in [20]. The authors of [21] describe an interesting MAC protocol that allows a concurrent transmission among the neighbours. In order to optimize the contention window usage, the authors of [22] also proposed a backoff generator based on contention level and the channel BER (Bit Error Rate) status.

The remainder of the paper is structured as follows. The proposed MAC is described in detail in Section III. Section IV provides the evaluation of the results, and then Section V concludes the paper by proposing a number of future directions.

III. PROPOSED MAC

A. Proposed Exponential Backoff Mechanism
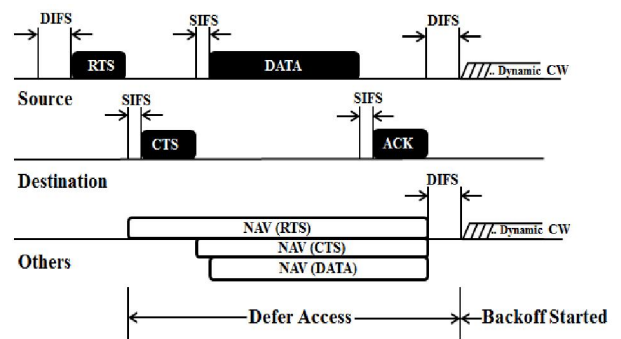
Figure 2 : Medium Access Control Operation.

The proposed MAC, named Dynamic Queue Utilization Based MAC (DQUB-MAC), is derived from the original IEEE 802.11 specification and operates within the context of the RTS/CTS mechanism shown in figure 2. The new protocol dynamically adjusts the probability of accessing the medium according to the buffer utilisation of active nodes. It does this by varying the [CWMin; CWMax] interval used in the backoff phase of the IEEE 802.11 protocol. As such, this protocol is explicitly cross-layer and the information concerning the queue utilization (q_u) is passed to the MAC layer with the help of a new 16-bit field in the IP packet header as shown in figure 3. Although not used in this paper, this information embedded in the packet header could also be useful at the next hop as it makes the node aware of the buffer status of the preceding node.
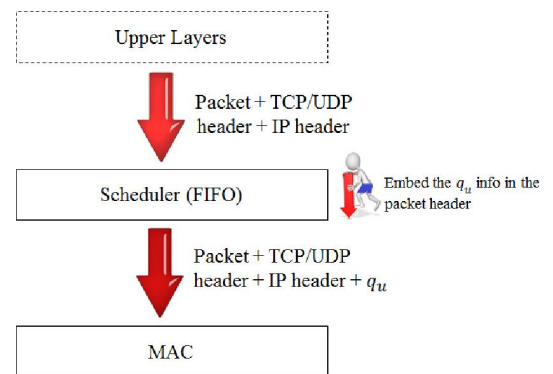
Figure 3: Embedding the Queue Utilization info in the Packet.

The DQUB-MAC assigns higher medium access probability to nodes with a higher queue utilisation. A node with full or already overflowing queue has the greatest likelihood of accessing the medium and a node with an almost empty queue has low probability of accessing the channel. This differentiation increases the probability of frames progressing to the next hop should that node have an emptier queue. This optimizes the utilization of the queues and reduces the packet drop along the path and leads to higher end-to-end network throughput.

A node running the DQUB-MAC protocol is initialised in the usual way with [*CWMin;CWMax*] =[0:8]. When the node becomes active either in sending, receiving or

relaying, the CW range depends linearly on the remaining space in the queue according to (1).

$[CWMin, CWMax]$

$$= \begin{cases} \left[2^{\alpha}\frac{Q-q_u}{\psi}; 2^{\alpha}(\frac{Q-q_u}{\psi}+1)\right], & r = 0 \\ \left[2^{\alpha}\left(\frac{Q-q_u}{\psi}+1\right)(\gamma); 2^{\alpha}\left(\frac{Q-q_u}{\psi}+2\right)(\gamma)\right], & r > 0 \end{cases}$$

(1)

In (1), Q denotes the maximum size of the queue, and the current utilization of the queue is denoted by q_u, so $Q - q_u$ represents the remaining number of empty slots of the queue. There are two adjusting parameters, α and ψ; and they control the width of the range of the contention window and the number of the priority levels respectively. In the present work, Q =100 and the adjusting parameters are set to α= 3, so that the contention window range grows/shrinks with a factor of 8 for different priority levels and with ψ= 30 in (1) to generate four different priority levels, namely: low, fair, high and very high when the queue utilization is between 0-29%, 30-59%, 60-89% and >=90% respectively. So, a fuller queue has a higher probability to access the channel compared to the emptier queue. The retry count of a packet is denoted by r and when the data packet is to be retransmitted ($r>0$) then a new contention window (CW) range interval is calculated as shown in (1). This depends linearly on the remaining number of retries given by γ, which is computed as the difference between the retry limit of retransmission, and the current retry number of retransmission. This factor γ helps a packet which has attempted a higher number of retransmission to get higher degree of access probability to that of a fresher one when the queue utilizations (q_u) of the nodes are similar. The maximum number of retransmissions takes the same value as used in IEEE802.11 following the work of [23], so that packets which are too old are discarded after several unsuccessful attempts.

IV. EVALUATION

The new algorithm has been tested and benchmarked against both IEEE802.11 and IEEE802.11e standards in a variety of simulation environments. The purpose of the tests is to evaluate the efficiency in distributing the traffic and queue utilisation, as well as to determine the resulting packet loss in saturated network scenarios. Moreover, some tests of the robustness of the algorithm under less favourable circumstances are also performed.

All simulations are carried out with NS2, version 2.35 according to the network parameters listed in Table 1. Each simulation lasts for 800 seconds and each result is an average value of 10 rounds of simulations. The majority of simulations are performed using 1000 byte packet size.

A. Six-hop chain topology:

Most of the simulations use a regular chain topology based on the node arrangement shown in figure 4 and later a rigorous random topology simulations are considered to validate the testing. Different length chains will be considered but the first sets of simulations are based on a six hop chain. Node 0 and node 6 act as the source and the destination respectively for a UDP connection supporting a CBR application with a packet size of 1000 bytes.

Parameter	Value/protocol used
Grid Size	2000m x 2000m
Routing Protocol	DSDV
Queue Type	DropTail
Queue Size	100
Bandwidth	2Mbps
SIFS	10μs
DIFS	50μs
Length of Slot	20μs
Transmission Range	250m
CS Range	550m
Max$_{Retry}$	7
Simulation Time	800s
Traffic Type	CBR
Packet size	500, 1000, 1500 bytes

Table 1: Simulation Setup.
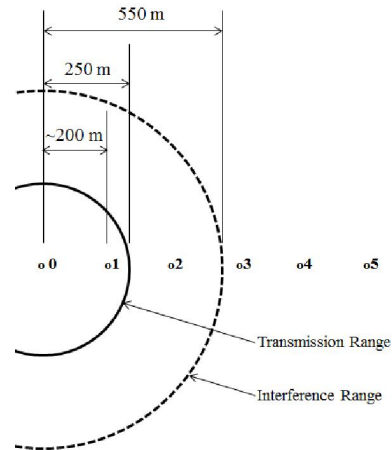
Figure 4: Chain Topology settings of the Ad Hoc Network

The first set of simulations measure the throughput as the offered load is increased on the 6-hop chain. Figures 5, 6, and 7 show the results for IEEE802.11 DCF, IEEE802.11e and DQUB-MAC respectively.

In the experiment of figure 5, using IEEE 802.11 DCF the MAC layer contention among the competing nodes is fair, but interference along the transiting path is different, and the incoming and the outgoing packets of an active node are not controlled. Consequently it is expected that the

packet drop and queue utilization will not be uniform along the path. Figure 5 shows that end-to-end throughput starts to saturate when the source node generates data at approximately 290kb/s in IEEE802.11DCF. The performance deteriorates as the offered load increases, but stabilizes at around 400kb/s and upwards. The graph also shows the data rates in each node in order to display the bottlenecks. The graph confirms that loss of packets along the route is not uniform and neither is the utilization of each queue along the path. The end-to-end throughput at the point the network becomes saturated is approximately 200kb/s.
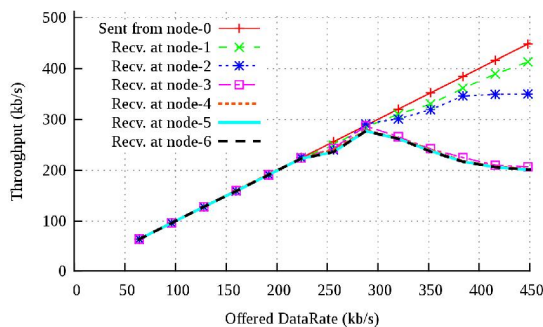
Figure 5: Throughput per Hop Vs Offered DataRate, IEEE802.11DCF on a 6-hop Chain.

Figure 6 shows that the performance of IEEE 802.11e is worse than IEEE 802.11DCF despite setting the data flow to the highest priority. This is due to the fact that the CW window range for this highest priority is only (7,15) which is too narrow for a saturated network. The end-to-end throughput starts to saturate only at around 200kb/s, a traffic load much lower to that of IEEE802.11DCF. Since, the network becomes saturated much earlier, the experiment reveals that there is a heavy loss of packets in an around the source node. This result also shows that the distribution of the queue utilization is non-uniform along the high hop communicating path. The end-to-end throughput after network saturation is approximately 130kb/s, a value which is approximately 35% lower than IEEE 802.11DCF.
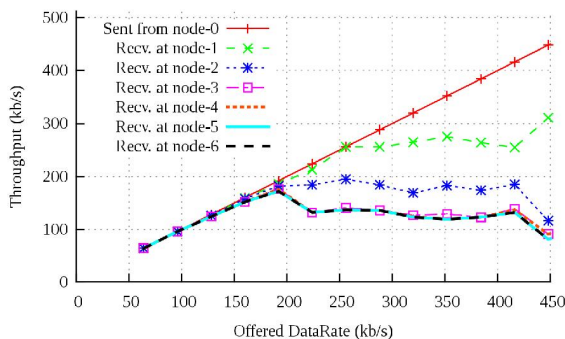

Figure 6: Throughput per Hop Vs Offered DataRate, IEEE802.11e on a 6-hop Chain.

The experiment of figure 7 shows that the saturation point of the offered load of DQUB-MAC is similar to that

of IEEE 802.11DCF protocol. However, as the offered load is further increased, the performance does not sink like IEEE 802.11DCF and IEEE802.11e. Instead, as the queue utilization along the path is distributed more uniformly in comparison with IEEE 802.11DCF or IEEE 802.11e, the resulting data rates continue to increase when the offered data rate increases. This is due to the fact that the nodes with heavily utilized queues are given higher probability to access the channel than the ones that are less utilized. As a queue fills up, more packets are forwarded towards the nodes with underutilised queues. Those nodes with similar queue utilization are hereby each share the same CW range. Nodes with fewer packets wait longer than the ones that are overflowing, therefore the overall packet drop is greatly reduced and in turn the network performance is enhanced. The network becomes saturated with a high end-to-end throughput of approximately 270kb/s. The end-to-end throughput of DQUB-MAC is approximately 35% and 107% higher than that of IEEE802.11DCF and IEEE802.11e respectively in network saturation.
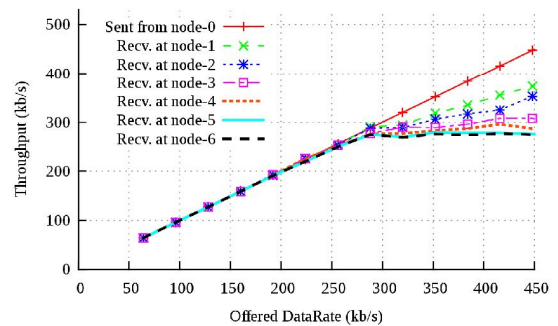
Figure 7: Throughput per Hop Vs Offered DataRate, DQUB-MAC on a 6-hop Chain.

Figure 8 shows the throughput achieved per hop along with the error bar for a specific offered data rate of 416kb/s along the 6-hop chain. This represents the packet arrival rate at each intermediate node. In the case of IEEE 802.11DCF, the data rate is halved after three hops; IEEE 802.11e halves the data rate after only two hops from the source. In the case of DQUB-MAC, the overall arrival rate at each intermediate node is much higher than for the IEEE802.11 standards and the data rate never drops by half. This improvement is due to the fact that queues that are either full or highly utilised (in this case queues on the source and the following few nodes) will dynamically receive higher access probability to push the packets forward, compared to those nodes whose queues are less populated and are situated closer towards the destination. Since no priority of any form is assigned to IEEE 802.11 DCF, the impact of hidden nodes and buffer overflow degrades the performance of the network after third hop and similar is the case for IEEE 802.11e.

The error bar is too small to be visible as shown in the figure 8. During network saturation, the average delay between two successive packet arrivals of a packet size of 1000 bytes at the destination when DQUB-MAC, IEEE

802.11 DCF, and IEEE 802.11e MAC are used are 28.8569ms, 29.3185ms and 60.411ms respectively, when the packet generating interval at the source is 19.2307ms. At a low data rate when packets of 1000 bytes are generated with an interval of 62.5ms at the source i.e. during unsaturated network, the average delay between two successive packet arrivals are 62.5131ms, 62.5046ms, and 64.102ms while using DQUB-MAC, IEEE 802.11 DCF, and IEEE 802.11e MAC respectively. During network saturation, the overall average arrival rate is higher for DQUB-MAC, due to the use of fast forwarding technique when queue utilization is high, unlike IEEE 802.11 DCF or IEEE 802.11e MAC where heavy loss of packets occurs due to buffer overflow.

Figure 8: Avg. Throughput Vs Hops along the Path.

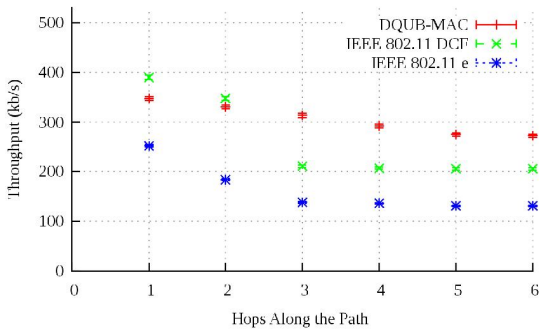The way in which DQUB-MAC improves the queue utilisation distribution is shown in figure 9 which presents the per-hop packet loss distribution with an offered load of 416kb/s. The maximum loss rate at any hop along the route for DQUB-MAC is only 15% whereas IEEE802.11DCF and IEEE802.11e have maximum loss rate approaching 40%. In DQUB-MAC, the loss rate is distributed uniformly along the route while IEEE 802.11DCF and IEEE 802.11e, display an irregular pattern of loss.
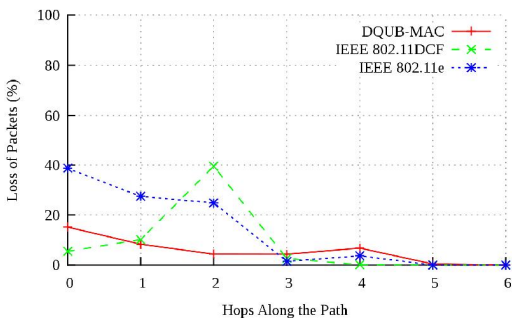

Figure 9: Per-hop Packet Loss Distribution.

B. *End-to-End Delay Analysis:*

Using the chain topology of figure 4 and the network parameters listed in table 1, the average end-to-end delay of a packet with a short path length of 2 hops and a long path length of 6 hops are calculated with an increasing offered

load as shown in table 2. The average end-to-end delay is the average time taken by a packet between its delivery time at the destination and the time when it was generates at the source's application. The main factors contributing to the end-to-end delay of a packet are processing delay, queuing delay and transmission delay; among all these factors, the queuing delay has the highest impact on delaying the end-to-end delivery of a packet. In a shared channel environment, higher number of active nodes led to a higher degree of contention which enhances the queuing delay.

Source Data Rate kb/s	Average End-to-End delay in sec			
	2 hops		6 hops	
	IEEE 802.11 DCF	DQUB-MAC	IEEE 802.11 DCF	DQUB - MAC
32	0.010914	0.011452	0.03315	0.034774
96	0.01091	0.011451	0.033141	0.034775
160	0.01091	0.01145	0.033154	0.034825
224	0.01091	0.01145	0.033153	0.034776
288	0.01091	0.011452	0.191107	0.233461
352	0.01091	0.011451	3.457812	2.939796
416	0.01091	0.011451	4.854712	4.986854
480	0.01091	0.01145	6.025652	5.738954
544	0.010912	0.011452	6.403192	5.85696
608	0.010909	0.011453	6.427407	6.086968
672	0.010897	0.011502	6.294373	6.065397

Table 2: Average End-to-End Delay of a Packet.

Here in analysing the delay, instead of testing with different packet sizes, the end-to-end delay is evaluated using different data rates with a fixed packet size of 1000 bytes, so that the rate of generation of packet varies. For a short distance communication like two hops, the end to end delay is not much affected by the increasing data rate of the source in both the medium access control protocols, IEEE 802.11 DCF and DQUB-MAC when tested with an offered load of upto 672 kb/s. But in case of long path length like 6 hops, where the degree of contention is higher, DQUB-MAC performs better in terms of average end-to-end delay in comparison to IEEE 802.11 DCF when the offered load of the source is high; it is due to the fast forwarding technique used in DQUB-MAC when the queue utilization is higher. When the data rate is low, the end-to-end delay is small because there is sufficient bandwidth to share among the contending nodes and the queue hardly gets full to introduce a long queueing delay, but when the offered data rate is high, more packets are generated with a faster rate at

the source than the capacity of the shared channel, so the queuing delay increases, resulted in higher end-to-end delay in both the IEEE 802.11 DCF or the DQUB-MAC.

C. Shorter chains:

Since the end-to-end performance of IEEE 802.11e is not competitive, comparison of the proposed protocol is done only with IEEE 802.11DCF hereafter. Two-hop and four-hop chain topologies are tested and compared with the outcome scenario of the six-hop chain topology. In order to cause network saturation, the offered data rates are 768kb/s, 585kb/s and 416kb/s respectively.

Table 3 compares the three different scenarios and confirms that the longer the path length, the larger is the performance improvement from using the new algorithm. However, there is a discernible advantage even for short chains. The reason for small improvement for shorter chain in DQUB-MAC is due to similar queue utilization pattern (similar priority) among the nodes, since the nodes are exposed within the vicinity of each other's interference ranges. When the path length is high, the degree of contention and interference density vary, resulted in higher degree of variation in queue utilization pattern, highest around the source.

MAC Type	Chain throughput (kb/s)		
	2-hop	4-hop	6-hop
IEEE 802.11 DCF (A)	715	324	208
DQUB – MAC (B)	726	334	271
Percentage improvement	1.5%	3.1%	30.3%

Table 3: Saturation Throughput of Shorter Chains.
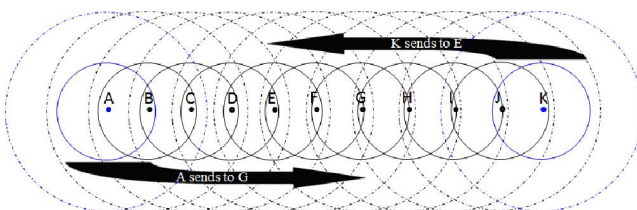
D. Flows with opposite directions:

Figure 10: A chain topology with 11 nodes, with two flows from Opposite Direction.

Here in figure 10, eleven different nodes are arranged in a chain topology. Two sources of the extreme end points of figure 10 are selected as the sources, where node A sends to node G and node K sends to node E, so that the two traffics crosses each other with a crossover of two hops and each flow has to move six hops to reach their respective

destinations. The graph of figure 11 provides the network performance of the network for an increasing data rate of per flow offered load of the network topology of figure 10, which is tested with a network parameters listed in table 1. In a system using IEEE 802.11 DCF medium access control mechanism, the total network throughput peaks when the offered per flow load is 250kb/s to 350kb/s, but thereafter despite increasing the per flow offered load of the network, the total end-to-end network throughput drops drastically and saturates with a total network throughput of around 325kb/s. In case of DQUB-MAC, the network saturates with a higher network throughput of around 375kb/s. It shows that there is a performance gain of 15% during network saturation in case of DQUB-MAC over the standard IEEE 802.11 DCF medium access control protocol. In such case where one traffic flow crosses other traffic flow in an opposite direction with a 6 hop communication, the peak network throughput is achieved when the per flow load supply is between 250kb/s - 350kb/s and 250kb/s - 420kb/s in case of IEEE 802.11 DCF and DQUB-MAC respectively. Increasing per flow load does not increase the overall network performance after the peak, but the DQUB-MAC performs better and handles saturated region more efficiently to that of IEEE 802.11 DCF as shown in figure 11.
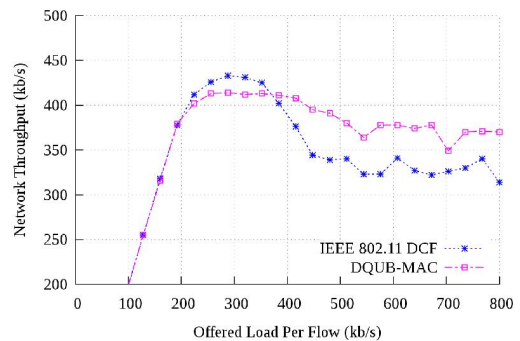
Figure 11: Network performance, with two flows running from opposite direction

E. Other packet sizes:

So far, all simulations have taken place with 1000 byte packets. Under the same network scenarios and the same network parameters, it is observed that for smaller 500 byte packets the performance gain is not as large. This is due to the fact that the control overhead (RTS-CTS-ACK) increases substantially. The gain of DQUB-MAC over IEEE802.11DCF for high hop count is approximately 16%. When the hop count between the communicating nodes is two and four, then the performance gain of DQUB-MAC over IEEE802.11DCF is approximately 2.5% and 3.2% respectively.

For larger packets, beyond the Maximum Transfer Unit (MTU) of a link, the packet is fragmented. However, even with a 1500 byte packet and 1000 byte MTU the

performance gain of DQUB-MAC over IEEE802.11DCF over two hops, four hops and six hops is approximately 5.0%, 12.0% and 18.0% respectively.

F. Random topology:

In order to validate the results are not an artefact of artificially arranged networks, a random placement of 40 nodes is considered as shown in figure 12, by dividing the area into three zones, namely AREA 1, AREA 2 and AREA 3. AREA 1, AREA 2 and AREA 3 are randomly placed with 10 nodes, 20 nodes and 10 nodes respectively. Sources and destinations are also randomly selected from AREA1 and AREA 3 respectively. Potential source zone and destination zone are separated by at least 1000m with a consideration that source and destination are at least multiple hops apart. A fixed data rate of 416kb/s is offered to the network and tested with 1000 byte packets of real time data like CBR traffics. The same network parameters listed in Table 1 are used during the simulation. The actual path taken depends on the routing algorithm, DSDV. Two different sets of simulations are considered: firstly, with a single flow with a random selection of source from AREA 1 and a random selection of destination from AREA 3. Secondly, a case with a multiple flow (two flows in this case) with a random selection of distinct source and destination pairs from AREA 1 and AREA 3 respectively are considered. A total of 200 different random topologies are considered with a fresh random selection of source and a destination pair(s) at each turn in both the cases. Ignore all those simulations, if path could not be established between the source and destination pair.
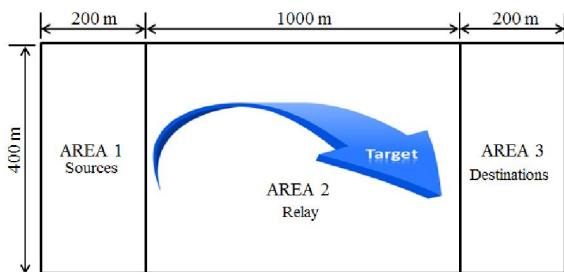

Figure 12: Random Topology

Since the node placement is defined and the simulation is ran extensively, an average value is considered for simplicity in analysis. In the first case with a single flow, the correlation coefficient of the end-to-end performance of IEEE 802.11 DCF and DQUB-MAC is +0.78, showing a strong uphill (positive) linear relationship. In this case DQUB-MAC yields a performance gain of approximately 42kb/s, which is a gain of 22% over IEEE 802.11 DCF. The error bar of IEEE 802.11 DCF is 1.043 and that of DQUB-MAC is 1.127 which shows that both the protocols are consistent and performance does not fluctuate much. In a multiple flow scenarios, the total network performance gain of DQUB-MAC is approximately 37kb/s, which is a gain of

20% over IEEE 802.11 DCF. The average degree of fairness among the flows in DQUB-MAC and IEEE 802.11 DCF are 97.51% and 97.60% respectively, using Jain's fairness index.

The random topology setup of figure 12 is also tested with an exponential traffic generator with multiple sources. During an exponential traffic generation there are different durations called the burst period and the idle time. The burst period is the time when network traffic is generated and idle time is the period when the application goes silent. The system is tested with a network parameters listed in table 1 with a 1000 bytes packet size and a multiple flows of 416kb/s per flow offered load in the network. Table 4 shows that whether the idle time is smaller or greater than the burst time, the overall network performance gain of DQUB-MAC outperformed the standard IEEE 802.11 DCF. When the burst time is greater than or equal to the idle time, the overall network performance gain of DQUB-MAC is over 16% compared to the IEEE 802.11 DCF.

Burst Time (s)	Idle Time (s)	IEEE 802.11 DCF (kb/s)	DQUB-MAC (kb/s)	Gain %
1.0	0.5	193.96	226.66	16.85
0.5	1.0	209.74	218.08	03.97
0.5	0.5	204.84	242.02	18.15

Table 4: Network Performance using Exponential Traffics.

V. CONCLUSION AND FUTURE DIRECTION

This paper has proposed a new MAC protocol, called Dynamic Queue Utilization Based (DQUB) MAC, which adjusts the contention window range based on the current utilization of the queue. As a result, a node with higher utilisation queue will be prioritised over a node whose queue is less utilized. Moreover, during packet retransmission, the protocol also ensures that packets with higher retransmission count will take priority over packets with lower retransmission count.

In simulations using a long 6-hop chain topology, the proposed DQUB-MAC demonstrated a performance gain of up to 30% over IEEE 802.11DCF when a CBR traffic is considered. Despite employing the highest priority, IEEE 802.11e performs even worse than IEEE 802.11DCF. Additional experiments also showed that these performance gains are robust with respect to varying the length of the chain, adjusting the packet size, considering random topologies and DQUB-MAC also works well with exponential traffic applications with a performance gain of over 16% when a burst time is greater than or equal to the idle time. There is a high degree of stability and consistency in DQUB-MAC even with random topologies. The degree of fairness of DQUB-MAC is equally compatible with the standard MAC with a higher degree of overall network performance gain.

Future work will be based on testing the protocol by introducing exponential back off instead of using a linear backoff when the packet retries, so that the protocol can withstand and accommodate high degree of contention. It shall also focus on using hop count values in designing the inter frame spacing to prioritize those packets travelled with higher hops.

REFERENCES

[1] P. Mohapatra; J. Li; C. Gui, "Qos in mobile Ad Hoc networks," *Wireless Communications, IEEE* , vol.10, no.3, Pages.44,52, June 2003 doi: 10.1109/MWC.2003.1209595.

[2] T. Bheemarjuna Reddy; I. Karthigeyan; B.S. Manoj; C. Siva Ram Murthy, "Quality of service provisioning in ad hoc wireless networks: a survey of issues and solutions", *Elsevier - Ad Hoc Networks*, Volume 4, Issue 1, January 2006, Pages 83-124, ISSN 1570-8705.

[3] J. Zheng; D. Simplot-Ryl; S. Mao; B. Zhang, "Advances in Ad Hoc Networks II", *Elsevier - Ad Hoc Networks* 10, Pages 661-663, 2012.

[4] K. Kosek-Szott, "A survey of MAC layer solutions to the hidden node problem in Ad Hoc networks", *Elsevier - Ad Hoc Networks,* vol. 10 Pages 635-660, 2012.

[5] L. Khoukhi; H. Badis; L. Merghem-Boulahai; M. Esseghir, "Admission control in wireless ad hoc networks: a survey", *EURASIP Journal on Wireless Communications and networking, Springer Open Journal*, 2013:109.

[6] P. Gupta; P.R. Kumar, "The Capacity of Wireless networks", *IEEE Transactions on Information Theory*, 46(2): Pages 388-404, March 2000.

[7] J. Marchang; B.V. Ghita; D. Lancaster , "Hop-Based Dynamic Fair Scheduler for Wireless Ad-Hoc Networks", *Proceedings of 7th IEEE International Conference on Advanced Networks and Telecommunications Systems* (ANTS), ISBN: 978-1-4799-1477-7, 2013.

[8] J Li; C Blake; D.S.J. De Couto; H.I. Lee; M. Robert, "Capacity of Ad Hoc Wireless Networks", *ACM SIGMOBILE*, ISBN 1-58113-422-3/01/07 Rome, Italy.

[9] X. Su; S. Chan; H.M. Jonathan, "Bandwidth Allocation in Wireless Ad Hoc networks: Challenges and Prospects", *IEEE Communications Magazine* , Accepted from Open Call, Pages 80-85, 2010.

[10] C. Li; H. Che; S. Li, "A wireless channel capacity model for quality of service," *Wireless Communications, IEEE Transactions on* , vol.6, no.1, Pages.356-366, Jan. 2007 doi: 10.1109/TWC.2007.05282.

[11] IEEE 802.11 WG, International Standard for Information Technology – *Telecommunications and Information Exchange Between Systems – Local and Metropolitan Area Networks* – Specific Requirements – Part11: "Wireless Medium Access Control (MAC) and Physical Layer (PHY) Specifications, ISO/IEC 8802-11:1999(E) IEEE Std. 802.11, 1999".

[12] IEEE 802.11 WG, 802.11e IEEE Standard for Information Technology- *Telecommunications and Information Exchange Between Systems – Local and Metropolitan Area Networks* – Specific Requirements Part 11: "Wireless LAN Medium Access Control (MAC) and Physical Layer (PHY) specifications": Amendment 8: "Medium Access Control (MAC) Quality of Service Enhancements, 2005".

[13] A. Torres; C.T. Calafate; J.C. Cano; P. Manzoni, "Assessing the IEEE 802.11e QoS effectiveness in multi-hop indoor scenarios", *Ad Hoc Networks*, Volume 10, Issue 2, March 2012, Pages:186-198,ISSN-1570-8705.

[14] Y. Xiao, "IEEE 802.11e: QoS provisioning at the MAC layer" *Wireless Communications, IEEE* , vol.11, no.3, Pages .72-79,June,2004-doi:10.1109/MWC.2004.1308952.

[15] P. Wang; H. Jiang; W. Zhuang, "IEEE 802.11e enhancement for voice service," *Wireless Communications, IEEE* , vol.13, no.1, Pages.30-35, Feb. 2006 doi: 10.1109/ MWC.2006.1593522.

[16] Y. Yi; S Shakkottai, "Hop-b y-Hop Congestion Control Over a Wireless Multi-Hop network", IEEE/ACM Transactions On Networking, Vol. 15, No. 1, February 2007,Pages:133-144.

[17] Y. Yu; G.B. Giannakis, "Cross-layer congestion and contention control for wireless ad hoc networks," *Wireless Communications, IEEE Transactions on* , vol.7, no.1, Pages 37-42, Jan.,2008,doi:10.1109/TWC.2008.060514.

[18] F. Wang; O. Younis; M. Krunz, "Throughput-oriented MAC for mobile ad hoc networks: A game-theoretic approach", *Ad Hoc Networks*, Volume 7, Issue 1, January 2009, Pages 98-117, ISSN 1570-8705.

[19] M. Kaynia; N. Jindal; G.E. Oien, "Improving the Performance of Wireless Ad Hoc Networks Through MAC Layer Design," *Wireless Communications, IEEE Transactions on* , vol.10, no.1, Pages 240-252, January 2011 doi: 10.1109/TWC.2010.110310.100316.

[20] D. Jung; J. Hwang; H. Lim; K.J Park; J.C. Hou, "Adaptive contention control for improving end-to-end throughput performance of multi-hop wireless networks," *Wireless Communications, IEEE Transactions on* , vol.9, no.2, Pages 696-705, February 2010 doi: 10.1109/TWC.2010.02.081205.

[21] W. Yu; J. Cao; X. Zhou; X. Wang; K.C.C. Chan; A.T.S. Chan; H.V. Leong, "A High-Throughput MAC Protocol for Wireless Ad Hoc Networks," *Wireless Communications, IEEE Transactions on* , vol.7, no.1, Pages.135-145, Jan. 2008 doi: 10.1109/TWC.2008.06094.

[22] D.J. Deng; C.H. Ke; H.H. Chen; Y.M. Huang, "Contention window optimization for ieee 802.11 DCF access control," *Wireless Communications, IEEE Transactions on* , vol.7, no.12, Pages 5129-5135, December 2008 doi: 10.1109/T-WC.2008.071259.

[23] P.H.J. Nardelli; M. Kaynia; P. Cardieri; M. Latva-aho, "Optimal Transmission Capacity of Ad Hoc Networks with Packet Retransmissions," *Wireless Communications, IEEE Transactions on* , vol.11,no.8, Pages 2760-2766, August 2012doi: 10.1109/TWC.2012. 062012.110649.

Jims Marchang is a PhD student at the Centre for Security, Communications, and Network research (CSCAN) laboratory, Plymouth University, UK. He is a recipient of the Best Student Paper award of Advanced Computing and Communications (ADCOM) International Conference, 2007, hosted at Indian Institute of Technology, Guwahati and a member of IEEE. His main research topic includes QoS in Ad-Hoc Networks, Internet of Things, and network security based on intrusion detection.

Dr Bogdan Ghita received his PhD in 2005 from Plymouth University, UK. He is Associate Professor at Plymouth University and leads the networking area within the Centre for Security, Communications, and Network research. His research interests include computer networking and security, focusing on the areas of network performance modelling and optimisation, wireless and mobile networking, and security. He has been principal investigator in a number of industry-led, national, and EU research projects. He was a TPC member for over 40 international conference events as well as a reviewer for IEEE communications letters, computer communications, and future generation computer systems journals and he is the chair of the International Networking Conference series.

Dr David Lancaster is a Lecturer at Plymouth University. He received his PhD in Physics in 1984, but has been working on various computing topics for the past 15 years.

Hierarchical-distributed approach to movement classification using wrist-mounted wireless inertial and magnetic sensors

Peter Sarcevic[1], Laszlo Schaffer[1], Zoltan Kincses[1], *Member, IEEE*, Szilveszter Pletl[1], *Member, IEEE*

Abstract—**Wireless Sensor Networks (WSN) can be used for patient monitoring, analysis of daily activities, and emergency or fall detection. Using a WSN of two wrist mounted 9-degree-of-freedom (9DOF) sensor boards, movement classification can be reliably done. The sensor boards or motes contain a tri-axial magnetometer, a tri-axial gyroscope, and a tri-axial accelerometer. If the classification is assigned to only one mote, which is using the data from both sensor boards, high energy consuming wireless data transfer is required. In this paper, a hierarchical-distributed algorithm is presented, where the motes are calculating their own movement classes, which can be combined on one mote, to determine the movement of the entire body and arms. The proposed method requires less and smaller classifiers, which can be easily implemented on low performance motes. Eleven movement classes were constructed, and data were collected with the help of nine subjects. By distributing the process, some movements can be merged and seven classes can be defined for each arm. Their combination determines the class of the entire body. Two classification hierarchies were tested and various Time-Domain Features (TDF) were calculated with different processing window widths. Altogether 48 training and validation data sets were constructed by different configurations of the sensors. The Minimum Distance (MD) with usage of the Linear Discriminant Analysis (LDA) dimension reduction method and the MultiLayer Perceptron (MLP) classifiers with and without LDA were tested.**

Index Terms—**movement recognition, wireless 9 degree-of-freedom sensor motes, time-domain features, linear discriminant analysis, minimum distance classifier, multilayer perceptron**

I. INTRODUCTION

Using Wireless Sensor Networks (WSN) for analysis of human behaviour is a widely studied field of health and medical applications. It can be used for fall and emergency detection [1-2], telerehabilitation [3], analysis of the daily activities, patient or health monitoring [4-5], and also for industrial applications. Because of their low cost and small energy consumption, miniature inertial and magnetic sensors are reliably used for these applications. Usually these sensors are built into a small, light-weight sensor board, capable of digital signal processing and wireless communication. These boards or motes can be wearable and therefore they can make real-time wireless monitoring widely available.

A potential application of the proposed system is an intelligent WSN, which can be used for emergency detection, or monitoring the movement of the patients in a hospital, or at home.

During the research of movement classification numerous combinations of the sensor types, position of the sensors, various defined movement classes and classification methods were found in the literature. In [6] a detection and classification system of a surveillance sensor network is presented, which classifies vehicles, persons, and persons carrying ferrous objects, and tracks them with the use of Passive Infrared Sensor (PIR), microphone, and magnetometer. Hierarchical classification architecture was used to distribute sensing and computation tasks at different levels of the system. Altogether the system achieved 90% accuracy with 200 sensor nodes. An application of biomedical wireless sensor network is presented in [7], which attempts to monitor patients for specific conditions. The proposed system uses a three-axis accelerometer to determine if the arm movement of a person is similar to a person suffering from a seizure. The results of the presented algorithms have been verified on test subjects and showed few occurrences of false positives. One waist-worn bi-axial accelerometer was used in [8] to monitor the movement of patients. A decision tree algorithm was used for classification, which classified the movements into six movement classes, with a success rate of 90%. In [9] a tri-axial waist mounted accelerometer was used for movement monitoring, in which the classification was done by a hierarchical binary decision tree algorithm into seven classes. The overall accuracy of the system was 97.7% over a data set of 1309 movements. In [10-12] a tri-axial magnetometer, a tri-axial gyroscope and a tri-axial accelerometer were used together as a sensor unit. In [10] five sensor units were used on the body. Multi-Template Multi-Match Dynamic Time Warping (MTMM-DTW) was used to classify the movement into 8 movement classes with 93.46% accuracy. Six sensor units were used in [11] for fall detection. Least-Squares Method (LSM), k-Nearest Neighbour (k-NN), Support Vector Machines (SVM), the Bayesian Decision Making (BDM), DTW and the Artificial Neural Network (ANN) classifiers were tested based on time and frequency domain features. The results showed that 99% accuracy is

achievable with k-NN and LSM. In [12] five sensor units were used on the body. The Bayesian Decision Making (BDM), the Rule-Based Algorithm (RBA), the Least-Squares Method (LSM), the k-Nearest Neighbour (k-NN), DTW, Support Vector Machines (SVM), and the Artificial Neural Networks (ANN) classifiers were compared to each other to classify into 19 movement classes. The results showed that the performance of the SVM and k-NN is good, but the BDM was the best.

In this paper an energy-efficient hierarchical-distributed classification algorithm is presented, which is tested with two different hierarchies, and is capable of classifying the movement of a human body based on the data of two wrist-mounted wireless 9DOF sensor boards. The constructed wearable wireless sensor system enables easy data collection and real-time monitoring.

This paper is organized as follows. The fundamental problem and the proposed solution are described in Section II. The used hardware and software for the measurements is presented in Section III. Section IV presents the classes, the classification algorithm and the used techniques for the classification. In Section V the generation of the input data and the usage of the extracted features are presented. Section VI presents the experimental results, while Section VII concludes the paper.

II. PROBLEM DESCRIPTION

A. Previous Research

As described in [13], above 90% recognition efficiency can be achieved using proper processing window widths if the TDFs computed using the measurement data from both sensor motes are used together in the classification algorithm. Multiple classifiers were compared with and without the use of the LDA-based dimension reduction, and their comparison showed that the Multi-Layer Perceptron networks (MLP) are the most effective, but the performance of the Minimum Distance (MD) classifier is also acceptable, moreover, the implementation and training of this classifier is faster and easier. The LDA-based dimension reduction of the input data before the classifiers can improve the recognition efficiency, and decrease the training time.

B. The Problem

Since the proposed algorithm in [13] uses the measurement data from both sensor motes, its implementation requires high energy consuming radio communication for data transfer between the motes, or the two motes and a processing unit. It was reasonable to split the classification algorithm into a hierarchical approach to get a distributed network, so the motes can calculate their own movement classes. Using the proposed hierarchical-distributed technique, only the movement class is needed to be transferred periodically based on the value of the window shift. The determined classes are combined to get the movement of the entire body and arms. Besides that using the proposed algorithm less data transfer is required via wireless communication, the classifiers have less

input features and output classes. Therefore it is more energy-efficient and easier to implement the algorithm on motes.

C. The System

The proposed system is shown in Fig. 1. Both motes compute their own movement class, based on the measured acceleration, angular velocity and magnetization. After the classification, the movement class of the slave mote is sent to the master, which combines the received class with its own class. In the last step, the final result is computed, which can be sent to another wireless device, and can be used for monitoring purposes. Another approach can be to send the computed classes from both motes to a processing unit, which combines the classes and use the final result. In this case a more energy-efficient operation is available, because it is not necessary to keep the reading channel operating on the motes. Only the processing unit has to read the data from the sensor boards.

Previously a distributed approach was proposed in [14], where the seven classes of the two arms were organized into one hierarchical level. Two training setups were tested where the training data were constructed in two different ways in case of the merged classes. The results showed no major difference between the two setups. The MLP and MD classifiers were tested with LDA-based dimension reduction, and the two methods provided similar results. The classifiers were trained for the arms separately, and the results showed only slight differences in the recognition efficiencies for the two arms. The algorithm would be improved if the same classifier could be used for the two arms.

III. MEASUREMENT

Analyzing the movement of the human body with a wearable sensor system can be very tiring for the subjects. Therefore it is necessary for a wearable movement classification system to be small, comfortable and also wireless. For this reason a 9-degree-of-freedom (9DOF) sensor board, the IRIS wireless mote was chosen.
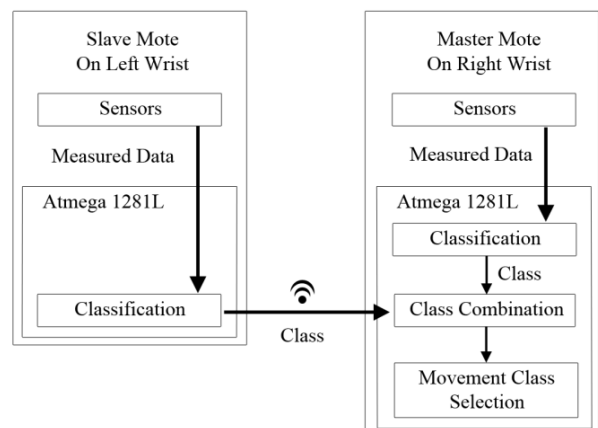
The IRIS mote contains an Atmel ATmega 1281L 8-bit
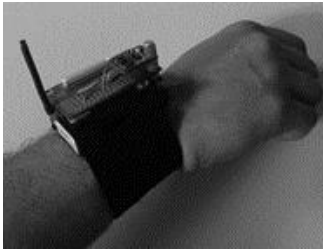

Fig.1. The architecture of the used system

Fig. 2. Wireless sensor mote mounted on the wrist

Fig. 3. The first movement hierarchy

microcontroller, a 512 Kbyte Flash with SPI communication, and an RF231 radio transceiver. The radio transceiver can provide a maximal data throughput of 250 kbps, and its outdoor range is 300 m. The transceiver requires 16 mA current draw for receiving, and 17 mA for transferring data. The IRIS mote has a 51-pin expansion interface, which can be used to connect different sensor boards to the mote. An MDA100 prototype board was used for connecting the 9DOF sensor board to the IRIS mote.

The sensor board contains a tri-axial ADXL345 accelerometer, a tri-axial ITG3200 gyroscope, and a tri-axial HMC5883L magnetometer. The accelerometer`s maximal sampling rate is 3.2 kHz, and it can measure up to ±16g. The gyroscope has a ±2000 deg/s measurement range, and 8 kHz sampling rate. The magnetometer is capable of an output resolution of ±8Ga and it can sample on 160 Hz.

With the help of the TinyOS operation system a sensor driver was implemented on the IRIS mote to configure the sensors and read the measured data. The driver and the sensors communicate via I2C communication protocol. A TinyOS application was developed for data collection, which can read the measurement values with 8 ms (125 Hz) period, and the measured data are sent to a BaseStation mote. The data from the BaseStation mote are forwarded to the PC via serial communication, and are then stored on the PC.

The measurements were performed using two wrist-mounted IRIS motes, as seen in Fig. 2. Eleven movement classes were defined for the movement classification and the data were collected for all classes with the help of 9 subjects. Data were collected in 20 s long sessions for each class. With the sampling rate of 125 Hz this means 2500 measures per mote.

IV. CLASSIFICATION ALGORITHM

A. Measurement System

Movement classes were constructed in order to recognize specific arm movements in stationary positions and also during the movement of the body. The used movement classes were the following:

1. "standing without movement of the arms";
2. "sitting with the arms resting on a table";
3. "walking";
4. "turning around in one place";
5. "jogging";
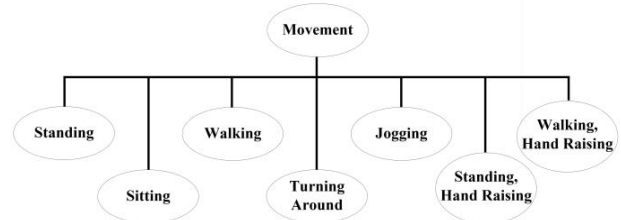6. "raising and lowering the left arm during standing";
7. "raising and lowering the right arm during standing";
8. "raising and lowering both arms during standing";
9. "raising and lowering the left arm during walking";
10. "raising and lowering the right arm during walking";
11. "raising and lowering both arms during walking".

In order to develop a distributed algorithm in which the two motes can determine their own movement type, some classes were merged by the role of the arm in the given movement. For example classes 1 and 6 can be merged in the case of the right arm, because in both cases the right arm is not moving during standing. This way the reduction of the classes can be done in four cases, so the total number of classes can be reduced to seven for both arms. Merging for the left arm can be done for the classes: 1 and 7; 3 and 10; 6 and 8; 9 and 11. For the right arm these cases are: 1 and 6; 3 and 9; 7 and 8; 10 and 11. Two different approaches were tested for the classification hierarchy. In the first approach the movements are equally distributed, all of them are on the same level. The first hierarchy can be seen in Fig. 3. The second hierarchy has been distributed into five parts based on specific selections of the main movement classes. The classification algorithm uses these distributions to decide which element of the hierarchy matches the actual movement. The second hierarchical approach can be seen in Fig. 4, and the corresponding distributions (D) are:

- D1: 1 or 2
- D2: a or b
- D3: c or d or e
- D4: I or II
- D5: III or IV

For example the first distribution D1 decides that the actual movement is stationary or not. Through these distributions a hierarchical classification can be provided.

B. Movement Classes

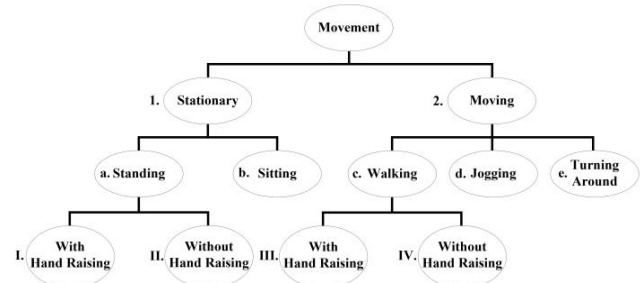In Fig. 5 the main parts of the classification algorithm are

Fig. 4. The second movement hierarchy approach

Hierarchical-distributed approach to movement classification
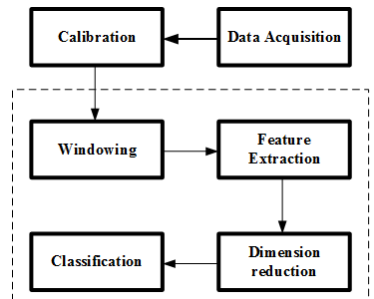using wrist-mounted wireless inertial and magnetic sensors

Fig. 5. The parts of the classification algorithm

shown. Before the data could be preprocessed, the raw measurement data have to be calibrated. A previously proposed offline evolutionary algorithm-based method was used for the calculation of the calibration parameters, which is presented in [15]. For the necessity of the easy implementation requirements only TDFs were used, because the ATmega 1281L is a low performance microcontroller. Fixed length processing windows were used for the feature extraction, which were shifted by predefined values. The used window width and shift pairs were: 80ms width and 40ms shift, 200ms width and 40ms shift, 400ms width and 80ms shift, 800ms width and 80ms shift. Similarly as in [16], the used TDFs were:

1) *Mean Absolute Value (MAV):* The mean of the summed absolute values inside a processing window.

2) *Willison AMPlitude (WAMP):* Records the number of times, when the amplitude change of the incoming signals within a processing window are higher than a given threshold level

3) *Number of Zero Crossings (NZC):* The number of the algebraic sign changes of the signal, with a predefined threshold value.

4) *Number of Slope Sign Changes (NSSC):* The number of direction changes in the signal, where from three consecutive values the change of the first or the last are larger than a predefined threshold.

5) *Waveform Length (WL):* The length of the waveform in a window, which is calculated by the sum of absolute changes between two measurement values.

C. Dimension Reduction

The previous researches proved that the LDA dimension reduction method can improve the speed of the training process, and its implementation is easy, since it needs only multiplications and addition.

As described in [17-18], the purpose of the LDA method is to seek a set of optimal vectors, denoted by $\mathbf{W} = [w_1, w_2, \ldots, w_l]$, such when the Fisher criterion is maximized, which is given in (1).

$$J(\mathbf{W}) = tr\left(\mathbf{W}^T \mathbf{S_B} \mathbf{W} / \mathbf{W}^T \mathbf{S_W} \mathbf{W}\right), \qquad (1)$$

where $\mathbf{S_w}$ is the within-class scatter matrix, and $\mathbf{S_b}$ is the between-class scatter matrix. Equation (2) defines the within-class scatter matrix:

$$\mathbf{S_W} = \sum_{j=1}^{c} \sum_{i=1}^{N_J} \left(\mathbf{x}_i^j - \boldsymbol{\mu}_j\right)\left(\mathbf{x}_i^j - \boldsymbol{\mu}_j\right)^T, \qquad (2)$$

where $\mathbf{x}_i^j$ represents the ith sample of class j, $\boldsymbol{\mu}_j$ is the mean of class j, C is the number of classes, and N_j is the number of samples in class j. The between-class scatter matrix is defined in (3):

$$\mathbf{S_b} = \sum_{j=1}^{c} \left(\boldsymbol{\mu}_j - \boldsymbol{\mu}\right)\left(\boldsymbol{\mu}_j - \boldsymbol{\mu}\right)^T, \qquad (3)$$

where $\boldsymbol{\mu}$ is the mean of all classes.

The goal of the LDA method is to maximize the between-class variance while the within-class variance should be minimized. The solution of this problem is obtained by an eigenvalue decomposition of $\mathbf{S_W^{-1}S_B}$, and take the eigenvectors corresponding to the highest eigenvalues. There are *C-1* generalized eigenvectors.

D. Classifiers

Two classification techniques were used, which based on previous researches proved to be the best. The classifiers were the following:

1) *Minimum Distance classifier:* Calculates the Euclidean distance from the mean values in each class for each feature. The output is the class, which has the smallest sum.

2) *MultiLayer Perceptron networks:* As described in [19-20], the MLP is a feed forward the Artificial Neural Network (ANN), where neurons are organized into three or more layers. The first layer is the input and the last is the output layer, between them are one or more hidden layers, and each layer are fully connected to the next one using weighted connections. The base elements are the neurons, which have an activation function that maps the sum of their weighted inputs to their output. The most common method for training is the backpropagation algorithm, which uses the gradient descent technique that attempts to minimize the squared error between target values and the network output values.

V. INPUT DATA GENERATION

Altogether 48 different data sets were constructed depending on the TDF calculation methods, the four window width and shift pairs, and the four used sensor combinations. Data from five subjects were used for the training and the remaining four for the validation of the system. The accelerometer, the gyroscope, and the magnetometer were tested separately as well as together.

Three different TDF calculation types were used. In the first type, the features for the x, y and z sensor axes were calculated separately (SEP), so one TDF type contains three different values. In the second type, the sum of the separately calculated TDF values was computed (SUM), thus possible misplacement of the motes on the wrists, or differences in movements of two persons can have smaller impact. In the third type, the TDFs were calculated using the magnitude (VL), which means that the features were calculated based on the changes in the Euclidean norms of the vectors. Some TDFs

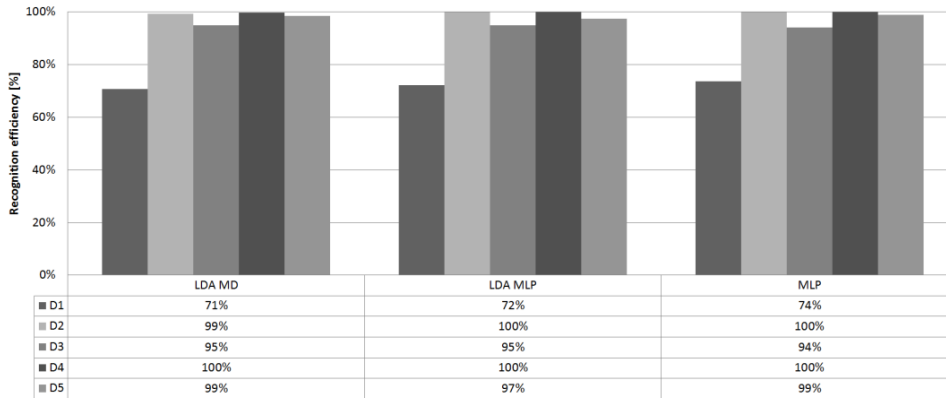|	LDA MD	LDA MLP	MLP
■ D1	71%	72%	74%
■ D2	99%	100%	100%
■ D3	95%	95%	94%
■ D4	100%	100%	100%
■ D5	99%	97%	99%

Fig. 6. Comparison of the classifiers in the case of the second hierarchy with validation efficiencies before combination, with 800 ms window length and separated TDFs of the sensors used together

were not computed, because they have no sense. The NZC cannot be calculated using the magnitudes, since they are always positive. The measurements of the magnetometer cannot be used for the MAV feature, because in ideal circumstances the magnitude of the magnetic field is constant.

For the generation of the datasets for both tested hierarchies the data from the merged classes were used in equal quantities, and the datasets for the two arms were used together for the training of the classifiers.

VI. EXPERIMENTAL RESULTS

All 48 data sets for the two training setups were tested with the classifiers described in III.C. The inputs of the MLP were used with and without the LDA dimension reduction method, while the inputs of the MD classifier were tested only with LDA. In [13] the LDA proved to improve the training process, but since in the second tested hierarchy type the classifiers have to classify into two or three classes, which means drastic dimension reduction, it was reasonable to test the MLP without dimension reduction too.

In the second tree-based hierarchy the first distribution is the significant, because the training and the validation efficiencies of the other distributions can reach 100% in the case of separated TDF values when the sensors were used together, or the accelerometer alone. Therefore, when speaking about the efficiency of the second hierarchy, the values are meant to be the values of the first distribution, because in a decision tree a wrong decision on the first level will cause a wrong final outcome. In Fig.6 the comparison of the distributions are seen in the case separately calculated TDF values with 800 ms window width, when all sensors were used together.

A. Minimum Distance Classifier

Analyzing the classification results achieved with the MD classifier on validation data before the combination on the master mote, it can be seen that in the separate cases the performance of the first hierarchy is higher, than the performance of the second hierarchy. The difference is about 5%. Despite this, in the sum and vector length cases the second hierarchy is proved to be better, the maximum

difference can be 20%. With the magnetic sensor with the first hierarchy the classification accuracy is around 30% with the smallest, and 35% with the biggest window width, but with the second hierarchy the accuracy with the smallest window is around 60%, and with the biggest it is 70%. In the first and second hierarchy, using the separately calculated TDF values 2-5% higher recognition rate can be observed with the magnetometer only. Comparing the efficiency of the gyroscope and the accelerometer, the accelerometer provides better results for all window widths in the first, but the gyroscope proved to be better in the second hierarchy only with 1-2%, if the TDFs are calculated for the axes separately. In the case of the summed and magnitude-based TDFs, the gyroscope provides the better recognition rates in both hierarchies. With the largest window width the highest efficiency with the accelerometer or the gyroscope is up to 65% in the case of the first hierarchy, and 71% in the second. Of course, the best classification rates can be reached when all the three sensors were used together. In this case, around 10% higher accuracy can be reached compared to the results of the accelerometer or the gyroscope using the same TDF types with the first, and 5% with the second hierarchy. But in some cases using only the gyroscope or the accelerometer are proved to be better. The highest efficiency with the first hierarchy was 77% and it can be reached with the separately calculated TDF values. With the second hierarchy the highest accuracy was 74%, and it can be reached with the magnitude-based TDF values.

Viewing the recognition on the training data with the first hierarchy, it can be seen that they were classified 10-15% more correctly than the validation data. The recognition of the training data with the second hierarchy proved to be 20-30% better than the validation data. For example when the recognition rate on the validation samples was 77%, the same was 92% on the training.

After the classes were combined, 80% on training and 60% on validation efficiency were reached with the first, and also 80% on training, but 55% on validation accuracies were reached with the second hierarchysamples.

B. *MultiLayer Perceptron*

It is obvious that with few hidden neurons only low recognition rates can be achieved, but by increasing the number of hidden neurons a converging tendency can be observed in the recognition efficiencies to a maximal value. Based on previous research it can be concluded, that this maximal value can be reached at most with 15 hidden neurons. Therefore increasing further the number of hidden neurons is not necessary, but it is required to know, that which hidden neuron number provides the best recognition rate. Consequently, the training of the MLPs for all data sets was tested with 1-15 hidden layer neurons, and the setups with the best recognition rates on validation data were used for comparison.

Before the combination of the final class selections, with the use of the LDA dimension reduction and the MLP networks on validation data in the case of the first hierarchy, the accuracy of the magnetometer is around 40%, the accelerometer and the gyroscope have very similar results, and they can provide around 70% efficiency with 800 ms window width. In the case of the second hierarchy the efficiency of the magnetometer is around 65%, the accelerometer and the gyroscope have also very similar around 70% accuracy with the window width of 800 ms. Using all three sensor types almost 80% accuracy can be achieved with both hierarchies. For the first hierarchy with all sensor configurations the results are significantly better when the TDFs are calculated separately for the sensor axes. For the second hierarchy only the magnetometer provides better results with separately calculated TDF values, the other sensors provide better results with the magnitude-based calculation. The maximum efficiency of the two hierarchies are very similar, the difference is about 1.5%. The recognition rates in the case of the training data are very similar between the MLP and MD

classifiers in the case of the second hierarchy. In the first hierarchy there are 5-10% differences between the results.

The MLP without LDA dimension reduction proved to be better both on and validation with 2-3% efficiency.

After the master mote combined the classes from the motes the highest validation efficiency was 66% with the first hierarchy, and 63% with the second in the case of the separated calculations of the TDFs with the use of all sensors together. On training data, the maximal accuracy in the case of the first hierarchy was around 82% and about 74% with the second.

The best training results can be seen in Fig. 7. and the best validation efficiencies in Fig. 8, on the figures the best accuracies of the MLP of [13] and the MLP of the proposed system with the required feature numbers shown, were compared, where V1 means the first and V2 means the second hierarchy type. The system of [13] used the data of the arms together, and classified them on the master mote. For the comparison after the combination of the classes, the MLP was used without LDA, because the simple MLP is better in the case of few classes. On validation data the best efficiency of [13] is 87%, while the proposed system provides 66% with the first, and 63% with the second hierarchy in the case of 800 ms window length, separately calculated TDF values using all sensors together. In the same circumstances on the training data the best accuracy of [13] is 100%, while it is 82% with the first, and 74% with the second hierarchy. The results of [13] are significantly better, and it is proved, that using the data from the arms together is a good approach, but energy consumption reduction has a decreasing impact on the efficiencies. On the other side, energy efficiency and lowering energy consumption in our growing civilization are very important, so the further development of the proposed system could be necessary, maintaining the reduced energy

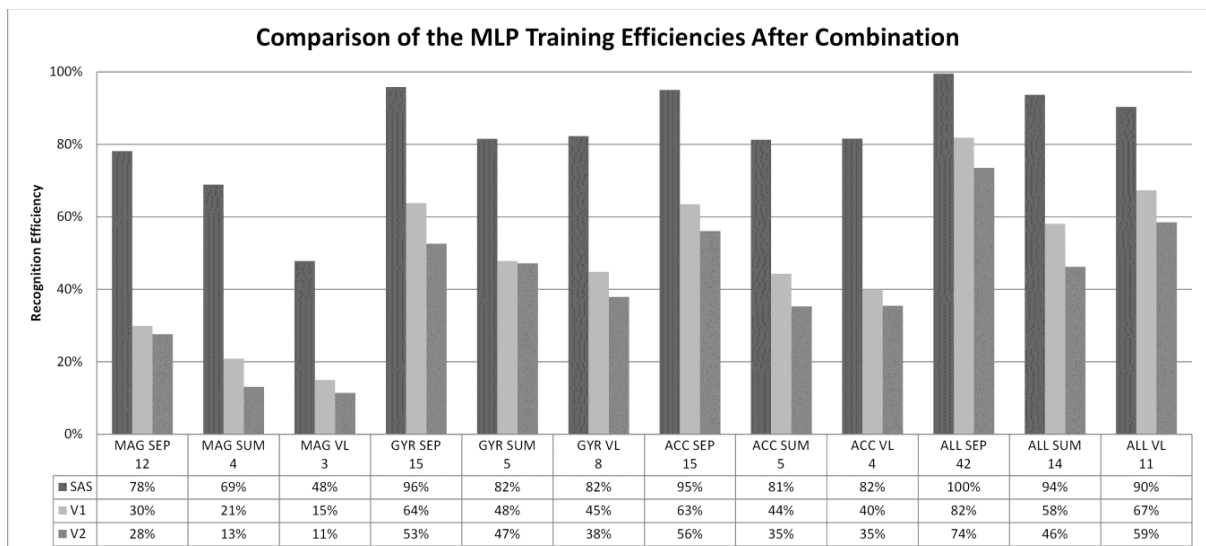|	MAG SEP 12	MAG SUM 4	MAG VL 3	GYR SEP 15	GYR SUM 5	GYR VL 8	ACC SEP 15	ACC SUM 5	ACC VL 4	ALL SEP 42	ALL SUM 14	ALL VL 11
SAS	78%	69%	48%	96%	82%	82%	95%	81%	82%	100%	94%	90%
V1	30%	21%	15%	64%	48%	45%	63%	44%	40%	82%	58%	67%
V2	28%	13%	11%	53%	47%	38%	56%	35%	35%	74%	46%	59%

Fig. 7. Comparison of the MLP training efficiencies after combination, 800 ms windows length, with the required feature numbers shown,
Abbreviations: MAG – Magnetometer, GYR – Gyroscope, ACC – Accelerometer, ALL – The TDFs of the three sensors together, SAS – Results from [13],
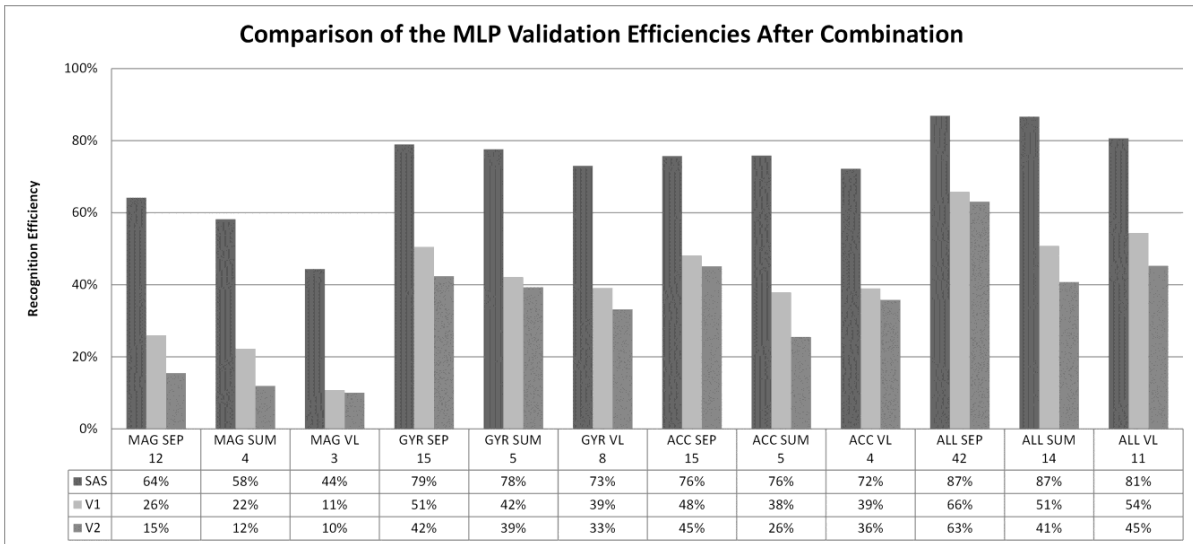V1 – First Hierarchy, V2 – Second Hierarchy

Fig. 8. Comparison of the MLP validation efficiencies after combination, 800 ms windows length, with the required feature numbers shown,
Abbreviations: MAG – Magnetometer, GYR – Gyroscope, ACC – Accelerometer, ALL – The TDFs of the three sensors together, SAS – Results from [13],
V1 – First Hierarchy, V2 – Second Hierarchy

consumption, but increasing the recognition rates.

Table 1 describes the needed RF communication and CPU computation tasks for each mote in the different algorithm types. The proposed algorithm in [13] can be realized in two different ways. In the first realization the slave mote has to send the measurement values (18 bytes/sampling cycle) to the master mote and the master mote makes the computation of the TDFs for both motes. In the second approach the slave computes the TDFs and only these values are sent to the master mote. The number of TDF values depends on the used configuration (10-50 bytes), and they should be sent after

every window shift. In the proposed hierarchical- distributed approach the computation is equally done by the two units, and only the movement class of the slave mote (1 byte) should be transferred to the master mote after every window shift.

As shown in [13], the needed memory for the implementation of the three tested classification methods is very similar. The needed memory in case of different number of inputs for the two tested hierarchical-distributed approaches and the non-distributed approach in case of the MLP classifier can be seen in Fig 9. For the calculation of needed bytes ten hidden layer neurons were applied for the non-distributed approach, V1, and D1 of V2, while for D2-D5 in V2 only one neuron was used. The results show that for the implementation of V1 less memory is needed than in case of the non-distributed approach, since the movements need to be classified into fewer classes, which reduces the size of the artificial neural network. It can be also noticed that V2 is the most memory consuming of the three methods.

Table 2 summarizes the comparison of the efficiencies based on the separately calculated TDF values.

TABLE I
RF COMMUNICATION AND CPU TASKS FOR THE MOTES

Radio communication	Master mote	Slave mote
Master processing (transmission of measurement data)	Reception of measurement data	Transmission of measurement data
Master processing (transmission of TDF values)	Reception of TDF values	Transmission of TDF values
Distributed processing	Reception of the slave mote`s movement class	Transmission of the arm`s movement class

| CPU computation tasks		
Master processing (transmission of measurement data)	Computation of the TDFs for both motes; computation of the movement class of the entire body and arms	None
Master processing (transmission of TDF values)	Computation of the TDFs; computation of the movement class of the entire body and arms	Computation of the TDFs
Distributed processing	Computation of the TDFs; computation of the arm`s movement class; class combination	Computation of the TDFS; computation of the arm`s movement class
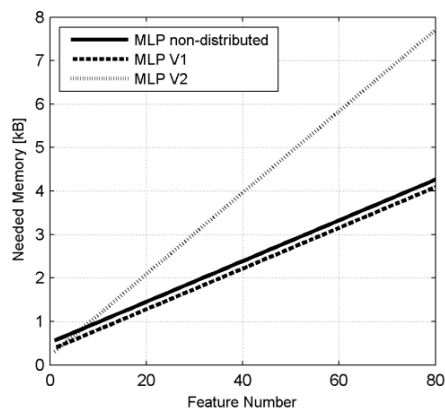
Fig. 9. The memory consumption in case of the MLP classifiers

TABLE II
SUMMARY OF SEPARATELY CALCULATED TDF BASED EFFICIENCIES, IN CASE OF 800 MS WINDOW WIDTH

Hierarchy	First								Second							
Sensor	MAG		GYR		ACC		ALL		MAG		GYR		ACC		ALL	
Combination (Before/After)	B.	A.	B.	B.	B.	A.	B.	A.	B.	A.	B.	A.	B.	A.	B.	A.
LDA MD T. (%)	51	36	76	70	75	74	92	74	89	53	93	56	90	55	97	80
LDA MD V. (%)	35	25	65	59	66	60	77	60	68	49	71	51	70	50	71	55
LDA MLP T. (%)	55	25	79	58	83	62	96	80	90	27	95	53	90	47	99	64
LDA MLP V. (%)	41	22	66	52	67	54	78	61	65	20	70	45	70	40	72	58
MLP T. (%)	58	30	84	64	84	63	98	82	91	28	98	53	95	56	100	74
MLP V. (%)	46	26	68	51	69	48	79	66	67	15	71	42	73	45	74	63

VII. CONCLUSION

In this paper, a hierarchical-distributed movement classification algorithm was described and tested for an energy-efficient system built up from two wrist-mounted wireless 9DOF sensor boards.

Results showed that the MLP classifier for few classes is better without LDA dimension reduction. Also the results of the MD classifier with LDA are similar to the MLP with LDA. In the proposed system the MLP classifier provides the best training with 82% and validation with 66% efficiencies in the first hierarchy, and 74% on training, 63% on validation accuracies in the second hierarchy in the case of separately calculated TDF values using all sensors together with 800 ms window length. In the proposed system the best classifier is the MLP with the first hierarchy, because the LDA dimension reduction has small effect on few classes, so the numbers of dimensions are few too. The results of the proposed system have been compared to the results of a previous approach, which used the data from the arms together, but classified them on the master mote. The final result is that a system that classifies the data on the master sensor board is better in recognition rates, but requires more energy. Therefore keeping in mind the low energy consumption the proposed system could be acceptable with further development on the recognition rates.

The implementation of the proposed system is more optimal than the algorithm presented in [13], but further development is required to reach the recognition rates of [13].

Future work could be the development of a better algorithm, the testing of more feature extraction techniques, or energy consumption optimization.

REFERENCES

[1] P. Kumar, P.C. Pandey, "A wearable inertial sensing device for fall detection and motion tracking", IEEE India Conference (INDICON), pp. 1-6, 2013

[2] Y. S. Delahoz and M. A. Labrador, "Survey on Fall Detection and Fall Prevention Using Wearable and External Sensors", Sensors Sensors for Globalized Healthy Living and Wellbeing, pp. 19806-19842, 2014

[3] J.M. Winters; Y. Wang, J.M. Winters, "Wearable sensors and telerehabilitation", IEEE Engineering in Medicine and Biology Magazine, Volume: 22 , Issue: 3, pp. 56-65, 2003

[4] A. Pantelopoulos; N.G. Bourbakis, "A Survey on Wearable Sensor-Based Systems for Health Monitoring and Prognosis", IEEE Transactions on Systems, Man and Cybernetics: Systems, Volume: 40, Issue: 1, pp. 1-12, 2009

[5] A. Rehman, M. Mustafa; N. Javaid, U. Qasim, Z. A. Khan, "Analytical Survey of Wearable Sensors"IEEE Seventh International Conference on Broadband, Wireless Computing, Communication and Applications (BWCCA), pp. 408-413, 2012

[6] L. Gu, D. Jia, P. Vicaire, T. Yan, L. Luo, A. Tirumala, Q. Cao, T. He, J. A. Stankovic, T. Abdelzaher, B. H. Krogh, "Lightweight Detection and Classification for Wireless Sensor Networks in Realistic Environments", Proceedings of the 3rd international conference on Embedded networked sensor system (SenSys), pp. 205-217, 2005

[7] T. R. Burchfield, S. Venkatesan," Accelerometer-Based Human Abnormal Movement Detection in Wireless Sensor Networks", Proceedings of the 1st ACM SIGMOBILE international workshop on Systems and networking support for healthcare and assisted living environments (HealthNet), , pp. 67-69, 2007

[8] A. Redondi, M. Chirico, L. Borsani, M. Cesana, and M. Tagliasacchi, "An integrated system based on wireless sensor networks for patient monitoring, localization and tracking," Elsevier Ad Hoc Networks, Volume 11, Issue 1, pp. 39–53, January 2013

[9] M. J. Mathie, B.G. Celler, N.H. Lovell, A.C.F. Coster, "Classification of basic daily movements using a triaxial accelerometer", Springer Medical and Biological Engineering and Computing, vol. 42, Issue 5, pp 679-687, 2004

[10] A. Yurtman and B. Barshan, "Automated evaluation of physical therapyexercises using multi-template dynamic timewarping on wearable sensor signals," Computer Methods and Programs in Biomedicine, vol. 117, Elsevier, 2014, pp. 189-207.

[11] A. T. Ozdemir and B. Barshan, "Detecting Falls with Wearable Sensors Using Machine Learning Techniques," Sensors, vol. 14, MDPI, 2014, pp. 10691-10708.

[12] K. Altun, B. Barshan, and O. Tuncel, "Comparative study on classifying human activities with miniature inertial and magnetic sensors", Elsevier Pattern Recognition, vol. 43, pp. 3605-3620, 2010

[13] P. Sarcevic, Z. Kincses and Sz. Pletl, "Comparison of different classifiers in movement recognition using WSN-based wrist-mounted sensors," IEEE Sensors Applications Symposium (SAS), pp. 1-6, 2015

[14] P. Sarcevic, Z. Kincses Sz. Pletl and L. Schaffer," Distributed movement recognition algorithm based on wrist-mounted wireless sensor motes", IEEE European Wireless, pp. 1-6, 2015

[15] P. Sarcevic, Sz. Pletl and Z. Kincses, "Evolutionary algorithm based 9DOF sensor board calibration," IEEE International Symposium on Intelligent Systems and Informatics (SISY), pp. 187-192, 2014

[16] B. J. Borbely, Z. Kincses, Zs. Voroshazi, Z. Nagy, and P. Szolgay, "Analysis of myoelectric signals using a Field Programmable SoC," IEEE Proceedings of European Conference on Circuit Theory and Design (ECCTD), pp. 1-4, 2013

[17] A. M. Martinez, and A. C. Kak, "PCA versus LDA," IEEE Transactions on Pattern Analysis and Machine Intelligence, vol. 23, pp. 228-233, 2001

[18] C. Yao, Z. Lu, J. Li, Y. Xu and J. Han, "A subset method for improving linear discriminant analysis," Neurocomputing, vol. 138, Elsevier, 2014, pp. 310-315.

[19] T. Mitchell, "Machine learning,", McGraw-Hill, pp. 432, 1997.

[20] P.M. Atkinson, , A.R.L. Tatnall," Introduction Neural networks in remote sensing", International Journal of Remote Sensing , Volume 18, Issue 4, pp. 699-709, 1997

Peter Sarcevic was born in Subotica, Serbia. He received his B.Sc. degree in electrical engineering from Subotica Tech – College of Applied Sciences, Serbia, in 2010, and his M.Sc. degree in electrical engineering from the Széchenyi István University, Gyor, Hungary, in 2013. Currently he is pursuing his Ph.D. degree in computer science from the University of Szeged, Hungary. His research interests include wireless sensor networks, pattern recognition, digital signal processing, embedded systems, and artificial intelligence.

Laszlo Schaffer was born in Szekszard, Hungary. He received his B.Sc. degree in engineering information technology from University of Szeged in 2013, and his M.Sc. degree in computer science and technology from University of Szeged in 2015. Currently he is pursuing his Ph.D. degree in computer science at Department of Technical Informatics, University of Szeged. His research interests include FPGA-based prototype development, wireless sensor networks, embedded systems, digital signal processing, and movement recognition.

Zoltan Kincses (M'06) was born in Gyula, Hungary. He received his M.Sc. degree in information technology from University of Veszprem in 2006 and B. S. degree in electrical engineering from University of Pannonia in 2008, and Ph. D. degree in information science and technology from the University of Pannonia in 2013.

From 2009 to 2013 he was an assistant lecturer with the Department of Computer Algorithms and Artificial Intelligence, University of Szeged. Since 2013 he has been an assistant professor with the Department of Technical Informatics, University of Szeged. His research interests include the implementation of FPGA-based cellular wave computers, FPGA-based image processing and myoelectric signal processing, movement recognition and development of wireless sensor networks.

Szilveszter Pletl (M'15) was born in Subotica, Serbia. He received his M.Sc. degree in electrical engineering from the Faculty of Technical Sciences at the University of Novi Sad, Serbia, in 1987, and his Ph.D. degree in engineering disciplines of electrical engineering disciplines from the Budapest University of Technology and Economics in 2001. He joined the Institute of Informatics, University of Szeged, in 2008 as a college professor. His current interests include research and development of intelligent solutions for industrial applications and wireless sensor networks.

Design of Pipelined Adaptive DFE Architecture
For High Speed Channel Equalization

A. Mandal, *Student Member, IEEE*, R. Mishra, *Member, IAENG*

Abstract— An adaptive equalizer is a vital and essential component for high-speed reliable data transmission through wired as well as wireless communication channels to minimize Inter Symbol Interference (ISI). The non-linear Adaptive Decision Feedback Equalizer (ADFE) finds enormous use in applications where the channel distortion is severe for a linear equalizer to handle. High hardware cost of the system makes an urge to redesign it in order to minimize overall circuit complexity and cost. In this paper, realization of COordinate Rotation Digital Computer (CORDIC) based pipelined ADFE architecture using reformulated least-mean-square (LMS) algorithm has been presented. The realization results area efficient, better speed and throughput with good convergence. The efficacy of the proposed equalizer is corroborated with MATLAB simulations for mitigation of severe channel distortion arise due to ISI in high speed communication systems.

Index Terms— Inter Symbol Interference (ISI), Adaptive Decision Feedback Equalizer (ADFE), CORDIC, LMS algorithm, Feed Forward Filter (FFF), Feedback Filter (FBF), Pipelined Architecture.

I. INTRODUCTION

WHEN channel frequency response deviates from the ideal of flat magnitude and linear phase response, both tails of the transmitted pulse will interfere with the neighboring pulses creating an *Inter Symbol Interference* (ISI) and it may lead to erroneous decision that increases the probability of error. To overcome this problem an equalizer at the receiver with a transfer function which is essentially an inverse of the channel transfer function is required [1]. So within the channel pass-band, ADFE ideally forms inverse transfer function to eliminate ISI .The performance of non-linear ADFE is better on a channel with spectral nulls in their frequency response characteristics than the linear equalizer which introduces significant amount of additive noise present in the received signal by introducing a large gain [2].

Since last few decades, a tremendous inclination among the researchers toward the implementation of CORDIC algorithm [3, 4] in various applications of digital signal processing arena had been witnessed. The modularity, compatibility, pipelinability, numerical stability and efficiency in generation of trigonometric and hyperbolic function have made the

CORDIC algorithm suitable for implementation of fast Fourier transform (FFT), discrete Fourier transforms (DFT), adaptive lattice filter and many more applications [5, 6]. In this paper, an adaptive transversal filter has been designed with a pipelined CORDIC unit as a core processing element in the equalizer for filtering and filters weight updating. Unlike the conventional LMS algorithm, the rotational angles rather than the tap weights are updated directly. The most popular and highly robust LMS algorithm has been efficiently mapped to obtain trigonometric form of LMS algorithm which facilitates in incorporating CORDIC processing element to participate in filtering as well as weight updating operations of the Feed Forward Filter (FFF) of the ADFE. Due to trivial bit length, decision feedback loop (DFL) has been simplified with general purpose multiplier to reduce complexity of the Feedback Filter (FBF). The proposed architecture uses CORDIC blocks instead of multipliers in the FFF and hence is more efficient in terms of internal numerical errors and power consumption.

The ADFE is widely used equalization technique for radar, antenna beam forming, digital communication systems, wireless video telephony, magnetic storage and many more applications [7, 8]. Wide variants of ADFE are available in the literature [9-12]. However, pipeline design of ADFE is known to be a difficult task for high speed applications. It is well known fact that the clock rate is limited by DFL. A lot of researches have been done to reduce hardware overhead and at the same time, to obtain better convergence. In this paper, we have used pipeline design technique throughout the architecture to reduce hardware complexity and to obtain high throughput for high speed applications. The modular design of multiplier has been incorporated to avoid place and route problem during physical layout. The combination of modified booth encoding (MBE) techniques [13, 14] along with partial product reduction [15-17] have facilitated in reduction of overall latency of the design to a single adder which has been implemented with carry look-ahead adder (CLA). This kind of design not only facilitates in easy implementation on FPGA device, but also reduces complexity significantly as compared to multiplier and accumulator (MAC) based design. The CORDIC processing element has been used by optimizing the quantization error [18] and to facilitate easy implementation of the equalizer for digital signal processing application. The convergence behaviors under various step sizes and its ability to generate inverse transfer function in severe channel mismatched situation have been adequately analyzed.

The rest of the paper is organized as follows. In the next section, we review the simple LMS algorithm and subsequently mapped into trigonometric form. In section III, CORDIC algorithm has been revisited and corresponding pipelined architecture is implemented. Section IV deals with the design of pipelined Adaptive Decision Feedback Equalizer along with explanation of associated components used with the design. Performance analysis of proposed design and discussion part of the paper is accommodated section V and finally, concluding remarks are presented in section VI.

II. REVIEW OF LMS ALGORITHM FOR CORDIC BASED APPLICATION

The LMS algorithm is one of the simplest as well as robust adaptive algorithms available in literature. We would like to reformulate LMS in trigonometric form for our design. Let the FIR filter is linear discrete time filter $x(n)$ and $d(n)$ are input and desired output sequence of the FIR filter (**Fig. 1**).
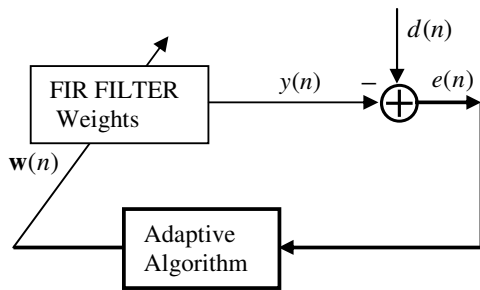

Fig. 1. LMS algorithm to update FIR filter weights

Let $\mathbf{w}$ and $\mathbf{x}(n)$ are filter coefficient and input vector of N-tap filter,

$$\mathbf{w} = [w_0, w_1, \ldots\ldots, w_{N-1}]^T$$
$$\mathbf{x}(n) = [x(n), x(n-1), \ldots\ldots, x(n-N+1)]^T \quad (1)$$

The output signal of the adaptive filter, $y(n)$, can be computed as the inner product of $\mathbf{w}(n)$ and $\mathbf{x}(n)$.

$$y(n) = \sum_{m=0}^{N-1} w_m(n)x(n-m) = \mathbf{w}^T(n)\mathbf{x}(n) \quad (2)$$

The error signal $e(n)$ is expressed as the difference between the desired response $d(n)$ and the filter output $y(n)$, i.e,

$$e(n) = d(n) - \mathbf{w}^T(n)\mathbf{x}(n) \quad (3)$$

The weight vector is updated iteratively in such manner that the mean-square error (MSE), ε is minimized.
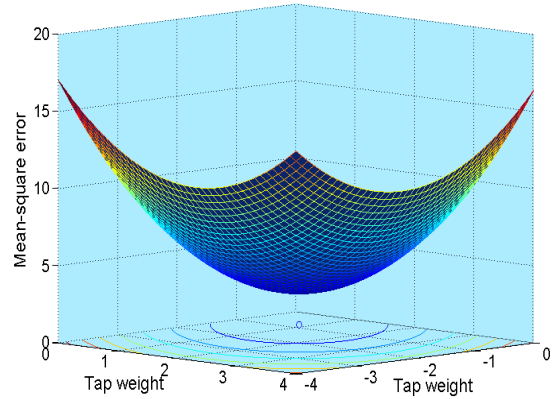

Fig. 2 Error surface curve to derive optimal weight of a FIR filter

$$\varepsilon \equiv E\{e^2(n)\}. \quad (4)$$

$$= E\{d^2(n)\} - 2\mathbf{w}^T\mathbf{p} + \mathbf{w}^T\mathbf{R}\mathbf{w} \quad (5)$$

where $\mathbf{R} \equiv E[\mathbf{x}(n)\mathbf{x}^T(n)]$ is the input auto-correlation matrix and $\mathbf{p} \equiv E[\mathbf{x}(n)d(n)]$ is the cross-correlation vector. Solving the equation, $\nabla_w \varepsilon = 0$, the optimal weights of a FIR filter can be derived.

$$\mathbf{w}_{opt} = \mathbf{R}^{-1}\mathbf{p}. \quad (6)$$

The direct calculation of the optimum filter weight ($\mathbf{w}_{opt}$) from $\mathbf{w}_{opt} = \mathbf{R}^{-1}\mathbf{p}$ is not practicable as matrix inversion involves huge complex multiplications. To reduce hardware overhead in terms of multiplier, steepest descent search method can be used for the design. The expression for steepest descent search method can be written for n-th index as

$$\mathbf{w}(n+1) = \mathbf{w}(n) - \frac{\mu}{2} \times \nabla_w \varepsilon \Big|_{w=w(n)} \quad (7)$$

where μ is step-size which is responsible for determining the convergence speed of the design. Putting $\mathbf{R}$ and $\mathbf{p}$ in equation (7), we get the simplest LMS algorithm in the following form:

$$\mathbf{w}(n+1) = \mathbf{w}(n) + \mu\,\mathbf{x}(n)\,e(n) \quad (8)$$

The pipelined implementation of conventional LMS algorithm is difficult because of its recursive behavior. That is why delayed LMS (DLMS) algorithm has been used. The feedback error, $e(n)$ generated at the n-th iteration cannot be available at the same iteration for weight updating process. The delay is referred to adaptation delay. If the adaptation delay is generated for L numbers of pipelined stages, the error in DLMS algorithm will be corresponds to $(n - L)_{th}$ iteration for

updating current filter weight in place of recent most error. Therefore, the iterative equation of delayed LMS algorithm can be expressed as:

$$\mathbf{w}(n+1) = \mathbf{w}(n) + \mu\, \mathbf{x}(n-L)\, e(n-L) \qquad (9)$$

The iterative LMS algorithm is required to be modified to include CORDIC processing element in the proposed architecture [19]. Let the tap weight w_k be

$$w_k = A_k \sin\theta_k \qquad (10)$$

w_k satisfies, $-A_k \le w_k \le +A_k$, and maps uniquely to a θ_k in the interval $[\,-\pi/2, +\pi/2\,]$. The function $\sin\theta_k$ is a monotonically increasing continuous function of θ_k, as it lies within $[\,-\pi/2 \le \theta_k \le +\pi/2\,]$, i.e. $\partial\varepsilon/\partial\theta_k$ has the same sign as that of $\partial\varepsilon/\partial w_k$ everywhere within the hypercube resulting in local minima or maxima less MSE. Using the equation (10), we can show the variation of error w.r.t angle variation as follows:

$$\partial\varepsilon/\partial\theta_k = \partial\varepsilon/\partial w_k \;.\; A_k \cos\theta_k \qquad (11)$$

$$\nabla_\theta\varepsilon = \Delta.\nabla_w\varepsilon \qquad (12)$$

Here Δ is $N \times N$ diagonal matrix whose k-th term can be given by: $\Delta_{k.k} = A_k \cos\theta_k$, $k = 0,1,.........,N-1$

Using the equations (6) and (12), we get the following

$$\boldsymbol{\theta}(i+1) = \boldsymbol{\theta}(i) - \frac{\mu}{2}\nabla_\theta\varepsilon \;\Big|_{\boldsymbol{\theta}=\boldsymbol{\theta}(i)} \qquad (13)$$

where, $\nabla_\theta\varepsilon = -2\Delta(\mathbf{p}-\mathbf{Rw})$

With replacing $\mathbf{p}$ and $\mathbf{R}$ by $\mathbf{x}(n)d(n)$ and $\mathbf{x}(n)\mathbf{x}^T(n)$ in equation (13), we get the trigonometric form of LMS algorithm as:

$$\boldsymbol{\theta}(n+1) = \boldsymbol{\theta}(n) + \mu\boldsymbol{\Delta}(n)\mathbf{x}(n)e(n) \qquad (14)$$

$$e(n) = d(n) - \sum_{k=0}^{N-1} \sin\theta_k(n)\, x(n-k)$$

The above form of LMS algorithm can be realized using CORDIC processing element. The sine/cosine terms generated by CORDIC can be utilized for filtering as well as updating filter coefficients in the equalizer.

III. Review of CORDIC Algorithm and Its Design

A. CORDIC Algorithm revisited

The CORDIC algorithm deals with the decomposition of the desired rotation angle into the weighted sum of a set of predefined elementary rotation angles. Each of them can be accomplished with simple shift-add operation for a desired rotational angle θ. It can be represented for M iterations of an input vector $(x,y)^T$ setting initial conditions: $x_0 = x$, $y_0 = y$, and $z_0 = \theta$ as $z_f = \theta - \sum_{i=0}^{M-1}\delta_i\alpha_i$. If $z_f = 0$ holds, then

$$\theta = \sum_{i=0}^{M-1}\delta_i\alpha_i \qquad (15)$$

i.e. the total accumulated rotation angle is equal to θ. δ_i, $0 \le i \le M-1$, denote a sequence of ± 1s that determine the direction of each elementary rotation. When M is the total number of elementary rotation angles, i-th angle α_i is given by:

$$\alpha_{m,i} = \frac{1}{\sqrt{m}}\tan^{-1}[\sqrt{m}\,2^{-s(m,i)}] = \begin{cases} 2^{-s(0,i)} \\ \tan^{-1}2^{-s(1,i)} \\ \tanh^{-1}2^{-s(-1,i)} \end{cases} \qquad (16)$$

where $m = 0$, 1 and -1 correspond to the rotation operation in linear, circular, and hyperbolic coordinate system respectively. For a given value of θ, the CORDIC iteration is given by:

$$\begin{bmatrix} x_{i+1} \\ y_{i+1} \end{bmatrix} = \begin{bmatrix} 1 & -\delta_i 2^{-i} \\ \delta_i 2^{-i} & 1 \end{bmatrix} \begin{bmatrix} x_i \\ y_i \end{bmatrix} \qquad (17)$$

and $z_{i+1} = z_i - \delta_i\alpha_i$

where $\alpha_i = \tan^{-1}2^{-i}$. To bring a unit vector to desired angle θ, the CORDIC algorithm gives known recursive rotations to the vector. The known rotational values are shown in **Table. I** as a Pre-Computed angle. Once the vector is at desired angle, the outcome of the X and Y coordinates of the vector are equal to $Cos\theta$ and $Sin\theta$ respectively. Let a unit vector in iteration 'i' is rotated by some angle θ_i, then the recursively updated equations are generated in the following form:

$$x_{i+1} = x_i\cos\delta_i\alpha_i - y_i\sin\delta_i\alpha_i$$

$$y_{i+1} = y_i\cos\delta_i\alpha_i + x_i\sin\delta_i\alpha_i \qquad (18)$$

The above equation can be simplified and written as

$$x_{i+1} = \cos\delta_i\alpha_i(x_i - y_i\tan\delta_i\alpha_i)$$

$$y_{i+1} = \cos\delta_i\alpha_i(y_i + x_i\tan\delta_i\alpha_i) \qquad (19)$$

The $\tan\alpha_i = \pm 2^{-i}$. So multiplication is converted into an arithmetic right shift. Since cosine is an even function, therefore $\cos(\alpha) = \cos(-\alpha)$. The iterative equation (19) can be reduced to

$$x_{i+1} = K_i(x_i - y_i\delta_i 2^{-i})$$

$$y_{i+1} = K_i(y_i + x_i\delta_i 2^{-i}) \qquad (20)$$

where $K_i = \cos\left(\arctan 2^{-i}\right) = 1\Big/\sqrt{(1+2^{-2i})}$ is known as scale factor for each iteration. If M iterations are performed, then scale factor, K, is defined as the multiplication of every K_i.

$$K = \prod_{i=0}^{M-1} K_i = \prod_{i=0}^{M-1} 1\Big/\sqrt{(1+2^{-2i})} . \qquad (21)$$

The elementary functions sine and cosine can be computed using the rotation mode of the CORDIC algorithm if the initial vector starts at $(|K|,0)$ with unit length. The final outputs of the CORDIC for the given input values $x_0 = 1$, $y_0 = 0$ and $z_0 = \theta$ are as follows:

$$x_f = K\cos\theta \ , \ y_f = K\sin\theta \ \text{and} \ z_f = 0 . \qquad (22)$$

Since the scale factor is constant for a given number of rotations, $x_0 = 1/K$ can be set to get purely $\sin\theta$ and $\cos\theta$ values.

B. Implementation of pipelined CORDIC:

In Pipelined CORDIC architecture, a number of rotational modules are incorporated and each module is responsible for one elementary rotation. The modules are cascaded through intermediate latches (**Fig. 3**). Every stage within the pipelined CORDIC architecture, only adder/subtraction is used. The shift operations are hardwired using permanent oblique bus connections to perform multiplications by 2^{-i}. The pre-computed values of i-th iteration angle α_i required at each module can be generated through required sequence of binary data within V_{cc} and G_{nd} using trivial hardware arrangements.

The delay is adjusted by using proper bit-length in the shift register. In the design of CORDIC module, adders and subtractor contribute the critical path. Since carry propagation delay in full adders is the source of delay, Carry Save Adder (CSA) was the obvious choice for the design. The use of these adders reduces the stage delay significantly [19]. With the pipelining architecture, the propagation delay of the multiplier is the total delay of a single adder.

So ultimately the throughput of the architecture is increased significantly as the throughput is given by: "*1/(delay due to a single adder)*". If an iterative implementation of the CORDIC is used, the processor would take several clock cycles to give output for a given input. But in the pipelined architecture, each pipeline stage takes exactly one clock cycle to pass one output. Again, to keep rotation angles within $-\pi/2 \le \theta_i \le +\pi/2$, the transformation of angles in different quadrant complementing corresponding MSBs has been illustrated in **Fig. 4**. A detailed study of various errors in pipelined CORDIC have been discussed in Mandal et al. [20]. The total error generated in the CORDIC block which uses 12 bits in its fractional part. Therefore, the upper limit of the total quantization error can be taken as 2^{-12} with considering scale factor K and iteration number n, the equation can be given by:
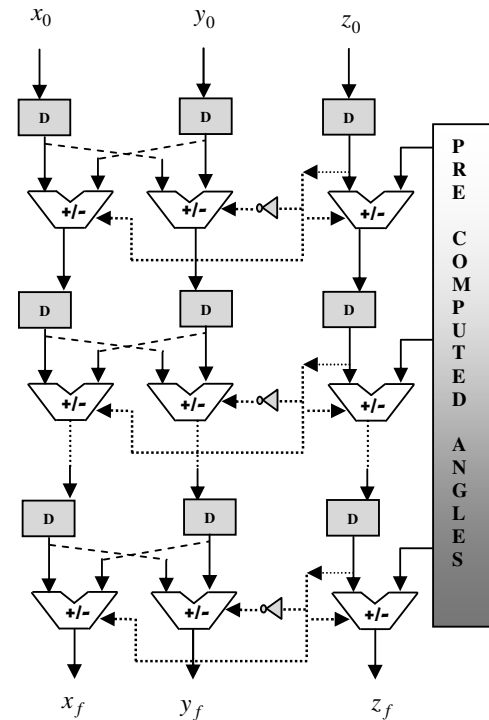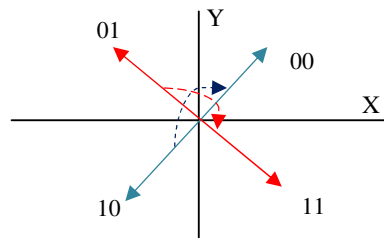

Fig. 3. The pipelined CORDIC

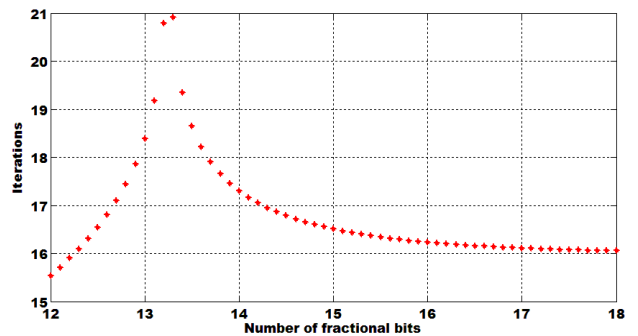Fig. 4 Quadrant transformation for CORDIC operation

Fig. 5 Word-length in fractional bits Vs number of iterations

Design of Pipelined Adaptive DFE Architecture
For High Speed Channel Equalization

TABLE I
COMPARISON WITH DIFFERENT CORDIC ARCHITECTURES BASED ON HARDWARE SYNTHESIS [21]

Designs	Area (sq. um)	Clock (ns)	TPT (per µs)	Latency (ns)	ACT (ns)	ADP
Conventional CORDIC	2987	2.52	36.07	27.72	27.72	82799
Fixed rotation CORDIC	2471	2.49	40.16	24.90	24.90	61527
Interleaved scaling	2674	2.56	55.8	17.92	17.92	47918
Separated scaling	4074	2.29	109.17	16.03	9.16	37317
Bi-rotation cascade	5819	2.21	226.24	15.47	4.42	25719
Proposed design	**3142**	**1.98**	**505.05**	**12.31**	**1.98**	**38678**

TPT stands for throughput, ACT stands for average computation time and ADP stand for area-delay product.

$$\frac{1}{2^{n-1}}*|v^*|+K*\sqrt{2}*2^{-b}\left(1+\sum_{j=0}^{n-1}\prod_{i=j}^{n-1}\sqrt{(1+2^{-2i})}\right)+2^{-b}$$

$$\leq 2^{-12} \qquad (23)$$

The above inequality is simulated in MATLAB to find out fractional bits of the internal word length of the CORDIC. The **Fig. 5** shows that when number of bits less than 14, the response of the CORDIC becomes complex and when bit number exceeds 14, the design works well. In view of the internal addition and subsequent error performance, 16 bit design has been preferred as fractional bits become almost independent of number of iterations at ≥ 16.

The time complexities of the proposed design and other various types of CORDIC architectures which have been published in recent times are compared. Unlike the proposed design, the conventional and few other designs available in the literatures uses adders, registers, barrel shifters and MUX which contribute toward hardware complexity. It has been seen that shifting operations using barrel-shifter for maximum of S shifts for the word-length can be implemented by $\lceil \log_2(S+1) \rceil$ stages of 2:1 MUX. Few designs have used ROM memory to store *arctan* angles as well as control signals for CORDIC operations. Therefore, the hardware complexity of the design also increases with increase in required word-length which leads to maximum number of shift operations for the design. We have compared our design with the other published work [21] in respect of clock period, throughput, latency and area which have been shown in **Table I** and **Table II** using TSMC 90-nm library.

TABLE II
TIME COMPLEXITY OF DIFFERENT CORDIC ARCHITECTURES [21]

Conventional CORDIC	$T_A+T_{FF}+5T_{MX}$
Fixed rotation CORDIC	$T_A+T_{FF}+5T_{MX}$
Interleaved scaling	$T_A+T_{FF}+5T_{MX}$
Separated scaling	$T_A+T_{FF}+4T_{MX}$
Bi-rotation cascade	$T_A+T_{FF}+2T_{MX}$
Proposed design	T_A

T_A, T_{FF} and T_{MX} stand for addition time, Flip-Flop delay and delays in 2:1 MUX respectively.

IV. ARCHITECTURE OF ADFE WITH CORDIC

The adaptive decision feedback equalizer consists of feed forward filter (FFF), feedback filter (FBF), decision device and error computation unit. A simple block diagram of ADFE has been shown in **Fig.** 6.
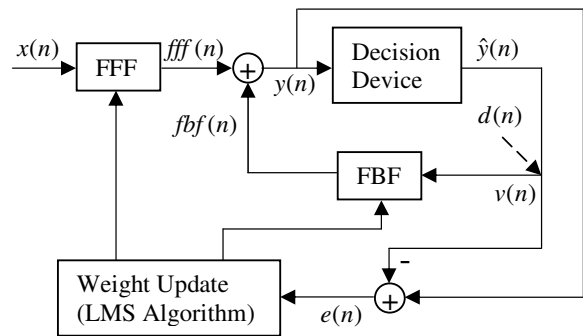

Fig. 6 Block diagram of a basic ADFE

A signal $x(n)$ arrives at the input to FFF filter. A decision device has been incorporated to give a decision based on $y(n)$ which is nothing but a sum of output of both feed forward and feedback filter. The decision result which is made on the input signal already detected previously is passed to FBF as an input. The error generated from the $y(n)$, $\hat{y}(n)$ and $d(n)$ is remain responsible for updating weights of the filters are being used in the design. The FFF in our design is a linear transversal filter which is implemented with a finite duration impulse response (FIR) filter with adjustable coefficients. The decisions made on the equalizer signal are fedback via a second transversal filter [22]. The elaborate internal design of proposed ADFE can be seen in **Fig. 7** which shows the error computation and weight updating phenomena through CORDIC based FFF and trivial multiplier based FBF filter respectively. If the detected symbols are stationary, then the ISI contributed by these symbols can be cancelled exactly by subtracting past symbol values with appropriate weight from the equalizer output. But channel response may not be same always. Therefore, the forward and feedback filter should adjust its coefficients simultaneously to counter the variation in channel response by minimizing the mean square error. At initial operation, the coefficients of the equalizer are needed to
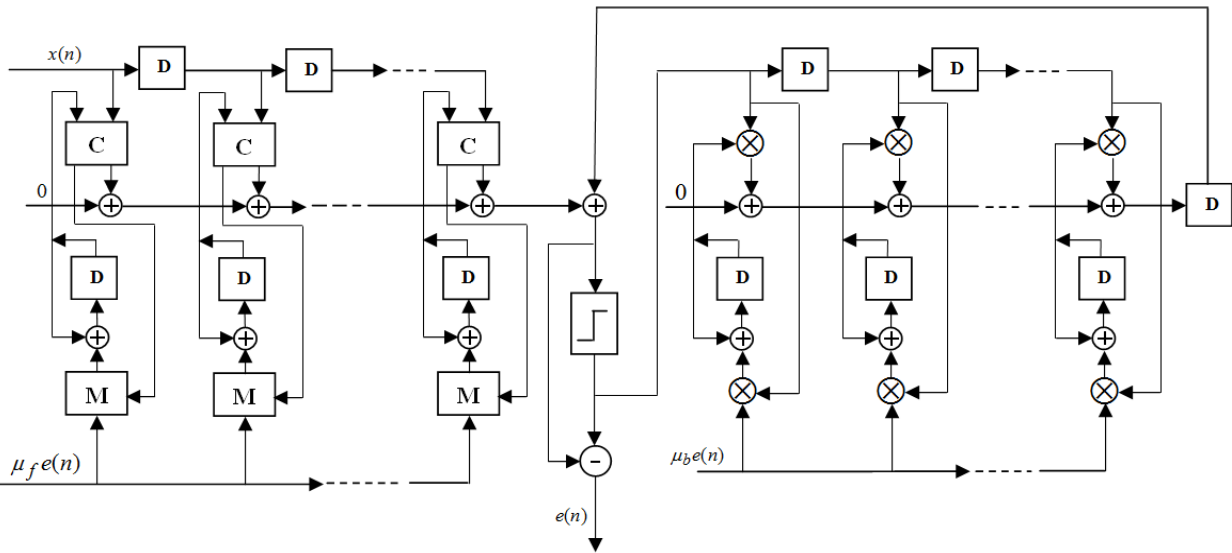
Fig. 7. Adaptive decision feedback equalizer using FFF and FBF filter

be adjusted as per the channel response and therefore, a known sequence of symbols named as training sequence is transmitted through the desired channel for this purpose. The design uses pipelined CORDIC unit as a main processing element. In circular rotation mode, CORDIC unit generates $\sin\theta$ and $\cos\theta$ which are the main ingredients for filtering and weight updating respectively in the proposed design. The pipelined technique has been adopted throughout the architecture to implement delayed version of trigonometric form of LMS algorithm in FFF and simple delayed LMS (DLMS) for FBF. The reason behind that is the inputs to the FBF are the transmitted symbols whose bit lengths are very small and hardware required for multiplication is trivial. But it is not the case for FFF filter. Adaptation delay in FFF

naturally more as compared to FBF. μ_f and μ_b are the step size used to compute the weight update term of FFF and FBF respectively to synchronize the error output.

Modified Booth encoding (MBE) algorithm has been widely used in implementation of multiplier due to its efficiency in reduction of partial products by half. The presented multiplication operations are performed using three steps as shown in **Fig 8 (a)**. All the partial products are generated in first step. For this purpose, popular MBE scheme has been employed and has not been discussed in detail in this design. The second step deals with reduction of all partial products in parallel structure using 4-to-2 adder. The third step uses fast adder named Carry Look-Ahead (CLA) to add the two numbers obtained from second stage to generate final product [23]. The reduction of partial products using 4-to-2 adder has been shown in **Fig. 8 (b)**. There are four 4-to-2 adder have been used to accommodate 16 partial product
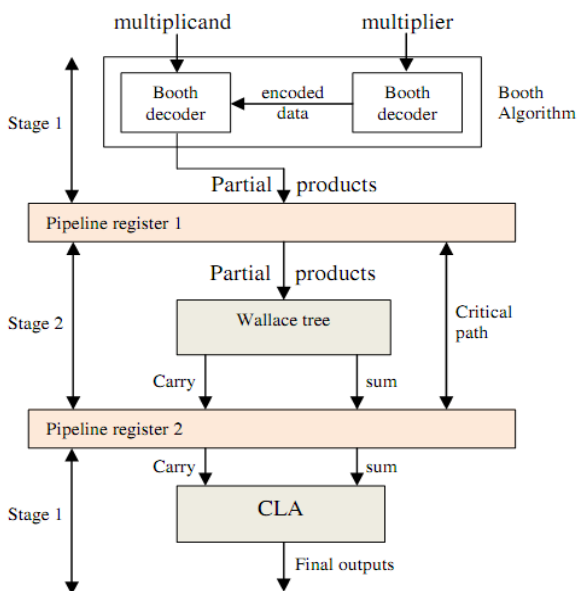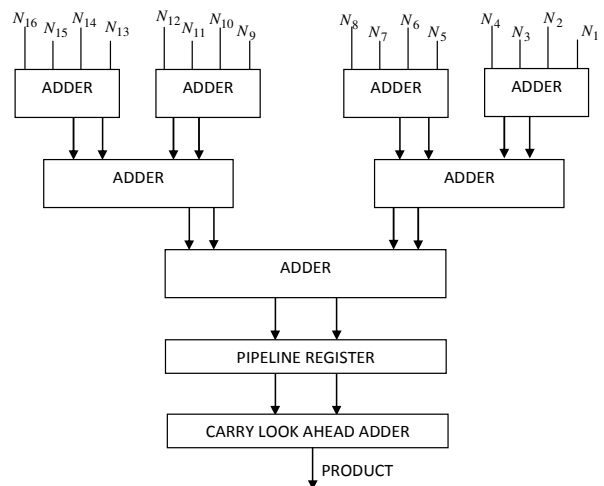

Fig. 8 (a) 3-stage pipelined multiplier

Fig 8(b). Partial product reduction scheme in association with final fast adder

generated from the input coming from CORDIC as well as error generator circuits. Each 4-to-2 adder receives four inputs and gives two outputs in terms of sum and carry. The adder cell consists of carry generator which receives three inputs from previous adder cell and a parity generator which generates a control signal for the two MUX to be selected.

The multiplier has been synthesized on Xilinx 13.4 using target device Spartan 3E xc3s250e-5-pq208. The resource utilization summary has been shown in **Table III.** The table shows the area efficiency of the design.

TABLE III
DEVICE UTILIZATION BY MULTIPLIER

Number of Slices:	45 out of 2448	1%
Number of Slice Flip Flops:	39 out of 4896	0%
Number of 4 input LUTs:	80 out of 4896	1%
Number used as logic:	63	
Number used as Shift registers:	17	
Number of IOs:	36	
Number of bonded IOBs:	36 out of 158	22%
Number of GCLKs:	1 out of 24	4%

V. PERFORMANCE ANALYSIS AND DISCUSSION

It is well known that pipelined CORDIC itself has got good convergence property which has been efficiently used in this application. Exact convergence analysis of proposed architecture using trigonometric LMS algorithm is not possible due to presence of nonlinearity of the filter as well as angle update equation. Using the iteration error generated in the equalizer, approximate convergence studies have been carried out.

The input sequence to the channel is considered to be QPSK data source. The generated signal is transmitted over a communication channel. The channel is complex and infected by noise which is additive and white Gaussian (AWGN). During the journey through the channel, the symbols are get corrupted due to various channel imperfection. A standard constellation has been utilized for training sequence for the equalizer. The equalizer is used to minimize the error at the receiver end by adjusting the filter weights in such a way to recover the constellation. The simulation environment has been created by utilizing total data 3000, training symbols 2000 and corresponding signal-to-noise ratio 30 dB. A 15-tap adaptive filter with centre placed at 8-th tap has been taken for simulation studies. The equalizer delay is set at 8. The coherent form of equalization has been considered where channel estimation is carried out to determine the amplitude as well as phase distortion created by channel imperfections or ISI. The tap weights are initialized to zero. The step size which is the guiding force for fast or slow conversion of the system is appropriately taken care. If $\mu \leq 0.001$ the convergent speed of the algorithm will be very slow and too large μ can cause instability. MATLAB Simulation for equalization on the received corrupted symbols and corresponding convergence performance of ADFE in terms of learning curves of the design at $\mu = 0.001$ and $\mu = 0.014$ has been shown in **Fig. 9** and **Fig 10** respectively.
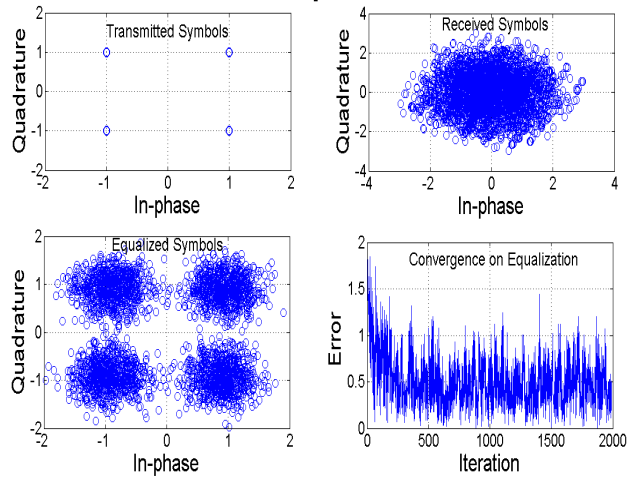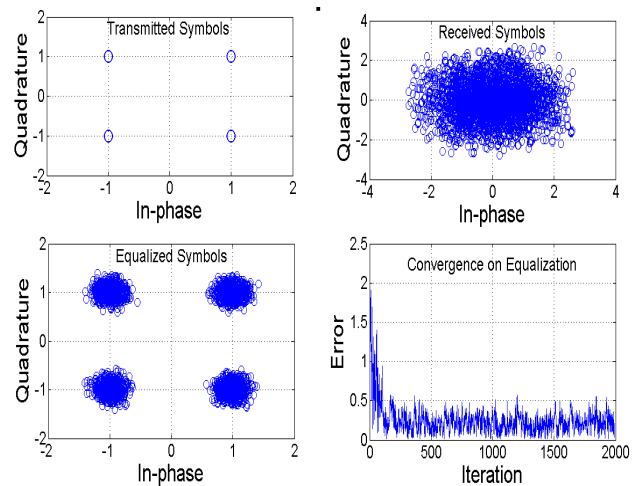

Fig. 9 Equalization on channel imperfection at μ=0.001

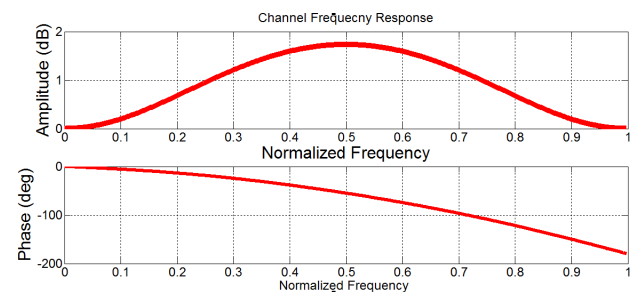Fig. 10. Equalization on channel imperfection at μ=0.014

Fig. 11 (a) The response of mismatched channel

The proposed design has been tested using randomly generated signal as an input for the equalizer which is to be used in mismatched channel. The equalization of mismatched channel has been shown in **Fig.11 (a)** whereas, **Fig.11 (b)** shows the equalizer response which is essentially inverse of the given channel response.
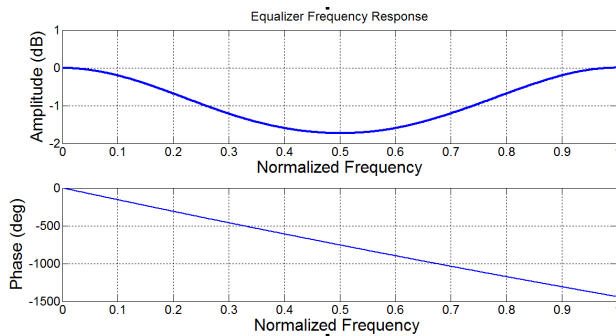
Fig. 11 (b) The equalizer response of the mismatched channel

VI. CONCLUSION

This paper presents realization of CORDIC based adaptive feedback equalizer using trigonometric form of LMS algorithm in mitigating severe Inter Symbol Interference (ISI) in AWGN channel. Based on the trigonometric reformulation of LMS algorithm, low-complexity ADFE architecture is designed. 50% of multipliers have been replaced in FFF by CORDIC unit to facilitate in easy implementation for weight updating and filtering purpose. To verify the validity of the proposed architecture, extensive MATLAB simulations have been carried out and the results shows the suitability of the design in respect of high speed channel equalization.

REFERENCES

[1] R. Mishra and A. Mandal, "Coordinate rotation algorithm based non-linear Adaptive Decision Feedback Equalizer", In *IEEE 2012 9th International Multi-Conference on Systems, Signals and Devices (SSD),* pp. 1-5, 2012.

[2] L. Fan, C. He, D. Wang and L. Jiang, "Efficient robust adaptive decision feedback equalizer for large delay sparse channel", *IEEE Transactions on Consumer Electronics,* vol. *51, no.* 2, pp. 449-456, 2005.

[3] J. E. Volder, "The CORDIC Trigonometric Computing Technique", *IRE Transactions on Electronic Computing*, vol. EC-8, pp. 330-334, Sept, 1959.

[4] Y. H. Hu, "CORDIC-based VLSI architectures for digital signal processing." *IEEE Signal Processing Magazine*, vol. 9, no. 3, pp. 16-35, 1992.

[5] P. K. Meher, et al., "50 years of CORDIC: Algorithms, architectures, and application*", IEEE Transactions on Circuits and Systems I: Regular Papers,* vol. 56, No. 9, pp. 1893-1907, 2009.

[6] Y. H. Hu, "On the convergence of the CORDIC adaptive lattice filtering (CALF) algorithm." *IEEE Transactions on Signal Processing,* vol. 46, no. 7, pp. 1861-1871, 1998.

[7] M. D. Yang, A. Y. Wu and J. T. Lai, "Fast convergent pipelined adaptive DFE architecture using post-cursor processing filter technique", *IEEE Transactions on Circuits and Systems II: Express Briefs,* , vol. *51, no.* 2, pp. 57-60, 2004.

[8] M. Magarini, L. Barletta and A. Spalvieri, "Efficient computation of the feedback filter for the hybrid decision feedback equalizer in highly dispersive channels". *IEEE Transactions on Wireless Communications,* vol. *11, no.* 6, pp. 2245-2253, 2012.

[9] A. M. Chan, and G. W. Wornell, "A class of block-iterative equalizers for intersymbol interference channels: Fixed channel results", *IEEE Transactions on Communications,* vol. *49, no.* 11, pp. 1966-1976, 2001.

[10] Y. C. Lin, S. J. Jou and M. T. Shiue, "High throughput concurrent lookahead adaptive decision feedback equalizer". *IET circuits, devices & systems*, vol. *6, no.* 1, pp. 52-62, 2012.

[11] R. Lopez-Valcarce, "Realizable linear and decision feedback equalizers: properties and connections", *IEEE Transactions on Signal Processing,* vol. *52, no.* 3, pp. 757-773, 2004.

[12] Á. Knapp and L. Pap, "General Performance Analysis of Binary Fading Channels with Measurement Based Feedback Channel Equalization", *Infocommunications Journal*, vol. VI, no. 1, pp. 1-9, 2014.

[13] A. Wu, C. K. Ng, and K. C. Tang. "Modified Booth pipelined multiplication."*Electronics Letters*, vol. 34, no. 12, pp. 1179-1180, 1998.

[14] F. Elguibaly "A fast parallel multiplier-accumulator using the modified Booth algorithm." *IEEE Transactions on Circuits and Systems II: Analog and Digital Signal Processing,* vol. 47, no. 9, pp. 902-908, 2000.

[15] R. S. Waters and E. E. Swartzlander, "A reduced complexity Wallace multiplier reduction," IEEE Transactions on Computers, vol. 59, no. 8, pp. 1134–1137, 2010.

[16] D. Galbi, et al. *U.S. Patent No. 4,901,270*, 1990, Washington, DC: U.S. Patent and Trademark Office.

[17] S.-R. Kuang, J.-P. Wang and C.-Y. Guo, "Modified booth multipliers with a regular partial product array," IEEE Transactions on Circuits and Systems II: Express Briefs, vol. 56, no. 5, pp. 404–408, 2009.

[18] Y. Hu, "The Quantization Effects of the CORDIC Algorithm", *IEEE Trans. on Signal Processing*, vol. 40, No. 4, pp. 834-844, 1992.

[19] M. Chakraborty, A. S. Dhar and S. Pervin, "CORDIC realization of the transversal adaptive filter using a trigonometric LMS algorithm", In *IEEE International Conference on Acoustics, Speech, and Signal Processing,* Vol. 2, pp. 1225-1228, 2001.

[20] A. Mandal and R. Mishra, "FPGA Implementation of Pipelined CORDIC for Digital Demodulation in FMCW Radar", *Infocommunications Journal,* 2013, vol. V, no. 2, p. 17-23.

[21] P. K. Meher and S. Y. Park, "CORDIC designs for fixed angle of rotation", *IEEE Transactions on Very Large Scale Integration (VLSI) Systems,* vol. *21, no.* 2, pp. 217-228, 2013.

[22] N. R. Shanbhag and K. K. Parhi, "Pipelined adaptive DFE architectures using relaxed look-ahead" *IEEE Transactions on Signal Processing, vol. 43, no.* 6, pp. 1368-1385, 1995.

[23] A. Mandal, R. Mishra, B. K. Kaushik and N. Z. Rizvi, "Design of LMS Adaptive Radar Detector for Non-homogeneous Interferences", *IETE Technical Review*, vol. 32, 2015. DOI: 10.1080/02564602.2015.1093436.

Amritakar Mandal received his M.Tech with specialization in VLSI from Shobhit University, India in 2009. He is currently working toward the Ph.D degree in the School of Information and Communication Technology, Gautam Buddha University, India. He has vast experience in Electronic Warfare (EW) and Surveillance Radar systems. His research interests include Radar Signal Processing and High Speed VLSI Design for Communication Systems.

Rajesh Mishra is currently working as Assistant Professor in School of Information and Communication Technology, Gautam Buddha University Greater Noida, Delhi NCR (India). He received his BE (Electronics Eng.), M. Tech and Ph. D. degree (Reliability Eng.) from Reliability Engineering Centre, IIT Kharagpur (India) in year 2000, 2004, and 2009 respectively. He has research interest in the area of reliability engineering, layout design for capacitated networks, and network optimization. He has published papers in several international journals of repute.

Traffic Simulation based on the Robocar World Championship Initiative

Norbert Bátfai, *Member, IEEE,* Renátó Besenczi, *Student Member, IEEE,* András Mamenyák,
Márton Ispány, *Member, IEEE*

Abstract—**Robocar World Championship or briefly OOCWC is a new initiative to create a community of people who share their interest in investigating the relationship between smart cities and robot cars with particular attention to the spread of robot cars in the near future. At the heart of this initiative is the Robocar City Emulator. It is intended to offer a common research platform for the investigation of the smart city simulations. In this paper, we review the recent advances of the OOCWC.**

Index Terms—smart city, traffic simulation, robocar, programming competition

I. Introduction

Based on some assumptions, by the year 2050, 70% of Earth's population will live in urban areas [1]. Urban infrastructures will face new challenges with this amount of population. In recent years, the domain called Smart City has become a vivid topic. Smart City applications contain solutions and research areas, such as intelligent city planning, crowd sourcing and crowd sensing, crisis and disaster management, etc. [2] The goal is to make the life of an urban population easier and provide sustainable development and an optimal distribution of available resources.

In recent years, many developments occurred in the automobile industry regarding the scope of autonomous cars, also known as driverless cars. Many companies are showing interest, such as the self-driving car pioneer, Google, or many German manufacturers, e.g. the Volkswagen Group. Also, the development of pure electric cars has shown major progress recently. These trends even seem to be accelerating. It is clear, one of the world's leading economic industries is facing a revolution; a paradigm shift is going to happen.

It can be an interesting question from the point of view of ICT and IT; how can these cars, which will be generally available in the near future, be assisted by city administration? What can a city controlled IT solution offer to these cars to allow them to be operated more practically, more economically and more efficiently?

Lets assume, in the near future, 50% of the cars in everyday life will be driverless. The car should have an optimal route if one would like to travel from one part of the city to the other. It can be a completely reasonable scenario that this route will be given by the city or, more specifically, by an IT solution coordinated by the city. This is reasonable, because the city has all the information necessary, such as traffic congestion, detours, accidents, road construction, rare events, etc, to produce an optimal route.

In this paper, we summarize the research and development results currently included in the RObOCar World Championship (OOCWC) platform. We will see in a working example, what we call "Police Edition" (described later), that the system can perform in an optimal way, to plan routes for individual entities and simulate traffic environments in almost every urban area of the world. We emphasize, this platform is currently a simulation platform, no actual traffic intervention occurs in the real world.

One useful feature of the system is adaptation to different uses. Different kinds of information is suitable for governmental travel, EMT actions, police events or civilian movements. As we will see in an example in Section II-B1, the system can be applied in each specific case.

The research and development process of the OOCWC is agile, with fast prototypes for every component. The platform, which is currently under development at the University of Debrecen, provides a competition where researchers and students can compare their knowledge in traffic analysis, route planning methods or even their coding skills. The currently available components of the system are open source and provide an opportunity for researchers and developers, who are interested in the relation of smart cities and autonomous cars, to try out their ideas and methods.

The OOCWC has many other possibilities. Besides providing routes to driverless cars and simulating traffic in cities, it will be able to collect data about cities with on-board traffic analysis. A database is being established for this data. Furthermore, the system can raise new questions in the ICT research domain: how can a car communicate with a city? The OOCWC is obviously a multidisciplinary platform (car industry, ICT and IT field, city administration, traffic analysis) which can bring us to the next step in smart cities: the automated city.

The rest of the paper is organized as follows. Sect. II sketches the overall architecture of the OOCWC platform to be developed and shows some main design requirements. In Sect. II-B we briefly introduce two rapid prototypes called "Justine" and "Justina". Finally, in Sect. III we give a brief summarization of the results from the first competitions and the results of our traffic measurement and analysis solutions.
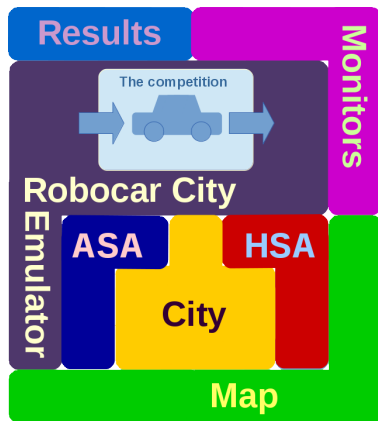
All authors are with the Department of Information Technology, University of Debrecen, H-4010 Debrecen PO Box 12, Hungary, e-mail addresses: batfai.norbert@inf.unideb.hu, netid21@mailbox.unideb.hu, mamenyaka@gmail.com, ispany.marton@inf.unideb.hu. Corresponding author: Norbert Bátfai, tel: +3652512900/ext.75228.

Fig. 1: The high-level "Tetris" plan of the OOCWC platform.

Related Works

It is not rare to use competitions in a given research and educational area, for example the RoboCup [3] focuses on artificial intelligence. We have suggested a similar initiative for smart city research.

The paper [4] presents a case study about investigation of replacing traditional cars with driverless cars in Singapore and [4, p. 10 Fig. 2] shows that the authors of the study have already used 10×10^5 number of vehicles but it may be noted that their simulation is not a realistic one in the sense that the simulated cars are not standalone agents.

Realistic traffic simulations have already been used in [5]. Here, it can be noted that our traffic simulation model can also be seen as a variant of the Nagel-Schreckenberg (NaSch) model [6] because we have used a cell-based approach as well.

Many traffic simulation models have been developed. In general, three classes exist: 1) The agent-based models (or microscopic models), which is the method presented in [7] and considered as a representative, modern approach of microscopic models. 2) The continuum models (or macroscopic models), there exists several solution, e.g. [8], [9]. 3) Hybrid models which work as a mixture of the two above, like [10]. Our rapid prototypes are agent-based systems. In addition, one of our prototypes called "Justine" can be considered as a standalone multi-agent system that has the ability to support multiagent programming competitions.

II. THE OOCWC PLATFORM

Fig. 1 shows the high level architecture of the system to be developed [11]. 1) Map, City, The competition: each competition is played on a map and assigned to a given city. 2) ASA, HSA: Automated Sensor Annotations and Human controlled Sensor Annotations. The ASA subsystem automatically collects traffic flow data using video cameras. In contrast with this, HSA provides data collected by volunteers. The collected data will be used in the Robocar City Emulator. 3) Robocar City Emulator, Results, Monitors: The Monitor programs can visualize the working of the Robocar City Emulator. The results typically are competition reports but

there might be simulation measurements in a given city, even industrial case studies.

A. Design requirements

Only some requirements are highlighted in this section. The full requirements can be found in the software repository of the project [11, doc/SRS] 1) Firstly, it must be specified that the Robocar Emulator can only be considered as an emulator for determining the traffic routing input and output of driverless cars, but in all other aspects it is a simulator. A distant goal is to provide a simulation in which the behavior of the driverless cars and human-driven cars are similar, as much as possible.

2) It is a very important requirement that the platform to be developed must be able to handle a very large number of cars. For example, [4] shows a simulation experiment in which there are 10^6 cars. 3) Another important requirement for the platform is, that it should be able to take into consideration the actual size of a car in such a way that a road can become closed because of the high density of traffic.

Crowd Sensing: The input of the Robocar City Emulator is stored in the City Cloud. This cloud system contains data about the city where the RCE operates. The collection of the data is a crowd sensing based solution. It can be performed in two ways: 1) A community of volunteers perform it manually with a cell phone software (HSA). 2) With specific hardware components developed for our purposes (ASA). By community based solutions we mean manually performed measurements. However, a cell phone application is being developed to assist the data recording. These smart phone applications are very simple and easy-to-use, they consist of only a few buttons. If a vehicle passes the point of measurement, a tap of the respective button is enough to record the event. After the annotation is finished, the application sends the time, position and recorded information to our cloud. Some similar, community based crowd sourcing solutions can be found in [12].

The specific hardware components, that are being developed for our purposes, can perform data collection without user interaction. These devices will be able to recognize vehicles via their video interface. The object detection will be performed with pre-trained cascade files, similar to those used in [13]. This type of object detection has good performance in face and eye recognition [14], [15]. Several solutions are being developed. The main difference between them is the type of processor assembled inside the hardware. The common part in our hardware design is the I/O parts and the usage of a Field Programmable Gate Array (FPGA). The FPGA component can perform tasks with very high speed. For the input, we use an image sensor (e.g. a high resolution video capture module) and a GPS module (to achieve accurate positioning). For the output, we use a standard GSM module to reach mobile data connectivity.

The first type of our hardware design is an ARM based solution [16], [17]. In this type, we use the advantages of the FPGA, mainly for I/O and memory management. The ARM gives us a standard option to perform calculations and image processing. This kind of hardware development can take place on development boards. The main advantage of

this type is that we can use an Embedded Linux System, so the high level processing tasks can be developed in a standard Linux/UNIX environment. An example for this type of system is the widely applied and very popular Raspberry Pi single-board computer [18]. The selection of the suitable development board is currently in progress.

Another solution is based on a soft-processor. In this type, we do not have a physical processor, only an FPGA, so we should add a pre-defined one to our hardware design (e.g. a Xilinx MicroBlaze). In this case, we must specify the operation of the processor, however its instruction set is poorly defined.

The third type of solution has no processor at all, only a pure FPGA design. The whole process, including the I/O handling, image processing and some basic analytics is performed by an FPGA. Certainly, this solution gives us the fastest processing speed, but its development is more complicated.

We conclude that the ARM based solution is very flexible and it is easy to extend it with new features, but we are limited to its instruction set. Also, because OOCWC is an open source project, a hardware design developed in this environment can easily be opened for a community interested in such systems, because these components are cheap and widely used. On the other hand, the purely FPGA based solutions have an advantage in processing speed and we are not limited to the instruction set of ARM.

B. Rapid Prototypes

1) Justine: this is a rapid prototype for development of the OOCWC platform. It is entirely based on Open-StreetMap [19] (OSM) which is a worldwide, community-based open data project published under the Open Data Commons Open Database License. Justine is released under the GNU General Public License Version 3 and can be downloaded from the project's repository at https://github.com/nbatfai/robocar-emulator. It contains three main components: 1) the rcemu is the main software package and consists of Boost C++11 implementations of the smart city and the traffic simulator programs, 2) the rcwin and rclog are online and offline visualization programs for displaying and replaying rcemu simulation files 3) the DocBook 5.1 XML-based [20] documentation sub-project can also be found in the project's repository. The rcemu uses libosmium library [21] for the processing of OSM data. The result of the processing is the routing map graph that is placed in a shared memory segment by the smart city server. The other task of the smart city server is to simulate activities that may occur in the city. The traffic server can simulate the traffic flows. In addition, rcemu contains a sample program that has been written to demonstrate how a client can communicate with the traffic server through TCP and how the shared memory graph may be handled. From the viewpoint of functionality, clients may be routine cars, smart cars and guided cars. From these cars the guided cars are controlled by the competing teams. We are currently working on several editions of the prototype Justine. The main edition of Justine is called "Police Edition" in which cop multi-agents pursue gangster agents for ten minutes. Gangsters are smart cars and cops are guided cars.
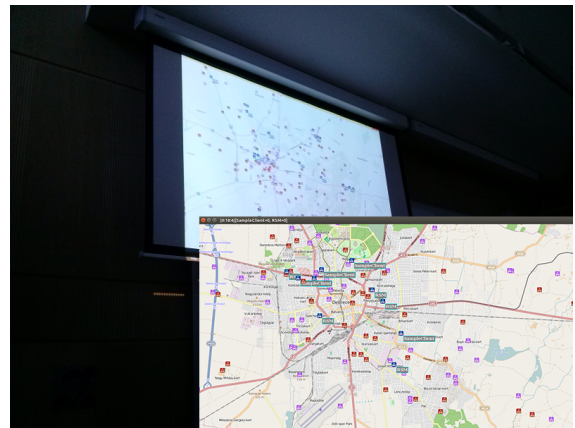

Fig. 2: The rcwin display program in action in the competition called Debrecen 2.

The rcwin and rclog have entirely similar structure, both of them are based on JXMapViewer2 [22]. The rcwin program can be seen in action in Fig. 2 and Fig. 3.

At the time of writing this paper, the official documentation is available only in the Hungarian language, but translations to many languages have already been prepared in the framework of the UDPROG project [23]. A YouTube video of the entire installation process and usage of the OOCWC platform can be seen at https://youtu.be/_FNoFqlygyE.

Operation of simulation model: The simulation has taken place in a rectangular part of the OSM map of the given city in which the competition is played. We call this part as "City Operating Area" or briefly COA. To be more precise, we have built two alternative data structures: one using a directed routing graph created from the OSM data and one using a Boost Graph Library (BGL) graph created from the previous directed graph. The simulation server is based on the directed routing graph but the custom clients may use the BGL graph as well. For example, in the case of Debrecen, the COA is bounded with GPS coordinates from 47.4095 to 47.652 and from 21.4268 to 21.8628. The corresponding routing graphs have 77591 edges and 37455 vertices. Using the terminology of the Nagel-Schreckenberg model, all edges are divided cells. If we interpret our simulation as an implementation of the NaSch model, then the cell length is equal to 3 meters that corresponds to 15 m/s = 54 km/h speed because our simulation cycles last 200 milliseconds. (It also means that all vehicles can move with the same velocity.) In contrast with the NaSch model, a cell may contain many cars, but each edge can only contain a given number of cars. This limit is calculated as the edge length divided by the length of the cell.

The routine cars move by random walk or ant simulations [24], [25]. In the latter case, for example, the next edge of a routine car will be chosen with a probability that increases with the number of past selections of the given edge. The sample client has a predefined implementation of Dijkstra's and Bellman-Ford algorithms to support the routing of guided cars. These implementations use the BGL's Dijkstra's and Bellman-Ford shortest path algorithms [26].

(a) Tile-set view

(b) Aerial view

(c) Hybrid view from distance

(d) Hybrid view closer

Fig. 3: The rcwin display program in action, hybrid view in Manhattan, New York City, USA. These views are provided by the JXMapViewer2[22].

2) Justina: this is another rapid prototype for development of the OOCWC platform and it is also based on OpenStreetMap. The main program contains both the emulator and the visualization components. The emulator uses the same libosmium library for the processing of OSM data. After the data is processed, the emulator cleans out the unnecessary parts, keeping only the roads, thus reducing the size of the map. From this data, a graph is created using the Boost Graph Library which holds the car objects and to which routing algorithms can be applied. The main routing algorithm for the non-routine car agents is the A* algorithm [26]. The algorithm takes into consideration the weight of the edges (roads). The weight of each edge is calculated from its length and the number of cars currently located on that edge, so the less congested roads are more likely to be part of the result. The routine cars move based on the ant simulation algorithm.

The visualization component uses the Qt development framework and can be seen in action in Fig. 4.

III. RESULTS

A. From Debrecen-1 to Debrecen-3

At the time of writing this paper, we have already organized three tournaments. The main purpose of these competitions was to gather first experience with the initial version of the OOCWC software and to find bugs in the source code. The Justine prototype has been used for tournaments. The first competition called Debrecen-1 was held in December 2014
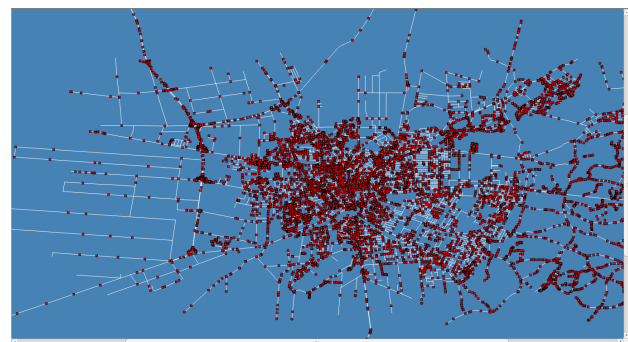

Fig. 4: The display program in action with 10122 cars

with six teams. Three out of the six teams and three new teams participated in the second competition (Debrecen-2) in January 2015. The third competition called Debrecen-3 was held in March 2015, where 43 teams were competing. All three competitions were organized using the prototype "Justine". The detailed documentation (that contains Announcements, Team Qualification Papers, Traffic Logs and Competition Reports) of the last two tournaments is available in English and can be found at http://justine.inf.unideb.hu/2015/Europe/Hungary/Debrecen.

B. Data acquisition

An important part of the system is the data acquisition. To simulate real-world events (e.g. routing, real traffic simulations) we need real-world data. In order to deliver this data, we have implemented a crowd sensing device, which we mentioned in Sect. II-A. The device is an ARM based hardware and software solution and it will be suitable to install it into individual traffic entities (e.g. cars, buses). We should note that an initial testing phase has occurred. In this experiment, some streets of the city of Debrecen has been measured and served as an input for the Robocar City Emulator. The data acquisition project, called Real-Time Traffic Analyzer [16], was applied to proceed this experiment in the Crowd-sourced Traffic Simulator project [27]. The device and the experiment are discussed in [17].

In a brief summary, we give a picture about the operation of this subsystem. With a device, which can be assembled into vehicles, we are able to measure traffic environment around individual traffic entities (including private or public transport). It is important for us regarding these devices that they are in motion constantly, in contrast with the sensors installed on a fix position. So we should consider every factor during the development to aid our plan to install them into vehicles. The base element of the device is a development board, which is currently a Digilent Zybo. This board contains an FPGA and an ARM processor, working parallel (this solution is the first one in Sect. II-A). The FPGA part performs the I/O handling, the ARM processor performs image processing. Because the device is in motion all the time, we needed a GPS module to obtain position and connecting measured data to roads (e.g. streets). The measurement itself is a Haar-cascade based object recognition, the video stream is served by a camera module with the resolution of 640×480. The data is sent to our server through internet connection provided by a GSM module (GPRS connection).

The measurement itself is a car-counting function which gives us a car density value on each road. As many car is counted on a road as dense it is. On the server side, where we receive this data, an algorithm collects these density values by street, so we get a pair of street name and the corresponding intensity of the traffic flow.

In the simulation we use this pair. On the standard interface of the Robocar City Emulator we give this simple text file as an input which will be the initial state of the simulation. So the data collected by the Real-Time Traffic Analyzer, after some systematization, will be served as an initial simulation state. During the simulation we can observe the change of the distribution of the initial data, actually, how the traffic situation changes.

We can conclude that the data acquisition worked well during the testing phase. The object detection method recognized nearly every type of vehicle in the environment of the device, an accurate position obtained with the GPS and the data arrived to our server properly during the measurement. The Robocar City Emulator, after a minor development (and after the creation of the standard interface as well) was able to simulate the traffic outcomes from the initial data.
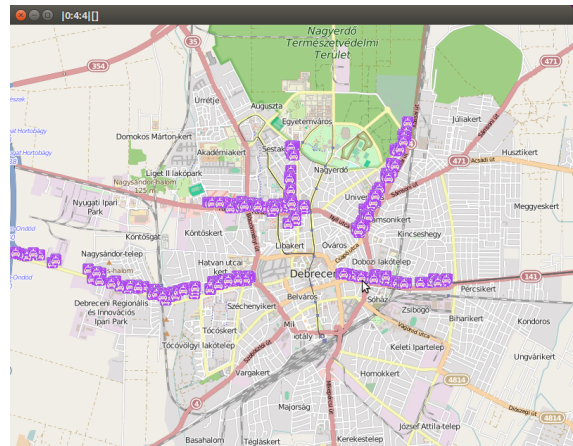

Fig. 5: The initial distribution of cars is based on the following roads Kassai út: 789, Egyetem sugárút: 317, Füredi út: 559, Kishegyesi út: 979, Faraktár utca: 271.

C. The Development of the Traffic Simulation Engine

As we mentioned in the introduction, the challenge of the *robocar-emulator* project is how to handle a large number of vehicles in the traffic simulation, for example, a million cars. It is clear that implementing cars in the simulation as individual software agents is a nearly impossible task. That is why we introduced the notion of routine cars. They are not individual entities like UNIX processes, Java threads or CUDA threads and they have no own individual properties. A routine car only has a probability distribution over the traffic graph nodes. It allows that routine cars can be built in the simulation software itself. The initial distribution of the cars is based on real measured or estimated data. In this work, the simulation starts from a modified version of the estimated distribution used in [17] as it can be seen in Fig. 5. Our main task in this paragraph is to investigate how the traffic simulation had changed this initial distribution of the cars. Fig. 6, 7 and 8 show the changing distribution of the cars over the traffic graph of Debrecen. These ordered histograms present the roads of Debrecen in decreasing order of the number of contained cars at different times of the simulation. It is an interesting observation that neither of these simulations change roughly the (Pareto) nature of the initial distribution but unfortunately it has not been enough. It is also very important that the ordering of the roads must stay the same during the 10 minutes of the simulation. It can be seen well in the presented ordered histograms that our simulation engine cannot fulfill this criteria at its current development phase.

D. Future Work

In this paper, we have shown that random walk and ant simulations are not suitable to move routine cars for the real simulations. The main research goal of the OOCWC platform is to develop a new kind of traffic simulation that does not change the ordering of the roads in the ordered histograms generated during the simulation.
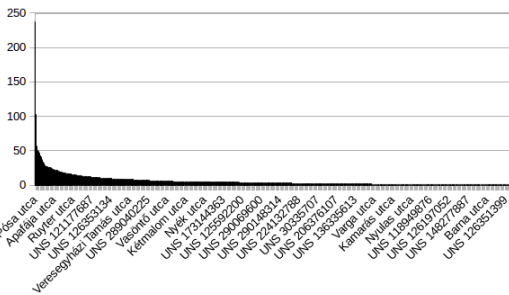
Regarding the crowd sensing subsystem the development and the testing phase has already been initiated. We should
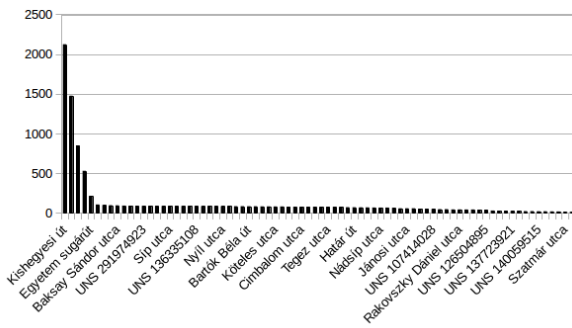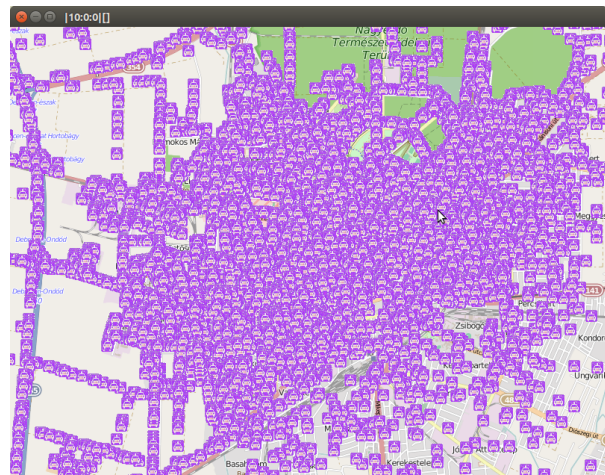
(a) At the beginning of the simulation the number of roads is 78.
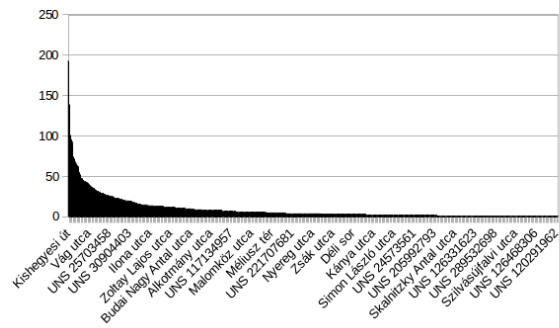
(b) After a minute the number of roads is 1085.

(c) After the ten-minute simulation the number of roads is 1725.

(d) The previous time moment of the simulation is shown in the display program.

Fig. 6: Ordered histograms of cars per road. The x-axis shows the roads ordered by the number of contained cars. The y-axis shows the number of cars on the same road. These histograms only include roads that have at least one car. The simulation has started from a "measured" distribution shown in Fig. 5 and contains 10000 routine cars colored purple that move by random walk.

note that this prototype serve as a good foundation for further research, however to set up a system with 40-50 devices (in a city with the size of Debrecen) is necessary to obtain more experience in the analysis.
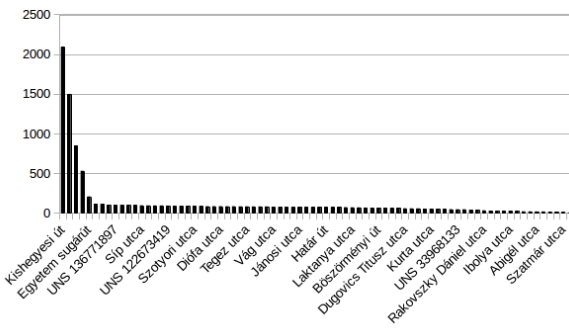
IV. CONCLUSION

In this paper, we have introduced the OOCWC initiative which is intended to offer a research platform for traffic simulations and attempts to organize a community through a coding competition. We have taken the first steps towards a successful implementation of the OOCWC. The "Justine" prototype has acquitted itself well in our local university environment. We found bugs, of course, but they were not too difficult to solve. Therefore, we believe that the time is ripe to build international partnerships around the OOCWC initiative. This paper is a step forward in this direction, because comprehensive use is the best catalyst for the development of a software system. Therefore, we invite researchers, university teachers and students to join the competition and organize their own championship in their own city.

Furthermore, the OOCWC initiative has shown a great step forward in the research of the connection between smart cities and robotcars (mainly in the analysis of real traffic situations). After the proper management of the data collected by the Real-Time Traffic Analyzer and the fine tune of the Robocar City Emulator, we were able to simulate real traffic situations and observe their outcomes. Although, the build-in simulation algorithms need further development, the system has proven to be useful for such functions.
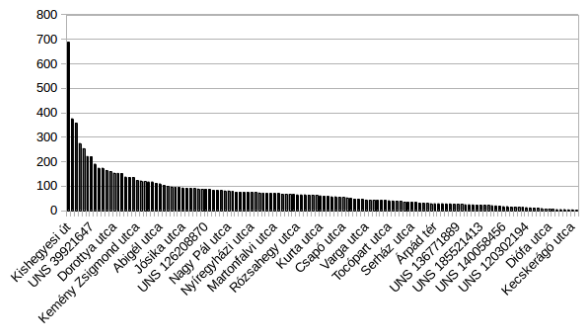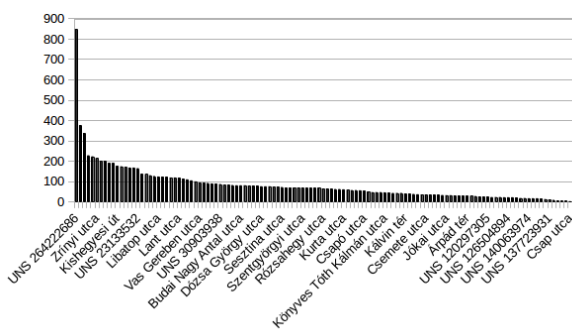
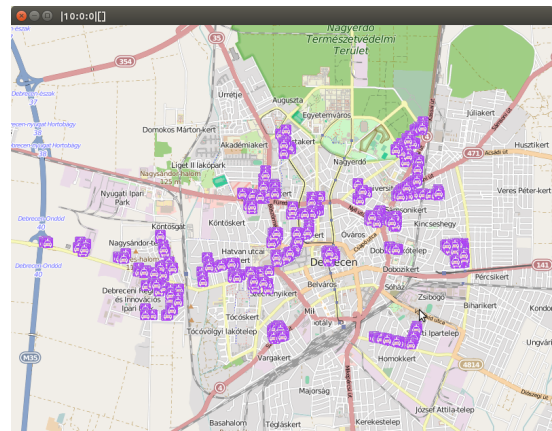Traffic Simulation based on the Robocar World
Championship Initiative

(a) At the beginning of the simulation the number of roads is 78.

(b) After a minute the number of roads is 134.

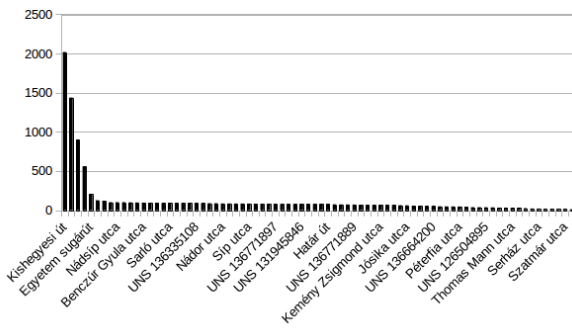(c) After the ten-minute simulation the number of roads is 122.

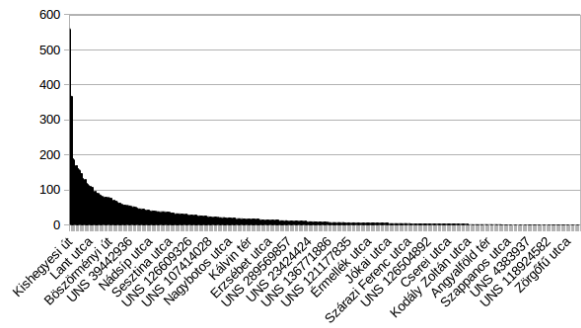(d) The final time moment of the simulation is shown in the display program.

Fig. 7: This simulation has been run with the parameter `traffict=ANTS`, namely the routine cars move by ant simulation. A comparison of different parameters (such as `ANTS`, `ANTS_RND`, `ANTS_RERND` or `ANTS_MRE`, see https://github.com/nbatfai/robocar-emulator/commit/5899ec98f5ce0acd796298929e53aa61037ba656 for details) of ant algorithms can be seen in a YouTube video at https://youtu.be/BwPGvoHls6c.

REFERENCES

[1] "World Urbanization Prospects. The 2007 Revision," United Nations, 2007. [Online]. Available: http://www.un.org/esa/population/publications/wup2007/2007WUP_Highlights_web.pdf

[2] Y. Zheng, L. Capra, O. Wolfson, and H. Yang, "Urban Computing: Concepts, Methodologies, and Applications," *ACM Trans. Intell. Syst. Technol.*, vol. 5, no. 3, pp. 38:1–38:55, Sep. 2014.

[3] H. Kitano, M. Asada, Y. Kuniyoshi, I. Noda, and E. Osawa, "RoboCup: The Robot World Cup Initiative," in *Proceedings of the First International Conference on Autonomous Agents*, ser. AGENTS '97. ACM, 1997, pp. 340–347.

[4] K. Spieser, K. Treleaven, R. Zhang, E. Frazzoli, D. Morton, and M. Pavone, "Toward a systematic approach to the design and evaluation of automated mobility-on-demand systems: a case study in Singapore," in *Road Vehicle Automation*, ser. Lecture Notes in Mobility. Springer, 2014, pp. 229–245. [Online]. Available: http://dspace.mit.edu/handle/1721.1/82904

[5] J. Dallmeyer, A. D. Lattner, and I. J. Timm, "From GIS to Mixed Traffic Simulation in Urban Scenarios," in *Proceedings of the 4th International ICST Conference on Simulation Tools and Techniques*, ser. SIMUTools '11. ICST (Institute for Computer Sciences, Social-Informatics and Telecommunications Engineering), 2011, pp. 134–143. [Online]. Available: http://eudl.eu/pdf/10.4108/icst.simutools.2011.245680

[6] K. Nagel and M. Schreckenberg, "A cellular automaton model for freeway traffic," *J. Phys. I France.*, vol. 2, no. 12, 1992.

[7] M. Treiber, A. Hennecke, and D. Helbing, "Congested traffic states in empirical observations and microscopic simulations," *Phys. Rev. E*, vol. 62, pp. 1805–1824, 2000.

[8] S. Fan, M. Herty, and B. Seibold, "Comparative model accuracy of a data-fitted generalized Aw-Rascle-Zhang model," 2014. [Online]. Available: http://arxiv.org/abs/1310.8219

[9] J. Sewall, D. Wilkie, P. Merrell, and M. C. Lin, "Continuum Traffic Simulation," *Computer Graphics Forum*, vol. 29, no. 2, pp. 439–448, 2010.
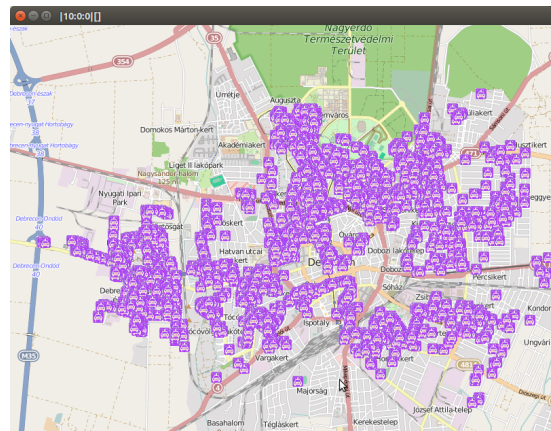
(a) At the beginning of the simulation the number of roads is 78.

(b) After a minute the number of roads is 410.
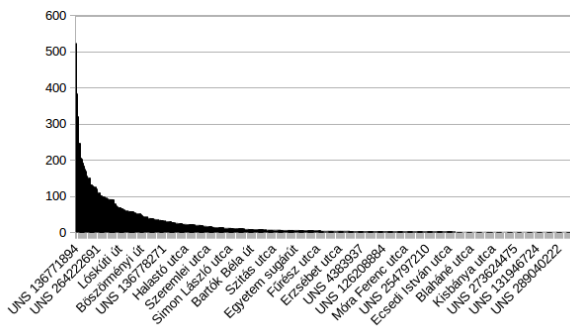
(c) After the ten-minute simulation the number of roads is 456.

(d) The final time moment of the simulation is shown in the display program.

Fig. 8: The simulation has been run with the parameter `traffict=ANTS_RND`.

[10] J. Sewall, D. Wilkie, and M. C. Lin, "Interactive Hybrid Simulation of Large-scale Traffic," *ACM Trans. Graph.*, vol. 30, no. 6, pp. 135:1–135:12, Dec. 2011.

[11] N. Bátfai and et al., "robocar-emulator, Robocar World Championship - Robocar City Emulator," 2015. [Online]. Available: https://code.google.com/p/robocar-emulator/

[12] R. Szabó, K. Farkas, M. Ispány, A. Benczúr, N. Bátfai, P. Jeszenszky, S. Laki, A. Vágner, L. Kollár, C. Sidló, R. Besenczi, M. Smajda, G. Kövér, T. Szincsák, T. Kádek, M. Kósa, A. Adamkó, I. Lendák, B. Wiandt, T. Tomás, A. Z. Nagy, and G. Fehér, "Framework for smart city applications based on participatory sensing," in *Cognitive Infocommunications (CogInfoCom), 2013 IEEE 4th International Conference on*, Dec 2013, pp. 295–300.

[13] P. Viola and M. Jones, "Rapid object detection using a boosted cascade of simple features," in *Computer Vision and Pattern Recognition, 2001. CVPR 2001. Proceedings of the 2001 IEEE Computer Society Conference on*, vol. 1, 2001, pp. I–511–I–518 vol.1.

[14] R. Lienhart, A. Kuranov, and V. Pisarevsky, "Empirical Analysis of Detection Cascades of Boosted Classifiers for Rapid Object Detection," in *Pattern Recognition*. Springer Berlin Heidelberg, 2003, vol. 2781, pp. 297–304.

[15] A. Schmidt and A. Kasiski, "The Performance of the Haar Cascade Classifiers Applied to the Face and Eyes Detection," in *Computer Recognition Systems 2*. Springer Berlin Heidelberg, 2007, vol. 45, pp. 816–823.

[16] R. Besenczi, M. Szilágyi, and I. Oniga, "Real-time Traffic Analyzer project," 2015. [Online]. Available: https://github.com/rbesenczi/real-time-traffic-analyzer

[17] R. Besenczi, M. Szilágyi, N. Bátfai, A. Mamenyák, I. Oniga, and M. Ispány, "Using Crowdsensed Information for Traffic Simulation in the Robocar World Championship Framework," 2015, Accepted.

[18] "Raspberry Pi single-board computer," 2015. [Online]. Available: http://www.raspberrypi.org/

[19] "OpenStreetMap," 2015. [Online]. Available: https://www.openstreetmap.org/about

[20] N. Walsh, L. Muellner, and B. Stayton, *DocBook: The Definitive Guide*. O'Reilly, 2015.

[21] J. Topf, "Osmium Library," 2015. [Online]. Available: http://osmcode.org/libosmium/

[22] M. Steiger, "jxmapviewer2," 2015. [Online]. Available: https://github.com/msteiger/jxmapviewer2

[23] N. Bátfai and et al., "The Yearbook of the Programmers of University of Debrecen," 2015. [Online]. Available: https://sourceforge.net/projects/udprog/

[24] D. M. Gordon, "The development of organization in an ant colony," *American Scientist*, vol. 83, no. 1, pp. 50–57, 1995.

[25] V. Nugala, S. J. Allan, and J. W. Haefner, "Parallel implementations of individual-based models in biology: bulletin- and non-bulletin-board approaches," *Biosystems*, vol. 45, no. 2, pp. 87–97, 1998.

[26] "The Boost Graph Library (BGL)," 2015. [Online]. Available: http://www.boost.org/doc/libs/1_57_0/libs/graph/doc/index.html

[27] R. Besenczi, M. Szilagyi, and I. Oniga, "Crowd-sourced Traffic Simulator," 2015. [Online]. Available: https://github.com/rbesenczi/crowd-sourced-traffic-simulator

Norbert Bátfai is working as an assistant professor in Faculty of Informatics at the University of Debrecen, Hungary. He received his M.Sc. (summa cum laude) in Computer Science at 1998 from the Kossuth Lajos University (KLTE), Debrecen, Hungary. In 1999, he won the first prize in the Java Programming Contest organized by Hungarian Java Alliance: Sun, IBM, Oracle, Novell and IQSoft.
In 2004, his company won the first prize in the Hungarian Mobile Java Developer Contest organized by Sun Hungary and Nokia Hungary. In 2008, the Hungarian Chief Information Officers' Association has selected him as an IT trainer of the year. He received the Ph.D. degree in 2011. He won the Pollák-Virág award from Scientific Association for Infocommunications Hungary in 2012.

Renátó Besenczi is majoring in Engineering Information Technology MSc and working as a research team member at the University of Debrecen, Hungary. His main research areas are smart cities, crowdsensing, crowdsourcing and medical image processing.

András Mamenyák is majoring in Software Information Technology MSc at the University of Debrecen, Hungary. In 2013, he won the first prize in the XDA Tablet Z Development Competition organized by XDA Developers.

Márton Ispány received his Ph.D. degree in 1997 from the Kossuth Lajos University, Hungary. He is an associate professor at the Department of Information Technology at the University of Debrecen, Hungary. Dr. Ispány's research areas include integer valued time series analysis, branching processes, and data mining. He won the Alexits György award from the Hungarian Academy of Sciences and the Pollák–Virág award from the Scientific Association for Infocommunications, Hungary in 2012.

EUSIPCO2016

EUROPEAN SIGNAL PROCESSING CONFERENCE

29 August - 2 September 2016
Hilton Budapest | Hungary

CALL FOR PAPERS

General Chair
Lajos Hanzo
University of Southampton, UK

Technical Co-Chairs
Andrea Conti
University of Ferrara, Italy
Saeid Sanei
University of Surrey, UK

Plenary Sessions Chair
Gerhard Bauch
TU Hamburg-Harburg, Germany

Tutorial Sessions Co-Chairs
Pier Luigi Draghotti
Imperial College London, UK
Gan Woon-Seng
Nanyang Technological University, Singapore

Special Sessions Chair
Alberto Rabbachin
European Commission

Operations Chair
Rolland Vida
Budapest Univ. of Tech. and Econ., Hungary

Publication Chair
Peter Müller
IBM Zurich, Switzerland

Student Activities
Tommaso Melodia
Northeastern University, USA

International Liaisons
Chong-Yung Chi
National Tsing Hua Univ., Taiwan
Moeness Amin
Villanova University, USA

Local Arrangements Chair
Nandor Matrai
Asszisztencia, Hungary

Finance Chair
Peter Nagy
HTE, Hungary

The 2016 European Signal Processing Conference will be held in the vibrant city of Budapest, Hungary from 29 August – 02 September 2016. This flagship conference of the European Association for Signal Processing (EURASIP, www.eurasip.org) will feature a comprehensive technical program addressing all the latest developments in research and technology for signal processing. EUSIPCO 2016 will feature world-class speakers, oral and poster sessions, keynotes, exhibitions, demonstrations and tutorials and is expected to attract many leading researchers and industry figures from all over the world.

TECHNICAL SCOPE

The focus will be on signal processing theory, algorithms, and applications. We invite the submission of original, unpublished technical papers on topics including but not limited to:

- Audio and acoustic signal processing
- Speech processing
- Language processing
- Image and video processing
- Multimedia signal processing
- Signal processing theory and methods
- Sensor array, multichannel and communications signal processing
- Radar and sonar array signal processing
- Estimation theory and applications
- Nonlinear signal processing and adaptive filters
- Cooperative networking
- Compressive sensing, dictionary learning, and sparse reconstruction
- Machine learning
- Signal processing for education
- Design and implementation of signal processing systems
- Information forensics and security
- Bio-inspired modelling and signal processing
- Medical image and signal processing
- Signal processing applications
- Signal processing for Quantum

Accepted papers will be included in IEEE Xplore®.

IMPORTANT DATES

Special session proposals:	**15th December 2015**
Tutorial proposals:	**8th February 2016**
Full paper submissions:	**8th February 2016**
Notification of acceptance:	**25th May 2016**
Camera-ready papers:	**17th June 2016**

Full details of submission procedures are available at
http://www.eusipco2016.org

Guidelines for our Authors

Format of the manuscripts

Original manuscripts and final versions of papers should be submitted in IEEE format according to the formatting instructions available on

http://www.ieee.org/publications_standards/
publications/authors/authors_journals.html#sect2,
"Template and Instructions on How to Create Your Paper".

Length of the manuscripts

The length of papers in the aforementioned format should be 6-8 journal pages.
Wherever appropriate, include 1-2 figures or tables per journal page.

Paper structure

Papers should follow the standard structure, consisting of *Introduction* (the part of paper numbered by "1"), and *Conclusion* (the last numbered part) and several *Sections* in between.
The Introduction should introduce the topic, tell why the subject of the paper is important, summarize the state of the art with references to existing works and underline the main innovative results of the paper. The Introduction should conclude with outlining the structure of the paper.

Accompanying parts

Papers should be accompanied by an *Abstract* and a few *index terms (Keywords)*. For the final version of accepted papers, please send the *short cvs* and *photos* of the authors as well.

Authors

In the title of the paper, authors are listed in the order given in the submitted manuscript. Their full affiliations and e-mail addresses will be given in a footnote on the first page as shown in the template. No degrees or other titles of the authors are given. Memberships of IEEE, HTE and other professional societies will be indicated so please supply this information. When submitting the manuscript, one of the authors should be indicated as corresponding author providing his/her postal address, fax number and telephone number for eventual correspondence and communication with the Editorial Board.

References

References should be listed at the end of the paper in the IEEE format, see below:

a) Last name of author or authors and first name or initials, or name of organization
b) Title of article in quotation marks
c) Title of periodical in full and set in italics
d) Volume, number, and, if available, part
e) First and last pages of article
f) Date of issue

[11] Boggs, S.A. and Fujimoto, N., "Techniques and instrumentation for measurement of transients in gas-insulated switchgear," IEEE Transactions on Electrical Installation, vol. ET-19, no. 2, pp.87–92, April 1984.

Format of a book reference:

[26] Peck, R.B., Hanson, W.E., and Thornburn, T.H., Foundation Engineering, 2nd ed. New York: McGraw-Hill, 1972, pp.230–292.

All references should be referred by the corresponding numbers in the text.
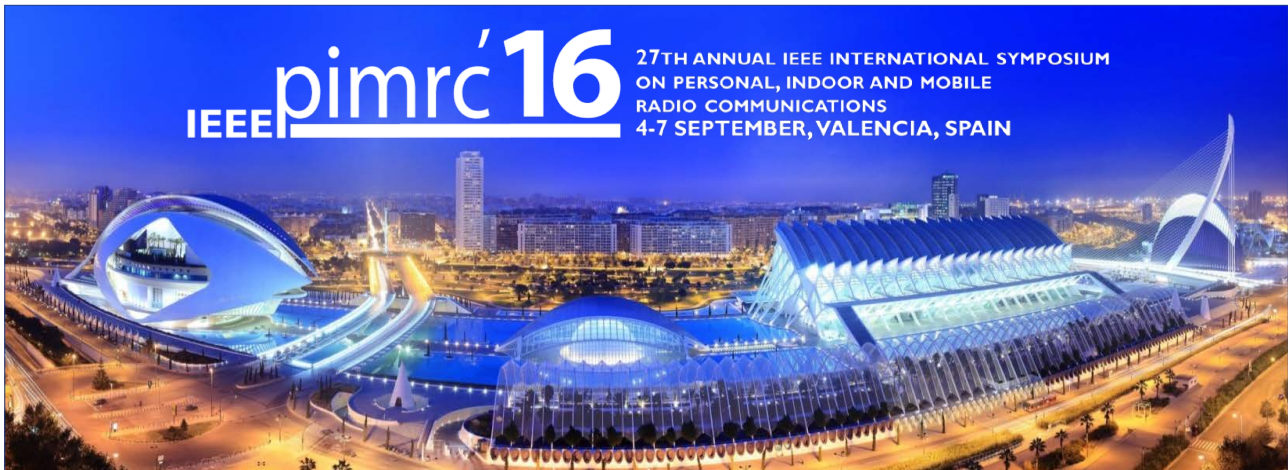
Figures

Figures should be black-and-white, clear, and drawn by the authors. Do not use figures or pictures downloaded from the Internet. Figures and pictures should be submitted also as separate files. Captions are obligatory. Within the text, references should be made by figure numbers, e.g. "see Fig. 2."
When using figures from other printed materials, exact references and note on copyright should be included. Obtaining the copyright is the responsibility of authors.

Contact address

Authors are requested to send their manuscripts via electronic mail or on an electronic medium such as a CD by mail to the Editor-in-Chief:

Csaba A. Szabo
Department of Networked Systems and Services
Budapest University of Technology and Economics
2 Magyar Tudosok krt.
Budapest, 1117 Hungary
szabo@hit.bme.hu

FIRST CALL FOR PAPERS

IEEE PIMRC 2016, SEPT 4-7, 2016, VALENCIA CONFERENCE CENTRE, VALENCIA, SPAIN

www.ieee-pimrc.org

The annual IEEE International Symposium on Personal, Indoor and Mobile Radio Communications (PIMRC) is one of the premier conferences in the wireless research arena and has a long history of bringing together academia, industry and regulatory bodies. Today, it has become one of the IEEE Communication Society's flagship conferences in wireless networking. After two successful editions in Asia and America, the 27th edition of this important wireless event will be held in Valencia, Spain. PIMRC 2016 will include technical sessions, tutorials, workshops, and technology and business panels. You are invited to submit papers, and proposals for panels, tutorials, and workshops, in all areas of wireless communications, networks, services, and applications.

Submission deadline: March 15, 2016

Track 1: Fundamentals and PHY

Advanced modulation schemes; Antennas; Beamforming; Channel capacity estimation; Channel equalisation; Channel modelling; Channel simulation; Cognitive and green radio; Cooperative communications; Interference mitigation; Multi-antenna signal processing; PHY aspects of WLAN, WPAN, and WBAN; PHY performance evaluation; Physical layer network coding; Physical layer security; Positioning, localisation, and tracking techniques; Power efficient communications; RF Propagation modelling; Signal processing for wireless communications; Single and multi-user MIMO; Source and channel coding; Synchronisation techniques; Ultra-wideband communications; Vehicular communications.

Track 3: Mobile and Wireless Networks

5G Networks; Software defined wireless networks; Mobile cloud networking; Mobile social networks; Mobile internet of things; Ad hoc networks; Body area networks; Cognitive radio networks; Congestion, load and admission control; Cooperative communications; Delay tolerant networks; Dynamic spectrum management; Future wireless Internet; Green wireless networks; Mobile computing; Network architectures; Routing, QoS and scheduling; Satellite communications; Self-organising networks; Smart cities; Smart grids; Vehicular networks; Multicasting, broadcasting, and geocasting; Wireless sensor networks.

Track 2: MAC and Cross-Layer Design

Adaptive MACs; Cognitive MACs; Cross-layer designs involving MAC; Delay tolerant MAC designs; MAC design for D2D, V2X communications; MAC design for MTC; Docitive MACs; Implementation, testbeds and prototypes; Information-theoretical approaches to MAC designs; Joint access and backhaul scheduler designs; Joint MAC and networking layer designs; MAC for low power embedded networks; MAC for mobile and vehicular ad hoc networks; QoS/QoE-enabling MAC in 4G and future mobile networks; Radio resource management, allocation, and scheduling; Reconfigurable MACs; Scheduler for cellular macro-, pico- and femto systems; Scheduler for cooperative systems; Scheduler for relay systems; Security issues in MAC designs; Time-critical MAC designs.

Track 4: Services, Applications and Business

Audio and video broadcast applications; Authentication, authorization and accounting; Context and location-awareness in pervasive systems; Cyber-physical system / real-world Internet; Emerging wireless/mobile applications; In-/intra-car communications; Mobile multimedia services; Link data and networked knowledge; Next generation digital home networks; P2P services for multimedia; Personalization, profiles and profiling; Secure network and service access; Self-adaptation on the service layer; Semantic technologies; Service discovery; Service oriented architectures and cloud computing; Service portability; User interfaces, user-machine interactions; Wireless emergency and security systems; Wireless robotics.

Co-Sponsored by:

UNIVERSITAT POLITÈCNICA DE VALÈNCIA

IEEE COMMUNICATIONS SOCIETY

Executive and Technical Program Co-Chairs

Narcís Cardona (iTEAM- U.P. Valencia, Spain)

Luis M. Correia (IST - U. Lisbon, Portugal)

SCIENTIFIC ASSOCIATION FOR INFOCOMMUNICATIONS

Who we are

Founded in 1949, the Scientific Association for Info-communications (formerly known as Scientific Society for Telecommunications) is a voluntary and autonomous professional society of engineers and economists, researchers and businessmen, managers and educational, regulatory and other professionals working in the fields of telecommunications, broadcasting, electronics, information and media technologies in Hungary.

Besides its 1000 individual members, the Scientific Association for Infocommunications (in Hungarian: HÍRKÖZLÉSI ÉS INFORMATIKAI TUDOMÁNYOS EGYESÜLET, HTE) has more than 60 corporate members as well. Among them there are large companies and small-and-medium enterprises with industrial, trade, service-providing, research and development activities, as well as educational institutions and research centers.

HTE is a Sister Society of the Institute of Electrical and Electronics Engineers, Inc. (IEEE) and the IEEE Communications Society.

What we do

HTE has a broad range of activities that aim to promote the convergence of information and communication technologies and the deployment of synergic applications and services, to broaden the knowledge and skills of our members, to facilitate the exchange of ideas and experiences, as well as to integrate and harmonize the professional opinions and standpoints derived from various group interests and market dynamics.

To achieve these goals, we…

- contribute to the analysis of technical, economic, and social questions related to our field of competence, and forward the synthesized opinion of our experts to scientific, legislative, industrial and educational organizations and institutions;
- follow the national and international trends and results related to our field of competence, foster the professional and business relations between foreign and Hungarian companies and institutes;
- organize an extensive range of lectures, seminars, debates, conferences, exhibitions, company presentations, and club events in order to transfer and deploy scientific, technical and economic knowledge and skills;
- promote professional secondary and higher education and take active part in the development of professional education, teaching and training;
- establish and maintain relations with other domestic and foreign fellow associations, IEEE sister societies;
- award prizes for outstanding scientific, educational, managerial, commercial and/or societal activities and achievements in the fields of infocommunication.

Contact information

President: **GÁBOR MAGYAR, PhD** • *elnok@hte.hu*
Secretary-General: **ISTVÁN BARTOLITS** • *bartolits@nmhh.hu*
Operations Director: **PÉTER NAGY** • *nagy.peter@hte.hu*
International Affairs: **ROLLAND VIDA, PhD** • *vida@tmit.bme.hu*

Address: H-1051 Budapest, Bajcsy-Zsilinszky str. 12, HUNGARY, Room: 502
Phone: +36 1 353 1027, Fax: +36 1 353 0451
E-mail: *info@hte.hu*, Web: *www.hte.hu*